Nano Research

ISSN 1998-0124 CN 11-5974/O4
https://doi.org/10.26599/NR.2026.94908728

Review Article

Advances in single atom alloy: synthesis, electronic regulation and application in energy-related electrocatalysis

Jiansong Miao[1], Shengwang Gong[1], Jingjing Jiang[2](✉), Xin Li[1], Xiaohui Sun[1](✉), Chunming Xu[1]

[1] State Key Laboratory of Heavy Oil Processing, China University of Petroleum (Beijing), Beijing 102249, China

[2] Institute of Analysis and Testing, Beijing Academy of Science and Technology, Beijing 100094, China

Nano Res., **Just Accepted Manuscript** • https://doi.org/10.26599/NR.2026.94908728

https://www.sciopen.com/journal/1998-0124 on Apr. 9, 2026

Just Accepted

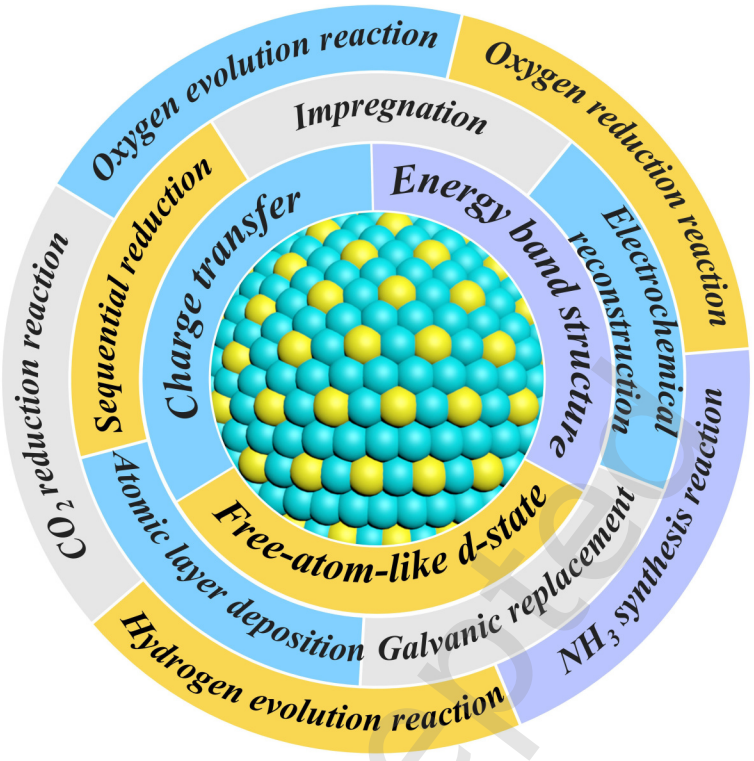

This review systematically summarizes the preparation strategies of SAAs and their electrochemical applications in recent years. It also probes the unique host-guest electronic interactions in SAAs to establish the intrinsic structure-performance relationship. We expect that this work can contribute to guide the rational design of next-generation SAAs toward practical applications in the field of energy-related electrocatalysis.

Nano Research

Open Access

Review Article

Advances in single atom alloy: synthesis, electronic regulation and application in energy-related electrocatalysis

Jiansong Miao[1], Shengwang Gong[1], Jingjing Jiang[2] ✉, Xin Li[1], Xiaohui Sun[1] ✉, and Chunming Xu[1]

[1] *State Key Laboratory of Heavy Oil Processing, China University of Petroleum (Beijing), Beijing 102249, China*
[2] *Institute of Analysis and Testing, Beijing Academy of Science and Technology, Beijing 100094, China*

Received: 10 February 2026; **Revised:** 22 March 2026; **Accepted:** 9 April 2026

✉Address correspondence to Xiaohui Sun, sunxiaohui@cup.edu.cn; Jingjing Jiang, jiangjingjing@bcpca.ac.cn

Cite this article: *Nano Research*, 2026, 19, 94908728 https://doi.org/10.26599/NR.2026.94908728

ABSTRACT: Single-atom alloy catalysts (SAAs), which consist of catalytically active metal atoms atomically dispersed within inert metal matrices, have recently attracted considerable attention. SAAs combine the merit of maximized atomic utilization from single-atom catalysts (SACs) with the feature of intermetallic electronic synergetic modulation from alloy catalysts. This enables the synergetic catalysis of multiple active sites, achieving highly active and selective catalysis. Hence, in this review, we summarize recent progress of SAAs from the perspective of synthetic methods, unique electronic properties, and their applications in a series of energy-related electrocatalytic reactions. First, the major approaches, including impregnation, sequential reduction, galvanic replacement, atomic layer deposition, and electrochemical reconstruction, for the fabrication of SAAs are overviewed. Second, the unique electronic properties between single-atom sites and metal supports in SAAs, including free-atom-like *d*-state, charge transfer, and energy band structure, are further elaborated. Then, the applications of SAAs in various energy-related electrocatalytic reactions are discussed to elucidate the structure-performance relationships and understand the reaction mechanisms. Finally, a conclusion of this review and insights into the challenges and prospects pertaining to this field are also highlighted.

KEYWORDS: single-atom alloy catalysts (SAAs), unique electronic properties, synergistic effects, electrocatalysis

1 Introduction

The combustion of conventional fossil fuels releases massive carbon dioxide and hazardous gaseous pollutants, which severely jeopardizes human living environments and even the ecological security of the Earth [1, 2]. To alleviate these issues, extensive efforts have been devoted to the exploration of renewable energy storage technologies, which convert electrical energy into chemical energy via clean electricity and involve a series of chemical transformation processes [3-5]. Metal-based solid catalysts play a pivotal role in these chemical transformation processes, as they accelerate the kinetics of chemical reactions while remaining chemically unchanged throughout the reaction, and have thus been widely applied in various electrocatalytic reactions [6-8]. Typical examples include the electrocatalytic water splitting, electrocatalytic oxygen reduction reactions (ORR) in fuel cell operation, electrocatalytic carbon dioxide reduction reaction (CO_2RR), and electrocatalytic ammonia synthesis reaction [9-17]. Nevertheless, these electrocatalytic conversion reactions are confronted with multiple challenges. For instance, CO_2 can be converted into C1 and multi-carbon products in CO_2RR, where high current densities and product selectivity have become a key bottleneck restricting practical development, and HER also suffers from excessive overpotential that causes a waste of electrical energy [18-22]. In view of these common bottlenecks, the development of high-efficiency metal-based solid electrocatalysts is one of the core factors to address the aforementioned issues.

Heterogeneous catalysis is an important branch of catalytic reactions, with its core being the presence of a phase interface between the solid catalyst and reactants [23-27]. In the catalytic reaction, it mainly involves solid catalysts acting on gas/liquid phase systems, where reactant molecules complete the processes of adsorption, conversion, and desorption on the catalyst surface [28-35]. A platinum powder catalyst that was developed by Döbereiner et al. in 1822 was capable of accelerating the oxidation of ethanol with oxygen to acetic acid, laying the foundation for the pioneering application of heterogeneous catalysis [36]. Subsequently, single-metal catalysts were modified via alloying to fabricate alloy catalysts, which has further propelled the advancement of heterogeneous catalysis. For example, Bosch and his colleagues reported preparation methods for various bimetallic and multimetallic alloy materials used in ammonia synthesis in their patents in the early 1910s [37]. These materials exhibited better performance than pure iron catalysts, and the improvement in their performance stems from the adjustability of the electronic and geometric structures of metal achieved through alloying [38-40]. It is precisely due to this modification advantage that the catalytic performance of

alloy catalysts has been significantly improved in various catalytic reaction [41-45]. However, the arbitrary aggregation of different metallic species during the growth process renders the construction of alloy catalysts with a homogeneous and clearly defined active coordination environment extremely challenging [46-49].

The solid-gas or solid-liquid interface serves as the reactive area for heterogeneous catalysis [50, 51]. Therefore, the density of active sites on the surface of solid catalysts is crucial for heterogeneous catalytic reactions [29, 52]. As catalysts have evolved from bulk phases to nanoparticles, catalytic efficiency has been improved, yet their atomic utilization efficiency remains limited. To further enhance atomic utilization and catalytic efficiency, researchers proposed the concept of single-atom catalysts (SACs), in which these single metal atoms are normally anchored by chemical bonding with coordination atoms on a substrate (e.g., metals, metal oxides/sulfides, and nanoporous carbon, etc.) [53-56]. Since Zhang et al. first reported Pt SACs supported on iron oxide for CO oxidation in 2011, the field of SACs has experienced an explosive boom over the past decade [57]. This groundbreaking achievement in heterogeneous catalysis maximizes atomic utilization efficiency to nearly 100% by realizing the atomic-level mono-dispersion of metal active sites [58-60]. Furthermore, based on this high atomic utilization efficiency, the rational regulation of single metal species and heteroatom coordination environments allows for the precise optimization of catalytic active centers, which in turn contributes to the enhancement of overall catalytic performance [61, 62]. For instance, Liu et al. reported that the Sc_1/NC SAC exhibited an 81.3% CO selectivity in CO_2RR [63]. When the metal active site was be substituted with Y, Y_1/NC SAC exhibited 88.3% CO selectivity. In another example, Yang et al. synthesized a Mn-SAC featuring a dual oxygen-nitrogen coordination (Mn-N_3O_1), which exhibited excellent electrocatalytic performance toward the ORR. At the Mn-N_3O_1 active sites, the cooperative coordination effect of O and N heteroatoms tunes the d-band electronic structure of Mn to an optimal electronic state, thereby conferring the catalyst with ultra-rapid ORR kinetic [64]. However, altering the metal species and coordination environment merely optimizes the electronic structure of single-atom active sites, while it offers limited scope for expanding the diversity of active sites. Thus, the single active site nature of SACs inherently restricts the adsorption modes of reaction intermediates. Furthermore, a single active center cannot independently regulate the adsorption energy of specific reaction intermediates, namely the scaling relationship limitation [65-67]. These limitations significantly impede the catalytic kinetic performance of SACs in multi-step reactions.

Single-atom alloy catalysts (SAAs), an emerging frontier in SACs, combines the advantages of conventional alloy catalysts and SACs, where trace amounts of catalytically active metal atoms are atomically dispersed within inert metal matrices [68-71]. The lattice-confined metal-metal interaction in SAAs provides much stronger thermodynamic stabilization for isolated sites than the surface coordination between metal and carbon/heteroatoms in traditional carbon-based SACs, thus effectively suppressing atomic migration, sintering, and leaching [72-74]. Moreover, no metallic bonds are formed between the guest metal atoms, endowing the guest metal atoms with the characteristics of free-atom-like atoms [75]. This unique electronic structure grants them excellent product selectivity and catalytic activity. For example, a study by Sykes et al. found that when Pt atoms are doped on the Cu(111) surface to form PtCu SAA, the Pt atoms can promote hydrogen activation and spillover of H to Cu, thereby facilitating the conversion of 1,3-butadiene to butene [76]. When the Pt atoms aggregate into clusters, the selectivity of butene is significantly reduced. What's more important is that the electronic interactions (e.g., electron transfer and orbital hybridization) between the guest metal single atoms and host metal matrix induce both guest and host metal atoms to exhibit synergistic catalytic activity [77, 78]. Such synergistic catalysis can effectively break the scaling relationship limitation in SACs, thereby promoting the activity and selectivity for multi-step reactions [79, 80]. For instance, Jin et al. fabricated a Mo_1Cu SAA catalyst with multiple active sites for CO_2RR [81]. Interestingly, negatively charged Mo atoms facilitate the dissociation of water to generate active H* species, and Cu atoms distant from Mo sites promote the conversion of CO_2 to *CO. Meanwhile, positively charged Cu species adjacent to Mo serve as the active center for the adsorption and activation of *CO and H*, synergistically catalyzing C-C coupling to produce C_{2+} products. However, in SACs, especially carbon-based SACs, although there exist certain electronic interactions between metal species and carbon/heteroatoms, their active-site types are relatively uniform, which still limits the further improvement of overall catalytic efficiency [82].

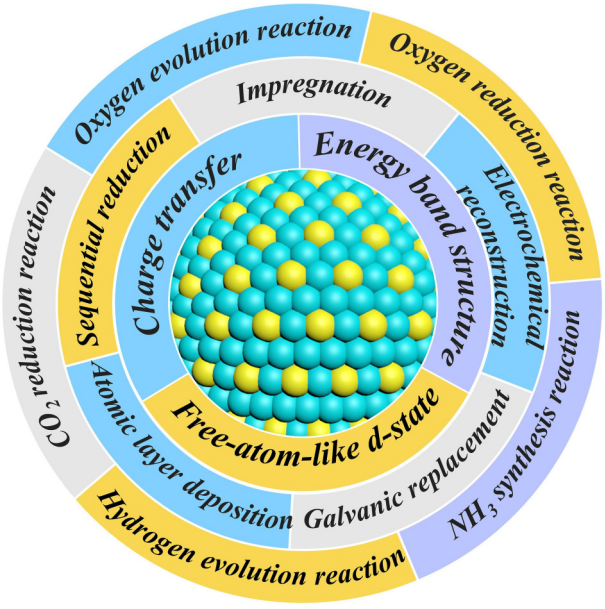

Figure 1. Overview of the topics covered in this review

Until now, numerous review papers have summarized the latest advances in the field of SAAs [69, 71, 72, 83-85]. For example, some papers systematically reviewed the synthetic strategies, advanced characterization techniques of SAAs, and their applications in heterogeneous catalysis [71, 72]. Beyond summarizing the design principles of SAAs, other

researchers have further probed into how SAAs modulate the adsorption behavior of reaction intermediates [85]. However, few reviews have focused on the unique interatomic interactions of SAAs and how such interactions determine their catalytic performance. This review therefore aims to summarize the recent progress in SAAs to fill this gap. We first summarize the synthesis methods of SAAs, including impregnation, sequential reduction, galvanic displacement, atomic layer deposition and electrochemical reconstruction. We then focus on the unique interatomic interactions from the perspectives of free-atom-like *d*-state behavior, charge transfer and energy band structure. Subsequently, we further introduce a series of electrocatalytic reactions to elaborate on their structure-performance relationships and reaction mechanisms. Finally, based on the summary of the latest advances, the existing challenges and future perspectives in the field of SAAs are proposed, aiming to provide insights and guidance for the design of high-performance single atom alloy catalysts for energy-related electrocatalysis (Figure 1).

2. Synthesis method

The development of simple and effective strategies is a prerequisite for the synthesis of highly active SAA catalysts. In this section, we describe several commonly used approaches for synthesizing diverse SAAs, including impregnation, sequential reduction, galvanic replacement (GR), atomic layer deposition (ALD), and electrochemical reconstruction. Combined with advanced characterization techniques, comprehensive information on the structure, chemical state and catalytic behavior of SAAs can be obtained.

2.1 Impregnation

The impregnation method is a commonly used technique for the synthesis of heterogeneous catalysts, which is particularly suitable for the preparation of supported metal catalysts [86-88]. The fundamental principle underlying this approach is the impregnation of the carrier in a solution containing active metal precursors. During impregnation, dilute metal precursors are uniformly adsorbed onto surface defects and functional sites of the support via electrostatic attraction or coordination binding, which spatially isolates individual metal species [89]. Subsequent drying, calcination, and reduction further anchor these adsorbed species and transform them into isolated active sites [90]. Since this method is straightforward, cost-effective, and amenable to large-scale production, it has been widely applied in the synthesis of SAAs. However, due to the distinctive structural properties of SAAs, the composition and proportion of the precursors must be meticulously calibrated to guarantee the mono-dispersity of the metal atoms [91-93]. By adjusting the precursor concentration, carrier type, impregnation time and temperature, and heat treatment conditions, the optimal process parameters for different metal combinations can be identified.

For instance, Zou et al. impregnated a TiO_2 support with a mixed solution of $RuCl_3{\cdot}xH_2O$ and $NiCl_2{\cdot}6H_2O$. After subsequently drying and reducing the precursor at a high temperature in a H_2 atmosphere, a series of Ru_xNi_y/TiO_2 catalysts with different Ru and Ni molar ratios were obtained (Figure 2a) [94]. High-angle annular dark-field scanning transmission electron microscopy (HAADF-STEM) image showed that a series of RuNi bimetallic nanoalloys with particle sizes between 0.9 and 3.9 nm were uniformly distributed on the TiO_2 supports in the form of nano-alloy islands (Figure 2b). The nanoalloy-islands in the high-magnification HAADF-STEM image of $Ru_1Ni_{2.5}/TiO_2$ exhibited uniform lattice fringes of approximately 0.203 nm, corresponding to Ni (111), indicating Ni as the host metal in the nanoalloy-islands (Figure 2c). Furthermore, the atomic resolution HAADF-STEM image of $Ru_1Ni_{2.5}/TiO_2$ showed a brighter spot than the surrounding atoms. Since Ru has a higher proton number (Z) than Ni, this brighter spot can be attributed to a single Ru atom in a Ni nanocluster with a size of about 0.9 nm (Figure 2d). In the study of *in situ* diffuse reflectance infrared Fourier transform spectra of CO adsorption (CO-DRIFTS) of the samples, a single narrow peak at 2081 cm^{-1} without parallel accompanying peaks was detected and could be identified as $Ru^{n+}(CO)_2$ adsorbed on the low coordination isolated Ru site surrounded by Ni in the RuNi alloy (Figure 2e). Further analysis of Ru K-edge X-ray absorption near-edge structures (XANES) spectra has revealed that both the average valence states of Ru in $Ru_1Ni_{2.5}/TiO_2$ and Ru_4Ni_{10}/TiO_2 were between Ru foil and RuO_2, indicating partial oxidation of the alloy surface under ex-situ conditions (Figure 2f). Fourier-transformed k^3-weighted extended X-ray adsorption fine structure (EXAFS) in R space of these catalysts were also analyzed to identify the coordination environment of Ru atoms in Ni nanoparticles (NPs). Only Ru-Ni scattering at 2.31 Å in $Ru_1Ni_{2.5}/TiO_2$ but both Ru-Ni (2.31 Å) and Ru-Ru (2.35 Å) scattering paths in Ru_4Ni_{10}/TiO_2 were observed, respectively (Figure 2g). Moreover, the Ru-Ni coordination number (CN) in $Ru_1Ni_{2.5}/TiO_2$ from the R-space fitting results is 0.54, which is much lower than that in Ru_4Ni_{10}/TiO_2 (1.48). This result indicated that in smaller nanoalloy-islands, Ru atoms tended to occupy low coordination sites such as the surface exposed corner or edge sites.

Huang et al. fabricated a series of Cu_8Pd_1/Al_2O_3 SAA catalysts by stepwise impregnating an Al_2O_3 support with an aqueous mixture of $Pd(NH_3)_4(NO_3)_2$ and $Cu(NO_3)_2{\cdot}3H_2O$ with certain molar ratios, drying and calcination [95]. X-ray photoelectron spectroscopy (XPS) analysis revealed that compared with Pd/Al_2O_3 and Cu/Al_2O_3, the binding energy of the Pd *3d* peak increased, while that of the Cu *2p* peak decreased, indicative of the charge transfer from Pd to Cu atoms in Cu_8Pd_1/Al_2O_3. HAADF-STEM image showed uniformly distributed bright spots that represented single Pd atoms on Cu_8Pd_1/Al_2O_3 (Figure 2h). The CO-DRIFT spectra showed a peak at 2080 cm^{-1} coupled with a broad peak at 1930 cm^{-1} on Pd/Al_2O_3, corresponding to linear CO absorption on Pd and bridging CO absorption on neighboring Pd atoms, respectively (Figure 2i). Since CO adsorption on single Pd atom tends to be linear adsorption rather than bridging adsorption, the absence of bridging CO adsorption on the Cu_8Pd_1 and $Cu_{20}Pd_1$ samples strongly suggested isolated Pd atoms at the surface. Furthermore, with the Pd content decreasing, the linearly adsorbed CO peaks on Pd in the $CuPd/Al_2O_3$ samples showed a gradually widened blue shift to 2100 cm^{-1} for Cu_1Pd_1/Al_2O_3 and 2103 cm^{-1} for $Cu_{20}Pd_1/Al_2O_3$. Such shift suggested that the

electronegativity of Pd in the $CuPd/Al_2O_3$ samples was weakened, implying a potential electron transfer from Pd to Cu. This is consistent with the XPS results, confirming the successful preparation of the Cu_8Pd_1/Al_2O_3 SAA. Bai et al. also reported a Pt_1In-ZnO_x SAA by immersing an $In(OH)_3$-ZnO support into a stoichiometric H_2PtCl_6 ethanol solution and subsequent reduction at 400 ℃ for 4 h in H_2 [96]. HAADF-STEM images indicated that the Pt single atoms with a large proton number were highly dispersed in the In lattice (Figure 2j). Pt L_3-edge XANES spectra showed that the Pt white-line intensity of Pt_1In-ZnO_x near 11568 eV was lower than that of PtO_2 but higher than that of Pt, indicating that the valence state of Pt in Pt_1In-ZnO_x was between 0 and +4. The k^2-weighted EXAFS spectrum of Pt_1In-ZnO_x showed one prominent peak at 2.3Å with a length between Pt-O and Pt-Pt bonds, which could be assigned to the Pt-In bond (Figure 2k). Neither Pt-Pt nor Pt-O coordination contributions were detected, demonstrating the formation of Pt_1In SAA. In another example, Hu and coworkers synthesized a $NiIr_{SAA}$-NiFe-Layered Double Hydroxide (LDH) with an Ir loading of 8.31 wt.% by impregnating the NiFe-LDH precursor with H_2IrCl_6 solution followed by reduction with $NaBH_4$ at 80°C for 1 h (Figure 2l) [97]. When $NaBH_4$ was substituted by NaOH, only Ir single atoms were deposited on the NiFe-LDH support (denoted as Ir_{SAC}-NiFe-LDH) with a comparable Ir loading of 8.47 wt.%. The scanning electron microscopy (SEM) images revealed that both Ir_{SAC}-NiFe-LDH and $NiIr_{SAA}$-NiFe-LDH exhibited a typical layered structure of LDHs (Figure 2m, o). At the same time, some bright spots that represented single Ir atoms were also detected on the LDH surface from their HAADF-STEM images (Figure 2n, p). From the Ir L_3-edge XANES spectra, the intensity of the white line edge suggested that the valence state of the prepared catalysts decreased in the sequence of Ir_{SAC}NiFe-LDH > IrO_2 > Ir_{SAA}NiFe-LDH > Ir foil (Figure 2q). This indicates that the existence state of metal single atoms in another metal will affect their electron distribution. Furthermore, the Ir L_3-edge EXAFS spectra revealed that only a single peak at 1.6 Å was observed in Ir_{SAC}-NiFe-LDH, corresponding to the Ir-O coordination. By contrast, the Ir L_3-edge EXAFS spectra of $NiIr_{SAA}$-NiFe-LDH showed a major peak at 2.3 Å, attributed to the scattering of the Ir-Ni bond. No Ir-Ir bond was detected, indicative of the formation of the $NiIr_{SAA}$ structure (Figure 2r).

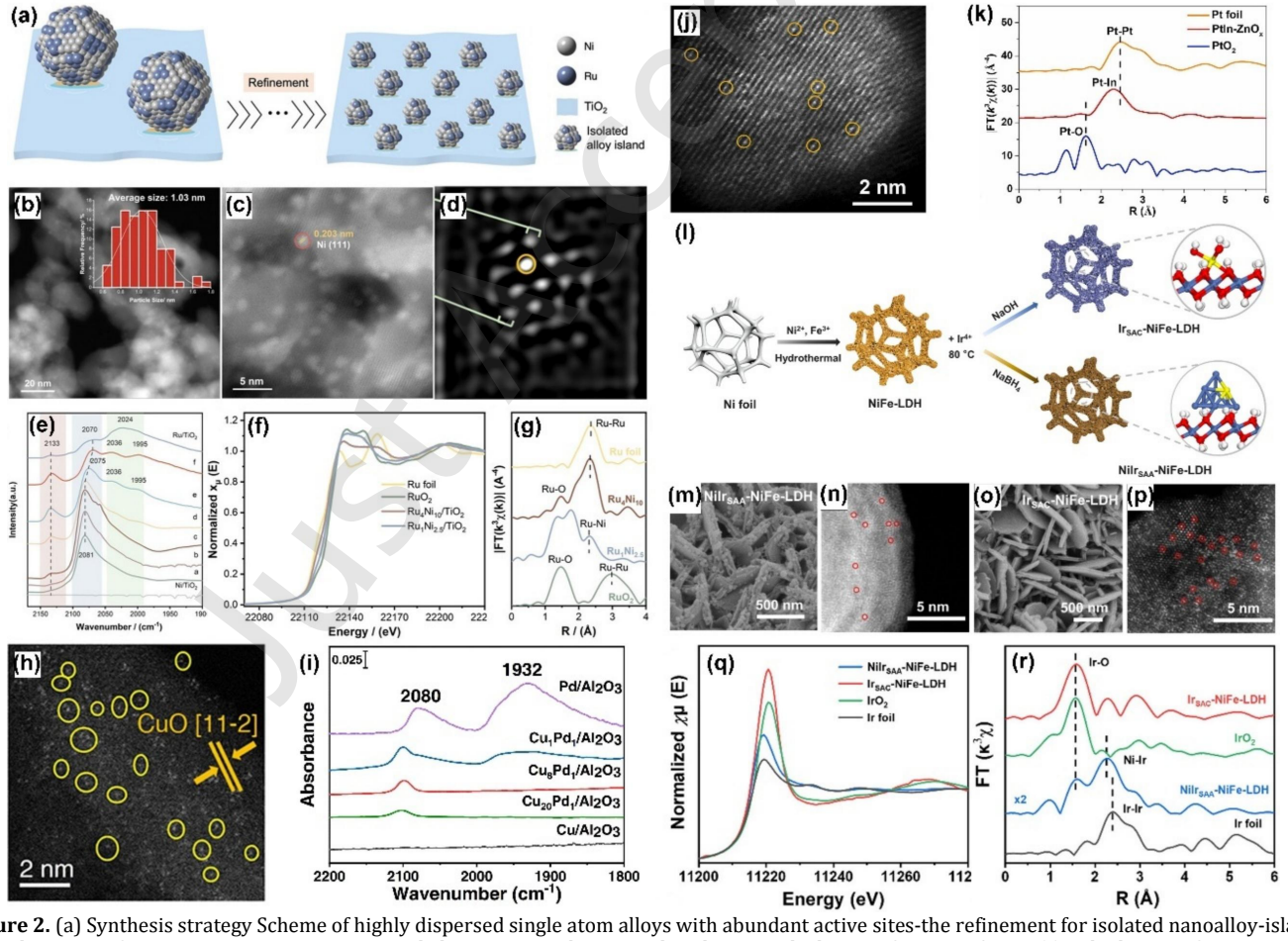

Figure 2. (a) Synthesis strategy Scheme of highly dispersed single atom alloys with abundant active sites-the refinement for isolated nanoalloy-islands. (b) a low-magnification STEM-HAADF image and the corresponding size distribution calculation of $Ru_1Ni_{2.5}/TiO_2$. (c) a high-magnification STEM-HAADF image and (d) an atomic-resolution STEM-HAADF image of a nanocluster in $Ru_1Ni_{2.5}/TiO_2$. (e) CO-DRIFTS of all samples (a. $Ru_{0.5}Ni_{1.25}/TiO_2$, b. $Ru_1Ni_{2.5}/TiO_2$, c. Ru_2Ni_5/TiO_2, d. $Ru_3Ni_{7.5}/TiO_2$, e. Ru_4Ni_{10}/TiO_2, f. $Ru_5Ni_{12.5}/TiO_2$). (f) Ru K-edge XANES for $Ru_1Ni_{2.5}/TiO_2$, Ru_4Ni_{10}/TiO_2, a Ru foil, and RuO_2. (g) Ru K-edge EXAFS Fourier-transform spectra in R space; Reproduced with permission from Ref. [94] Copyright 2024, Wiley-VCH. (h) Representative high-resolution AC-HAADF-STEM image of Cu_8Pd_1/Al_2O_3 sample. (i) In situ CO-DRIFT spectra of Cu_8Pd_1/Al_2O_3 samples; Reproduced with permission from Ref. [95] Copyright 2024, Elsevier. (j) HAADF-STEM image of PtIn-ZnO_x. Yellow circles: isolated Pt single atoms. (k) Pt L_3-edge EXAFS spectra in R space of Pt foil, PtIn-ZnO_x and PtO_2; Reproduced with permission from Ref. [96] Copyright 2025, Elsevier. (l) Schematic Diagram of the Synthetic Process of Ir_{SAC}-NiFe-LDH and $NiIr_{SAA}$-NiFe-LDH. (m-p) The (m, o) SEM image and (n, p) HAADF-STEM of $NiIr_{SAA}$-NiFe-LDH and Ir_{SAC}-NiFe-LDH. (q) Ir L_3-edge XANES spectra of $NiIr_{SAA}$-NiFe-LDH, Ir_{SAC}-NiFe-LDH, IrO_2, and Ir foil. (r) EXAFS spectra at the Ir L_3-edge of Ir_{SAC}-NiFe-LDH, IrO_2,

NiIr$_{SAA}$-NiFe-LDH, and Ir foil; Reproduced with permission from Ref. [97] Copyright 2023, American Chemical Society.

Impregnation represents the most industrially mature strategy for the synthesis of SAAs, with exceptional versatility toward diverse metal combinations and support materials. It is also seamlessly compatible with commercial catalyst manufacturing lines and enables facile, cost-effective catalyst preparation. Nonetheless, conventional impregnation exhibits inherent drawbacks in the precise control of atomic dispersion, as guest metal precursors are prone to sintering and aggregation during thermal treatment, which imposes strict limitations on the maximum guest metal loading for retaining atomic dispersion. Accordingly, this approach presently stands as one of the most promising synthetic routes for SAAs with considerable potential for industrial translation and pilot-scale production, while extensive process optimization is still highly desirable to achieve stable, reproducible large-scale manufacturing of high-performance SAAs with atomically precise structures.

2.2 Galvanic Replacement

GR is based on the principle that a metal can be displaced by another metal with a higher reduction potential, with the reaction occurring at the interface between the substrate and the metal-ion-containing solution. During the GR process, the metal with a lower reduction potential dissolves, whereas the metal with a higher reduction potential is deposited from the solution [69, 98, 99]. Using metals or metal oxides as sacrificial templates, alloy materials can be synthesized via the GR reaction. Meanwhile, the GR reaction depends on the difference in reduction potentials between metal redox couples. According to the Nernst equation, the actual reduction potential is also affected by reaction conditions including temperature, concentration, and pH [100]. Therefore, by adjusting these parameters, the replacement rate of guest metals on the host metal can be controlled, which enables the rational synthesis of SAA materials [101-104].

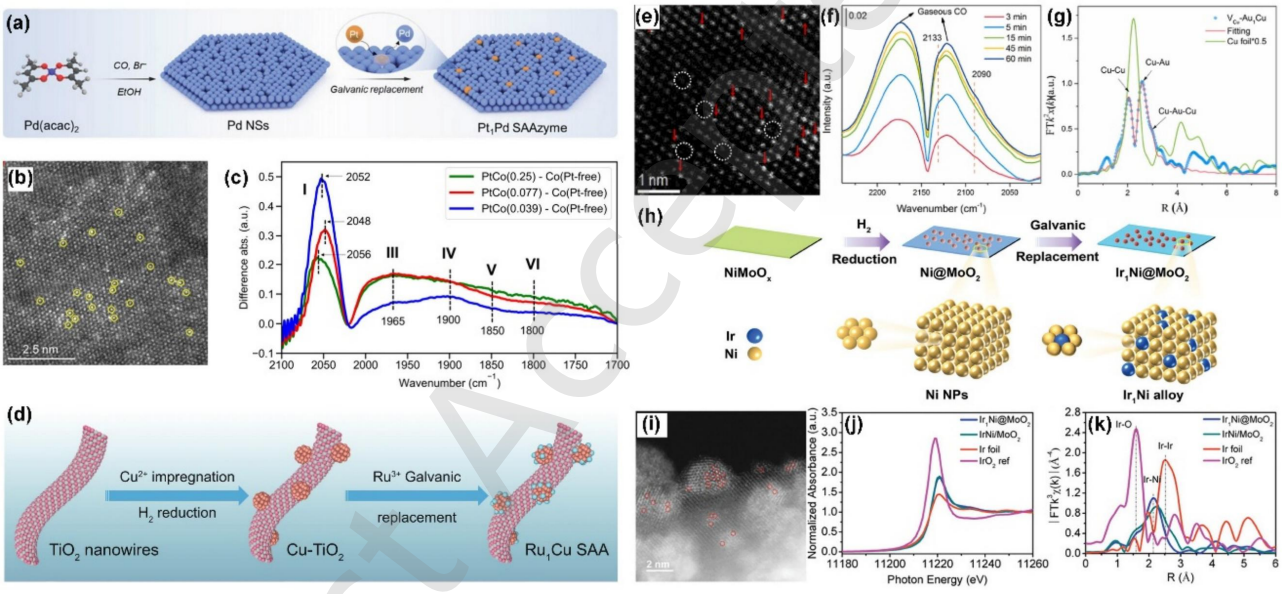

Figure 3. (a). Schematic illustration of the synthetic process for Pt_1Pd SAAzymes. (b) HAADF-STEM image of Pt_1Pd SAAzyme; Reproduced with permission from Ref. [105] Copyright 2023, Wiley-VCH. (c) The difference spectra of CO-FTIR spectra between PtCo(x) and Co (Pt-free) under the CO flow conditions; Reproduced with permission from Ref. [106] Copyright 2025, American Chemical Society. (d) Schematic illustration of preparation processes for Ru_1Cu SAA catalysts, with Ti, O, Ru, and Cu atoms shown as pink, gray, blue, and orange, respectively; Reproduced with permission from Ref. [107] Copyright 2023, Springer Nature. (e) HAADF-STEM image of the V_{Cu}-Au_1Cu SAA. (f) In situ DRIFT spectra of V_{Cu}-Au_1Cu SAA under CO flow at different times. (g) The Cu K-edge EXAFS spectra of the Cu foil and V_{Cu}-Au_1Cu SAA; Reproduced with permission from Ref. [108] Copyright 2022, Elsevier. (h) Schematic diagram for construction of the $Ir_1Ni@MoO_2$ SAA heterostructure. (i) HAADF-STEM image of the $Ir_1Ni@MoO_2$. (j) The Ir L_3-edge XANES spectra of $Ir_1Ni@MoO_2$, $IrNi/MoO_2$ compared with Ir foil and IrO_2 reference. (k) The k^3-weighted EXAFS spectra of $Ir_1Ni@MoO_2$, $IrNi/MoO_2$ compared with Ir foil and IrO_2 reference; Reproduced with permission from Ref. [109] Copyright 2023, Wiley-VCH.

For example, Li et al. prepared a Pt_1Pd SAA nanozyme (SAAzyme) through GR (Figure 3a) [105]. Briefly, Pd nanoscale sheets (NSs) were first prepared by reducing palladium acetylacetonate under the atmosphere of CO at 0.5 MPa and 90 °C, and the surface defects were constructed by dispersing them in ethanol at room temperature. Subsequently, different amounts of H_2PtCl_6 were added to the ethanol solution of Pd NSs. Since the Pt^{4+}/Pt potential (1.420 V) was higher than the Pd^{2+}/Pd potential (0.990 V), the Pd atoms on the surface of Pd NSs were replaced by Pt atoms through GR to yield the final Pt_1Pd SAAzyme. Following Pt doping, the Pt_1Pd SAAzyme retained the irregular hexagonal structure with an average size of approximately 75 nm, consistent with those of Pd NSs. The aberration-corrected HAADF-STEM image showed uniformly distributed bright spots in the irregular hexagonal structures, indicating that Pt existed as single atom in the Pd NSs (Figure 3b). Furthermore, XPS revealed that the binding energy of the Pd *3d* peak in Pt_1Pd SAAzyme decreased by approximately 0.2 eV as the doping amount of Pt increased from 2% to 5%, indicating a charge transfer from Pt single atoms to Pd NSs. Despite that, the binding energy of the Pt 4*f* peak in Pt_1Pd SAAzyme with 2% and 5% Pt loadings was approximately 71.0 eV, corresponding to metallic Pt. In another example, Oda et al. synthesized a series of PtCo(x) alloy catalysts supported on monoclinic-phase ZrO_2 (m-ZrO_2)

via a stepwise method, where *x* meant the Pt loading (wt.%) [106]. Firstly, pure m-ZrO_2 was immersed in a $Co(NO_3)_2$ solution, and the product was reduced by H_2 to prepare m-ZrO_2-supported Co NPs. Subsequently, a certain amount of $Pt(NO_3)_2$ solution was mixed with the ZrO_2-supported Co NPs. Finally, Co atoms were replaced by Pt atoms to yield PtCo(*x*) alloy through a GR reaction. The HAADF-STEM image showed uniformly dispersed bright spots on the surface of Co NPs when the Pt loading was 0.039 wt.%, indicating that the Pt atoms were primarily dispersed on Co NPs in the form of single atoms. However, single Pt atoms began to aggregate into NPs as the Pt loading increased. Specifically, Pt NPs with a size of about 1.3 nm were dominantly observed on Co NPs coupled with some isolated Pt single atoms in PtCo (0.077). As the Pt loading increased to 0.25 wt.%, an extensive number of Pt aggregates were observed on both Co NPs and the m-ZrO_2 support. As SAA catalysts enable efficient CO desorption while Pt ensembles suffer from CO poisoning, PtCo(0.039) shows the highest intensity of band I (~2052 cm^{-1}). With increasing Pt loading, the contribution of band I declines, whereas bands III-VI (1965, 1900, 1850, 1800 cm^{-1}, respectively) increase (Figure 3c). These results indicate that adjusting the loading amount of the guest metal on the host metal support can modify the existing form of the guest metal.

Moreover, the relatively low standard electrode potential of Cu makes Cu an ideal carrier for piggybacking noble metals via GR, because Cu can be readily dissolved under appropriate conditions [110]. For example, Lan et al. developed a stepwise approach to prepare Ru_1Cu SAA supported on TiO_2 nanowires (Figure 3d) [107]. Specifically, a $CuCl_2$ solution was mixed with a TiO_2 nanowire suspension, and the resulting mixture was freeze-dried. Following this, Cu nanoclusters (denoted as Cu NCs) that were loade H_2d onto the TiO_2 nanowire were prepared via thermal reduction of the freeze-dried samples in an H_2/Ar stream at 300°C for 2h. Finally, the Ru_1Cu SAA was fabricated by GR, where some Cu atoms in the Cu NCs that were anchored on TiO_2 nanowires were replaced by Ru^{3+} from the $RuCl_3$ solution. HAADF-STEM image showed many atomic-sized bright spots on the Cu NCs anchored on TiO_2 nanowires in Ru_1Cu SAA, attributed to single Ru atoms. Furthermore, the Ru K-edge FT-EXAFS analysis revealed a peak at 2.22 Å in Ru_1Cu SAA, distinct from the 2.39 Å peak in Ru foil (assigned to Ru-Ru scattering). This peak could be tentatively assigned to Ru-Cu scattering, indicating that Ru dopants were atomically dispersed in the Cu matrix. Zhang et al. also fabricated a V_{Cu}-Au_1Cu SAA with Cu vacancies (V_{Cu}) by dropping an aqueous solution of $HAuCl_4 \cdot 3H_2O$ into Cu NSs for GR, and subsequent acid-etching dealloying treatments [108]. In the aberration-corrected HAADF-STEM image of V_{Cu}-Au_1Cu, atomic-sized bright spots (red arrows) that corresponded to isolated Au atoms were uniformly dispersed on Cu crystals, while lattice defects (white circles) with no atomic arrangement manifested the Cu vacancies (Figure 3e). In situ CO-DRIFT of V_{Cu}-Au_1Cu also showed a small peak at 2133 cm^{-1}, corresponding to the Au^+-CO species, which demonstrated the atomically dispersed of Au in V_{Cu}-Au_1Cu (Figure 3f). Furthermore, the Cu K-edge EXAFS spectra revealed several peaks at 2.1 Å, 2.5 Å and 2.9 Å, corresponding to the Cu-Cu, Cu-Au and Cu-Au-Cu coordination, respectively, supporting the formation of Au-Cu alloys (Figure 3g). Notably, XPS revealed that the binding energies of Cu^0 for V_{Cu}-Au_1Cu SAAs have a 0.21eV positive shift compared with Cu or V-Cu NSs, indicating that the electrons are transferred from Cu to Au atoms. In a similar strategy, Wang et al. prepared a Ir_1Ni SAA supported on conductive MoO_2 oxides (denoted as $Ir_1Ni@MoO_2$ SAA) (Figure 3h) [109]. Firstly, since Ni has a higher reducibility than Mo, under an H_2 atmosphere, the oxidized Ni at the surface of $NiMoO_x$ was able to be reduced to Ni NPs and enriched on the MoO_2 support to form $Ni@MoO_2$ heterostructure. Subsequently, an aqueous H_2IrCl_6 solution was slowly added to the suspension of $Ni@MoO_2$ under an Ar flow. Through the GR reaction, Ni atoms were replaced by Ir to produce the $Ir_1Ni@MoO_2$ SAA. The HAADF-STEM image showed that bright spots, namely, Ir atoms were uniformly distributed on the $Ir_1Ni@MoO_2$ heterostructure (Figure 3i). The Ir L_3-edge XANES spectra showed that the white-line peak intensity of $Ir_1Ni@MoO_2$ was close to that of Ir foil, confirming the metallic state of Ir (Figure 3j). Meanwhile, the Ir L_3 edge FT-EXAFS spectra showed a main peak at 2.13 Å belonging to Ir-Ni coordination bond, and no Ir-Ir bond (2.52 Å) was detected, confirming the formation of $Ir_1Ni@MoO_2$ SAA (Figure 3k). Moreover, XPS spectra of Ni 2*p* and Ir 4*f* revealed that the binding energy of Ni^0 exhibited a positive shift from 852.3 to 852.5 eV, while that of Ir^0 showed a negative shift from 60.9 to 60.5 eV, indicating electron transfer from Ni to Ir.

Galvanic replacement enables spontaneous, ambient-condition fabrication of SAAs via redox reactions driven by reduction potential differences between host and guest metals, featuring simple operation and no need for external energy input. However, this method is strictly limited by the thermodynamic requirements of metal pairs, faces challenges in maintaining atomic dispersion at high guest loadings, and suffers from poor product uniformity and batch-to-batch consistency during scale-up. Thus, it is currently only suitable for lab-scale synthesis of specific SAAs and fundamental studies, and is unfit for large-scale industrial production.

2.3 Electrochemical reconstruction

Electrochemical reconstruction is a technique that uses electrochemical reactions to alter the surface structure of a material. Under controlled potential or current, the precursor materials undergo dynamic surface restructuring, including atomic rearrangement, defect generation, and partial oxidation/reduction [111]. The applied potential regulates the adsorption-desorption energy and migration barrier of surface metal atoms, favoring atomic dispersion rather than aggregation [112]. Moreover, the strong metal-metal interaction and electronic modulation between the host and guest metal atoms can be enhanced under electrochemical conditions, stabilizing isolated metal single atoms. This kinetic and thermodynamic controllability makes electrochemical reconstruction a reliable approach for constructing stable and uniformly dispersed SAAs [113, 114].

For example, Cao et al. synthesized a series of BiCu-SAA electrocatalysts with Bi single-atom uniformly dispersed on Cu substrates through in situ electrochemical reconstruction

[115]. Briefly, bismuth-modified CuS (designated as Bi-CuS) with nanoflower architectures were first synthesized via thermal decomposition of an ethylene glycol solution containing CuTuCl and Bismuth(III)diethyldithiocarbamate at 120 °C for 2h, followed by formulation into ink droplets for deposition onto glassy carbon/carbon paper electrodes. Subsequently, the Bi-CuS electrode was *in situ* electrochemically treated for structural reconstruction to get the BiCu-SAA catalyst at -0.9 V vs Reversible hydrogen electrode (RHE) in CO_2-saturated 0.1 M $KHCO_3$ electrolyte. After electrochemical reconstruction, the HAADF-STEM image of BiCu-SAA showed uniformly dispersed bright dots, indicating the single-atomic form of Bi in the catalyst. Meanwhile, its corresponding line profiles from HAADF intensity analysis revealed that the distance between Bi and Cu peaks was consistent with the Cu lattice spacing, implying that Bi atoms were dispersed by replacing Cu atomic positions rather than occupying interstitial sites within the Cu(111) facet (Figure 4a-c). Furthermore, the binding energies of normalized absorption peaks at the Cu K-edge XANES decreased from ~8985 eV for open circuit potential (OCP) to ~8980 eV at -0.9 V or even more negative potentials, indicating that the Bi-CuS precursor could be reconstructed and efficiently converted to metallic Cu towards the formation of BiCu-SAA catalyst at -0.9 V (Figure 4d). Cu K-edge XANES analysis demonstrated that the incorporation of Bi induced a shift of the absorption edge of BiCu-SAA toward lower energy relative to Cu-Nano, signifying the presence of electronic interactions between single-atomic Bi and the Cu substrate (Figure 4e). Utilizing a similar approach, Zheng et al. reported a Pb single-atom alloyed Cu catalyst (Pb_1Cu SAA) [116]. Firstly, a Cu-Pb precursor was synthesized via an epoxide gelation method using $CuCl_2$ and $Pb(NO_3)_2$ as raw materials, which yielded nanohybrid structures composed of $Cu_2(OH)_3Cl$ and $PbCl_2$. Subsequently, the as-prepared Cu-Pb precursor was in situ electrochemically reduced at a constant current density of -500 mA cm^{-2} in CO_2-saturated 0.5 M $KHCO_3$ electrolyte for 30 min to form the Pb_1Cu SAA catalyst. Following electrochemical reconstruction, HAADF-STEM images showed uniformly distributed bright spots on the catalyst, indicating that Pb atoms with a larger proton number were distributed as single-atoms in the Cu matrix (Figure 4f, g). The Pb L_3-edge EXAFS curve of Pb_1Cu exhibited two peaks at around 1.93 and 2.73Å, attributed to Pb-O and Pb-Cu bonds. No Pb-Pd bond was detected, further verifying the presence of atomically dispersed Pb atoms (Figure 4h).

In another example, an oxygen-pinned (O_p)-Ag_1In SAA catalyst was prepared by Fang et al [117]. Specifically, a Ag_1-In_2O_3 precursor was first prepared via a stepwise hydrolysis-calcination process using $InCl_3$ and $AgNO_3$ as raw materials. Subsequently, the precursor ink was uniformly drop-coated onto hydrophobic carbon paper, and reduced at -0.9 V vs. RHE potential for 1 h to finally obtain the O_p-Ag_1In SAA catalyst. In the HAADF-STEM image after electrochemical reconstruction, the isolated dark spots were identified as single Ag atoms based on the Z-contrast difference (where light Ag atoms appear darker than heavy In atoms) (Figure 4i). Meanwhile, the corresponding intensity line profiles showed that the signal intensity of Ag sites was lower than that of In sites, further indicating a uniform distribution of Ag atoms in the In substrate. (Figure 4j). The EXAFS spectra of Ag K-edge showed that there were only peaks at 2.04 Å and 2.89 Å, attributed separately to Ag-O and Ag-In bond, respectively (Figure 4k). Furthermore, the In 3*d* XPS results showed that O_p-Ag_1In moved 0.3 eV to a lower binding energy than that in In, which revealed the electron transfer interaction between the Ag single atom and the In substrate. In addition, Zhao et al. prepared a nanoporous Cu_1Au SAA (np-Cu_1Au SAA) via a stepwise chemical and electrochemical dealloying method (Figure 4l) [118]. First, all aluminum and part of copper in the precursor $Al_{80}Cu_{15}Au_5$ were removed sequentially with NaOH and HNO_3 solution to obtain bimodal np-$Au_{65}Cu_{35}$ alloy with second-order ligand/pore size distribution. Subsequently, an electrochemical dealloying process was performed via cyclic voltammetry between 0 and 1.0 V vs. RHE in 0.1 mol L^{-1} $HClO_4$ to gradually remove copper atoms. During the cyclic process, active Cu atoms were dissolved from np-$Au_{65}Cu_{35}$, leaving the coral-like np-Cu_1Au SAA. The Au L_3-edge XANES result showed that the white line peak of np-Cu_1Au SAA was close to Au foil, suggesting the metallic state of Au. The Cu K-edge XANES spectra showed that the absorption edge of np-Cu_1Au SAA was located between the Cu foil and CuO, indicating that the valence of Cu was between 0 and +2. Furthermore, the Cu K-edge EXAFS spectrum of np-Cu_1Au SAA exhibited two coordination peaks belonging to Cu-Au and Cu-O, which was different from those of CuO and Cu, implying the formation of CuAu alloy (Figure 4m). Moreover, the absence of Cu-Cu bonds in EXAFS fitting results further confirmed that the Cu atoms were atomically dispersed in the Au lattice, forming the Cu_1Au SAA after electrochemical reconstruction.

The existence forms of guest metals (atomically dispersed, clustered, or particulate) and host metals (metallic elemental state or metal oxides) are closely related to the level of electrode potential and the concentration of metal precursors in the solution. As mentioned above, when Cao et al. achieved the electrochemical reconstruction of Bi-CuS to BiCu-SAA, the Cu K-edge XANES spectra exhibited characteristic peaks similar to those of Cu foil only when the potential was more negative than -0.6 V vs. RHE [115]. This indicates that a sufficiently negative potential is required to reduce Cu to its metallic state for the formation of SAA. Similarly, in their investigation of the electrochemical reconstruction of the Ag_1-In_2O_3 precursor to O -Ag_1In SAA, Fang et al. determined via cyclic voltammetry curves that the potential needs to be more negative than -0.6 V vs. RHE to reduce In^{3+} to metallic In [117]. In other cases, Wang and coworkers prepared an Ag single-atoms-modified Cu catalyst (denoted as AgCu-SAA) and an Ag NPs-modified Cu catalyst (denoted as AgCu-Nano) via electrochemical reconstruction by changing the concentration of the guest metal precursor [119]. Specifically, 3 mmol $CuCl_2{\cdot}2H_2O$ and 0.2 mmol $AgNO_3$ were dissolved in 2 mL isopropanol in a vial. Under bath sonication, 2 mL propylene oxide and 0.2 mL H_2O were then successively added. The mixture was aged and dried to form a Cu-Ag precursor. Subsequently, the as-obtained Cu-Ag precursor was drop-coated on the carbon fiber paper and *in situ* electrochemically reduced to an AgCu-SAA catalyst (with an Ag concentration of 3.3 wt.%) at a

constant current density of 500 mA cm^{-2} for 30 min in a flow cell. When only the addition amount of $AgNO_3$ was increased to 0.6 mmol, the existing state of metallic Ag on Cu changed to Ag NPs, resulting in the AgCu-Nano catalyst with an Ag concentration of 9.3 wt.%. This is because the change in Ag content in the precursor exceeds the thermodynamic limit for the monatomic dispersion of Ag on the Cu matrix, causing the excess Ag atoms to agglomerate into NPs.

Electrochemical reconstruction enables in situ fabrication of SAAs on conductive substrates, with precise regulation of guest metal dispersion via tuning electrode potential, and features simple operation, low cost and high atomic utilization. However, this method is limited to conductive supports, faces challenges in maintaining product uniformity during scale-up due to uneven potential and charge distribution, and its structural control mechanism for complex multi-metal systems remains to be fully clarified. Thus, this approach holds great promise for the batch preparation of electrocatalytic SAAs, yet it remains a long way from industrial implementation.

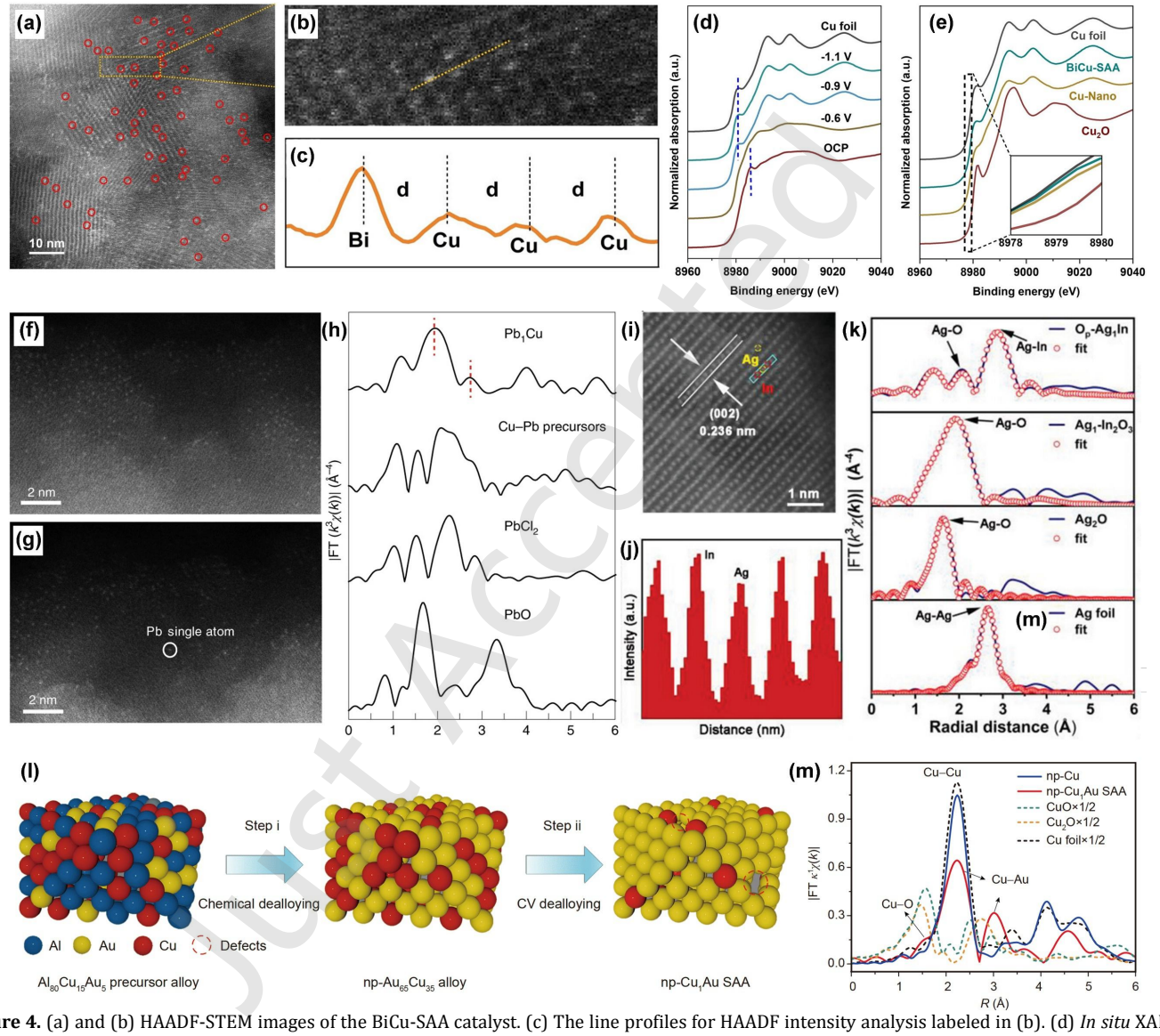

Figure 4. (a) and (b) HAADF-STEM images of the BiCu-SAA catalyst. (c) The line profiles for HAADF intensity analysis labeled in (b). (d) *In situ* XANES spectra at Cu K-edge for the BiCu-SAA catalyst. (e) *In situ* Cu K-edge XANES spectra of the BiCu-SAA and Cu-Nano catalysts at an applied potential of -1.10 V vs. RHE. Reproduced with permission from Ref. [115] Copyright 2023, Wiley-VCH. (f) and (g) HAADF-STEM images of the Pb_1Cu catalyst. The white circle highlights the single-dispersed Pb atom. (h) Ex situ EXAFS spectra at the Pb L_3-edge of the Pb_1Cu catalyst. The spectra of $PbCl_2$ and PbO are shown as references. Reproduced with permission from Ref. [116] Copyright 2021, Springer Nature. (i) Spherical aberration-corrected high-resolution HAADF-STEM image, and (j) corresponding intensity line profile for Op-Ag_1In. (k) Ag K-edge EXAFS spectra of Op-Ag_1In and reference samples. Reproduced with permission from Ref. [117] Copyright 2024, Wiley-VCH.(l) Schematic illustration for the preparation of np-Cu_1Au SAA with surface defects. (m) Fourier transforms of Cu K-edge EXAFS spectra for np-Cu_1Au SAA and comparison samples. Reproduced with permission from Ref. [118] Copyright 2021, Science China Press.

2.4 Sequential reduction

Sequential reduction is an effective technique for the preparation of SAA catalysts and is particularly suitable for those applications that require precise control of the position of metal atoms and alloy composition [113, 120]. Highly dispersed SAAs are formed by the sequential introduction of different metal precursors and their progressive reduction [121]. Specifically, by controlling the reduction sequence and rate, the first metal is preferentially reduced and self-assembles to form isolated nucleation sites, which may be supported or self-supported. Since the adsorption energy of guest metal atoms on the host metal

surface is significantly higher than that on the support or in homogeneous phase, independent nucleation of guest metal atoms is thermodynamically suppressed [122, 123]. Therefore, the second metal is subsequently deposited atomically onto the preformed host metal surface under mild reduction conditions, avoiding excessive agglomeration. Meanwhile, the strong metal-support interaction and electronic coupling between two metals stabilize the single-atom dispersion in SAAs.

For example, Yu et al. synthesized Au_xCu SAA aerogels (Au_xCu SAAs) by a facile $NaBH_4$ reduction approach (Figure 5a) [124]. Briefly, Cu aerogels were firstly prepared via a template-free self-assembly process, with $CuCl_2$ solution serving as metal precursors and $NaBH_4$ as a reducing agent. Subsequently, $HAuCl_4$ was induced to Cu aerogels, followed by a secondary $NaBH_4$ reduction. During the process, a number of hydrogens generated by the hydrolysis of $NaBH_4$ served as gas templates to directly form the porous nanostructure. By varying the concentrations of $HAuCl_4$ from 0.25 to 1 mM, a series of Au_xCu SAAs were synthesized. These samples with low, medium, and high Au concentrations were denoted as Au_1Cu SAAs (0.59 wt.% Au), Au_mCu SAAs (1.36 wt.% Au), and Au_hCu SAAs (2.59 wt.% Au), respectively. The aberration-corrected HAADF-STEM images of Au_mCu SAA revealed a homogeneous distribution of bright spots, and the line profiles from the HAADF intensity at the corresponding spots exhibited a trend of strong Au and weak Cu signals, indicating that Au was uniformly dispersed on the Cu surface in a single-atom form (Figure 5b-d). The Au L_3-edge XANES spectra of Au_mCu SAAs revealed that the white line intensity of Au_mCu SAAs lay between that of Au foil and Au_2O_3, suggesting that the valence state of Au was between 0 and +3 (Figure 5e). Furthermore, the Au L_3-edge EXAFS spectrum showed a prominent peak at 2.64 Å and a weak peak at 1.95 Å, corresponding to the Au-Cu and Au-O bond, respectively. And no peaks associated with Au-Au contribution distance (>2.7 Å) was discerned, which proved the atomic distribution of Au and the formation of SAA structure (Figure 5f). In another example, Pan et al. synthesized a UiO-66-NH_2 confined $Pd_{10}@Pt_1$ SAA catalyst by using a similar approach [125]. The $Pd(NO_3)_2$ solution was first impregnated into the pores of UiO-66-NH_2 and subsequently reduced by NH_3BH_3, with Pd^{2+} being reduced to Pd NPs to generate Pd_{10}/UiO-66-NH_2. Along with the depletion of NH_3BH_3, certain amounts of H_2PtCl_6 were added to the synthetic system. The surface Pd-H species generated during the hydrolysis of NH_3BH_3 were functioned as both nucleation seeds and reductants for H_2PtCl_6, leading to the formation of a $Pd_{10}@Pt_1$ SAA within UiO-66-NH_2 ($Pd_{10}@Pt_1$/UiO-66-NH_2) (Figure 5g). In the HAADF-STEM image of $Pd_{10}@Pt_1$/UiO-66-NH_2, uniformly dispersed bright spots were clearly observed due to the fact that Pt had a larger proton number than Pd, implying that Pt was atomically dispersed on the Pd surface (Figure 5h). Compared to the Pt^0 4 $f_{7/2}$ peak at 70.9 eV for Pt_1/UiO-66-NH_2, the $Pd_{10}@Pt_1$/UiO-66-NH_2 presents a lower binding energy (70.35 eV), reflecting that the Pt surface in Pd@Pt NPs becomes electron-rich. The direction of electron transfer between these metals is opposite to that reported by Li et al., which may be due to the influence of the carrier on the electron transfer of the metals [105]. Furthermore, the Pt L_3-edge EXAFS spectrum of $Pd_{10}@Pt_1$/UiO-66-NH_2 showed a prominent peak at ~2.7 Å and a weak peak at 1.5 Å, corresponding to the Pt-Pd and Pt-O bond, respectively. No peaks associated with Pt-Pt was discerned, confirming that the SAA structure was formed in $Pd_{10}@Pt_1$/UiO-66-NH_2 (Figure 5i).

Using the standard electrode potential difference of the metals, it is possible to realize that two or more metals are successively reduced on the carrier to obtain SAAs. Ren et al. fabricated a $Cu_{97}Sn_3$ SAA catalyst by reducing an aqueous mixture of $CuCl_2$ (300 mg) and $SnCl_2$ (12.3 mg) in 5 mol L^{-1} $NaBH_4$ (Figure 5j) [126]. Owing to the more negative standard electrode potential of Sn^{2+} relative to Cu^{2+} (Sn^{2+}+ $2e^- \rightleftharpoons Sn$, E^0 = -0.13 V vs. Standard Hydrogen Electrode (SHE); Cu^{2+}+ $2e^- \rightleftharpoons Cu$, E^0 = 0.34 V vs. SHE), the reduction of Cu^{2+} took place first, followed by the deposition of Sn on Cu surface (or near the surface). In addition, the Cu@Sn core-shell bulk alloy ($Cu_{70}Sn_{30}$) also could be obtained by controlling the content of $CuCl_2$ (300 mg) and $SnCl_2$ (17.2 mg). The HAADF-STEM images of $Cu_{97}Sn_3$ showed that there were uniformly distributed bright spots on the Cu surface, indicating the atomic dispersion of Sn (Figure 5k). Atom probe tomography was employed to further investigate the distribution of Sn atoms on the surface of Cu particles of $Cu_{97}Sn_3$. A 2D Sn density contour map was obtained by projecting the entire Sn atoms on the xy plane. To highlight the position of the two elements, Sn atoms were represented by larger green dots and Cu atoms were displayed by smaller purple dots (Figure 5l). As a result, high surface densities of isolated Sn atoms were formed on the surface of Cu NPs to evolve exposed Cu-Sn atomic interfaces, which was the convincing evidence of the SAAs configuration. Furthermore, the Cu K-edge XANES spectra revealed that the near-edge positions of Cu_{100}, $Cu_{97}Sn_3$, and $Cu_{70}Sn_{30}$ catalysts were slightly higher than that of Cu foil, indicating that the bulk Cu in the three samples was in the metallic state with only surface been oxidized to Cu^+. The Cu K-edge FT-EXAFS spectra of $Cu_{97}Sn_3$ exhibited two major peaks at 1.5 and 2.2 Å, corresponding to Cu-O and Cu-Cu coordination shells, respectively. The Cu-O peak was only observed in $Cu_{97}Sn_3$ and Cu_{100} catalysts, while the $Cu_{70}Sn_{30}$ displays similar peak shape compared to Cu foil with peak intensity from 4 to 5 Å significantly suppressed. This result showed that the surface of $Cu_{70}Sn_{30}$ was completely coated by tin shells by increasing the concentration of Sn.

Sequential reduction enables flexible modulation of the molar ratio of host and guest metals in SAAs, and catalysts with well-defined metal component gradients can be fabricated by regulating the reduction sequence and reaction kinetics of distinct metal precursors. Despite this unique merit in component regulation, the sequential reduction method is associated with cumbersome operational procedures involving multi-step reduction and post-treatment processes. Furthermore, the precise control of each reduction step is highly dependent on stringent reaction conditions (e.g., temperature, reducing agent concentration), and the uniformity of SAA products is difficult to ensure during scale-up synthesis due to the inhomogeneous mass and heat transfer in large-scale

reactors. Additionally, the stepwise reaction mode results in a relatively long overall synthesis cycle and low production efficiency. Accordingly, this method is currently only applicable for the lab-scale preparation of SAAs with complex multi-metal components.

2.5 Atomic Layer Deposition

ALD is an advanced thin film deposition technique, which is a cyclic process based on sequential self-limiting molecular-level surface reactions between gas phase chemical precursors and a solid substrate surface [127-129]. In the ALD reaction chamber, the host metal precursor vapor reacts with surface functional groups or adsorbs on the high-energy defect sites of support, forming metal nanoparticles. After that, unreacted precursor and byproducts are purged using a specific gas such as N_2. Subsequently, the as-obtained host-metal-modified support is exposed to the guest metal precursor vapor, allowing guest metal atoms to deposit uniformly onto the host metal surface. By adjusting the exposure time of each metal precursor on the support, the metal loading can be well controlled, thus allowing the successful preparation of SAAs [130, 131].

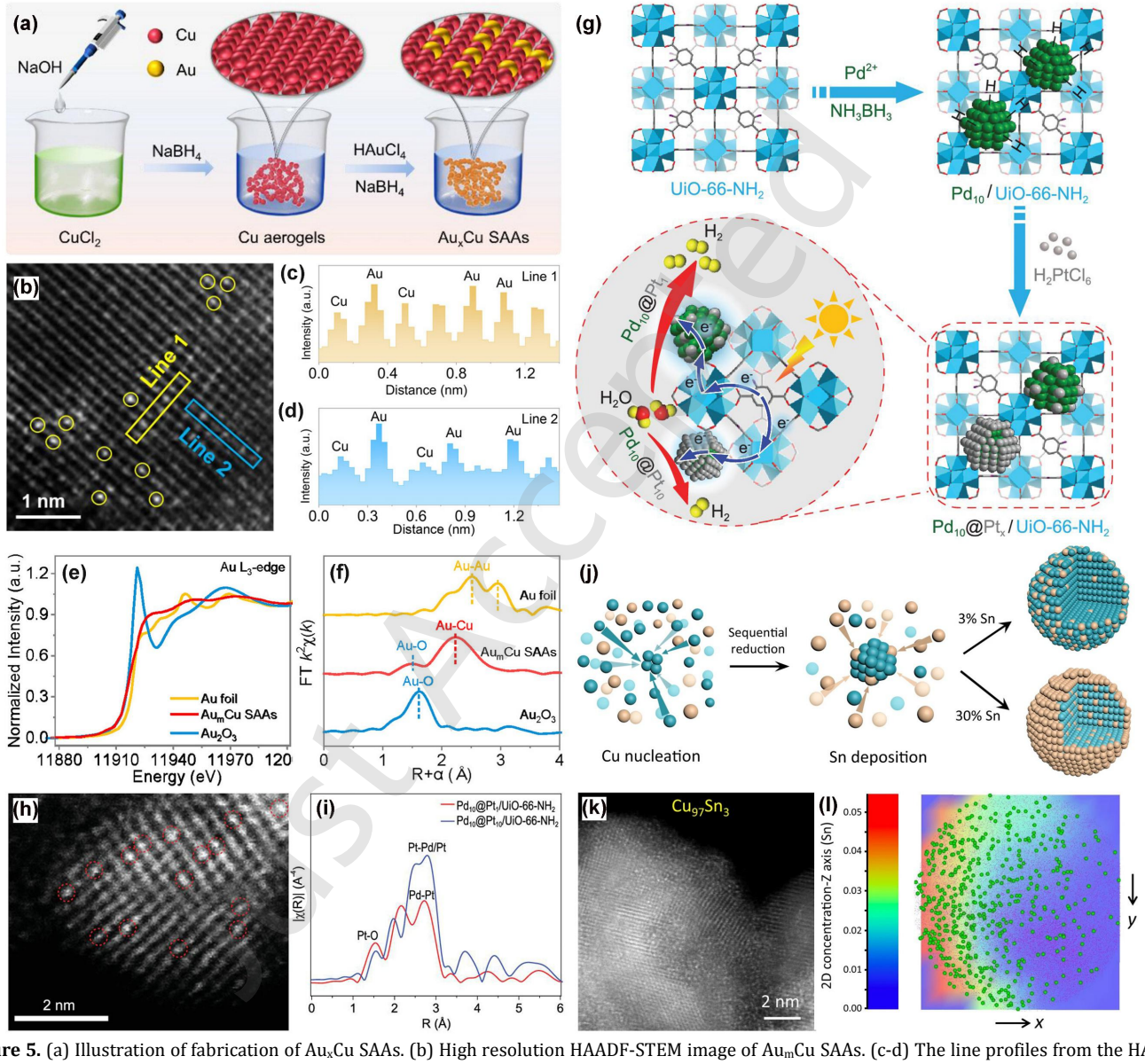

Figure 5. (a) Illustration of fabrication of Au_xCu SAAs. (b) High resolution HAADF-STEM image of Au_mCu SAAs. (c-d) The line profiles from the HAADF intensity analysis labeled in (b). (e) Au L_3-edge normalized XANES spectra, and (f) Au L_3-edge EXAFS spectra in R space for Au_mCu SAAs, Au foil, and Au_2O_3; Reproduced with permission from Ref. [124] Copyright 2024, Wiley-VCH. (g) Schematic illustration for the synthetic strategy of $Pd_{10}@Pt_x/UiO\text{-}66\text{-}NH_2$. (h) HAADF-STEM image of $Pd_{10}@Pt_1/UiO\text{-}66\text{-}NH_2$. The single Pt atoms are highlighted by the red circles and the lattice fringes are from Pd while the MOF is shaded in black background. (i) The Pt L_3-edge FT-EXAFS spectra for $Pd_{10}@Pt_1/UiO\text{-}66\text{-}NH_2$ and $Pd_{10}@Pt_{10}/UiO\text{-}66\text{-}NH_2$; Reproduced with permission from Ref. [125] Copyright 2020, China Science Publishing & Media Ltd. (j) Schematic illustration of the Cu-Sn nanoparticle formation via the sequential reduction. (k) HAADF-STEM image of $Cu_{97}Sn_3$. (l) The Sn concentration 2D contour projected on xy plane indicate a curved Sn-rich band, which corresponds to the Cu particle surface, and the low dopant region refers to the inside of the Cu particle; Reproduced with permission from Ref. [126] Copyright 2021, Springer Nature.

For example, Zhang et al. fabricated a Pt/Pd SAA catalyst by depositing single-atom Pt onto Pd octahedrons NPs supported on nitrogen-doped carbon nanotubes (NCNTs) via a stepwise wet-chemical and ALD method (Figure 6a) [132]. Specifically, octahedra Pd NPs were first prepared via a wet-chemical method using Pd cubes as seeds and Na_2PdCl_4 as the metal precursor. The resulting products were then loaded onto the surface of NCNTs via 30 min ultrasonic to obtain the Pd/NCNTs support for Pt deposition. Finally, the Pt/Pd SAA was prepared via four ALD cycles in an ALD

reactor chamber, each consisting of a 30 s exposure of the gaseous Pt precursor (trimethyl-(methylcyclopentadienyl)-platinum(IV)) to the Pd/NCNTs support, followed by a 10 s purge with high-purity N_2. In a similar ALD method, the Pt/Pd catalyst with a core-shell structure (denoted as Pd@Pt) were prepared by replacing Pd octahedrons with Pd nanocubes. The atomic-resolution HAADF-STEM images of Pt/Pd SAA revealed a few brighter atoms (green circles) and some individual bright spots (red circles) on octahedral Pd NPs, indicating the coexistence of Pt clusters and single Pt atoms (Figure 6b, c). In contrast, the atomic-resolution HAADF-STEM images of Pd@Pt revealed that the edges and corners of the cubic Pd NPs appeared brighter than the bulk, suggesting that a ~2-3 atomic layer-thick Pt shell was formed on cubic Pd NPs. Octahedral Pd NPs with abundant exposed (111) facets of low surface energy were supposed to adsorb fewer precursors, leading to Pt atoms in an isolated state However, cubic Pd NPs with abundant exposed (100) facets of high surface energy adsorbed more Pt precursors, which tended to form a uniform Pt shell. Further study of the CN revealed that the Pt-Pt CN for the Pt/Pd SAA was 1.7, further confirming the formation of Pt isolated atoms and clusters instead of a Pt thin shell on octahedral Pd NPs. Using a similar approach, Wang et al. prepared a Pd_1Ni SAA via depositing Pd single-atoms in the outermost layer of Ni NPs supported on SiO_2 (Ni/SiO_2) by using a palladium precursor of hexafluoroacetylacetate ($Pd(hfac)_2$) [133]. Specifically, the Ni/SiO_2 was first fabricated via the deposition-precipitation method using $Ni(NO_3)_2$ and spherical SiO_2 as raw materials. Then, in the ALD reaction chamber at 150 ℃, the Ni/SiO_2 support underwent ALD cycles with a timing sequence consisting of 120 s $Pd(hfac)_2$ exposure, 200 s N_2 purge, 60 s H_2 exposure, and 200 s N_2 purge. Following 5 ALD cycles, the Pd_1Ni SAA (5Pd-Ni/SiO_2) catalyst with 1 wt.% Pd loading was obtained (Figure 6d, e). Due to the much larger Z-value of Pd than that of Ni, brighter spots were observed in the HAADF-STEM image of 5Pd-Ni/SiO_2, indicating that Pd atoms were atomically dispersed on the Ni NPs (Figure 6f). Furthermore, the Pd K-edge FT-EXAFS spectrum of 5Pd-Ni/SiO_2 showed a dominant peak at 2.12 Å, which was mainly attributed to Pd-Ni coordination, with no detectable Pd-Pd peak (Figure 6h). In contrast, large Pd ensembles (or even a continuous shell) were produced by multiple ALD cycles, as observed for 20Pd-Ni/SiO_2. The HAADF-STEM image of this sample showed some large bright spots, and Pd K-edge FT-EXAFS spectra exhibited intense Pd-Pd peaks at 2.52 Å (Figure 6g, h). The aforementioned cases demonstrated that controlling the type of substrate facets and the number of ALD cycles enabled effective regulation of the guest metal's existence form on the substrate. Moreover, *in situ* Pd 3*d* XPS measurements revealed that, over 5Pd-Ni/SiO_2, a prominent positive shift of the Pd 3*d* binding energy by 0.7 eV was observed relative to Pd/SiO_2, indicating charge transfer from Pd to Ni. This positive shift gradually became less pronounced with increasing Pd coverage, implying that the surface electronic structure was approaching that of pure Pd.

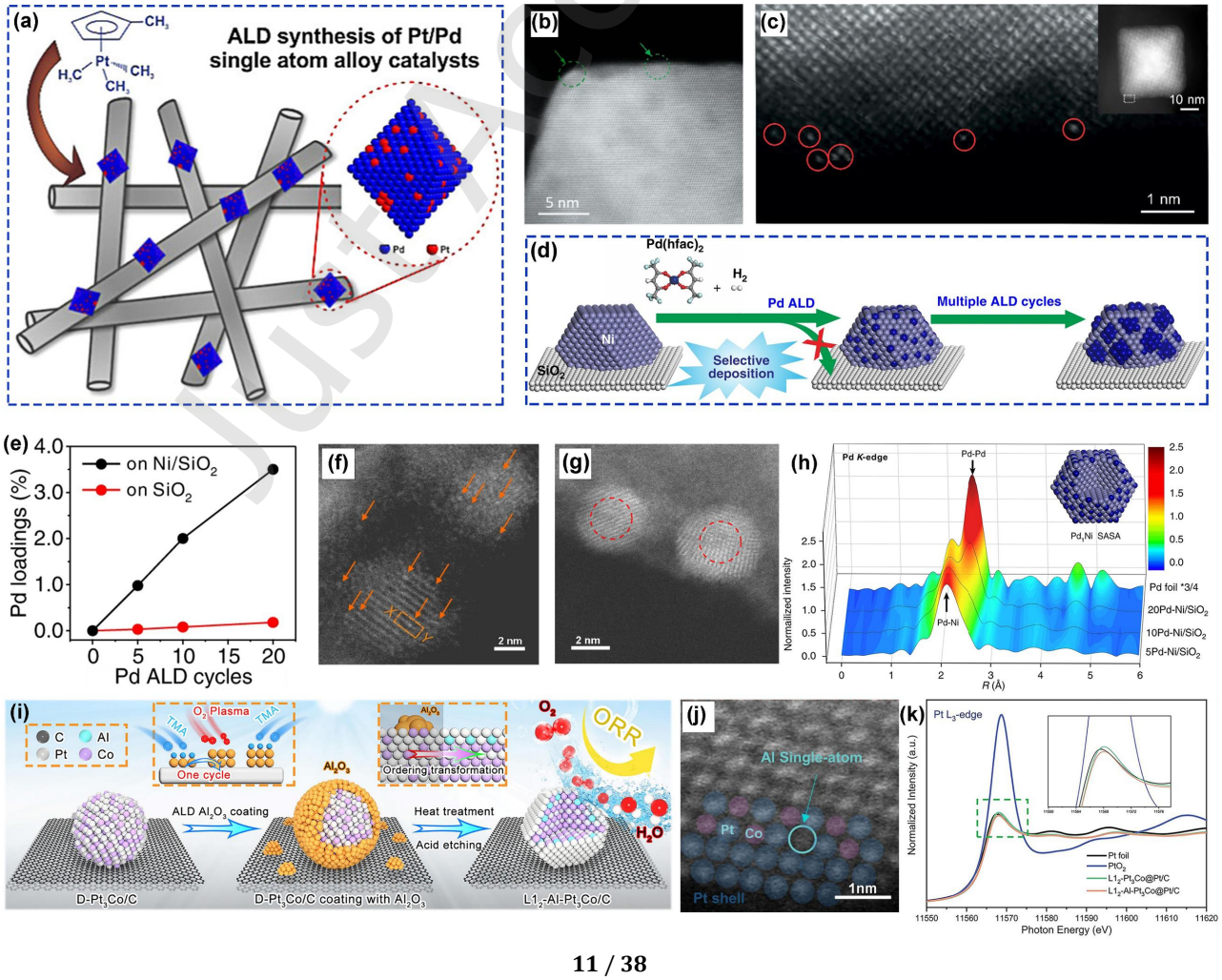

Figure 6. (a) Schematic illustration of synthesis of Pt/Pd SAA. (b) Atomic-resolution STEM image of an individual octahedral Pt/Pd SAA particle. (c) High-resolution STEM image showing the surface of one individual octahedral Pt/Pd SAA (inset), indicating the formation of Pt isolated atoms on Pd particles; Reproduced with permission from Ref. [132] Copyright, 2019 American Chemical Society. (d) Schematic illustration of synthesis of xPd-Ni/SiO_2 SAA. (e) Pd loadings in the xPd-Ni/SiO_2 and xPd/SiO_2 samples determined by inductively coupled plasma atomic emission spectroscopy. HAADF-STEM images of (f) 5Pd-Ni/SiO_2 and (g) 20Pd-Ni/SiO_2. (h) *In situ* Fourier transforms EXAFS spectra of the xPd-Ni/SiO_2 samples (x = 5, 10, and 20) and Pd foil reference in the real space at the Pd K-edge. Reproduced with permission from Ref. [133] Copyright 2019, Springer Nature. (i) Schematic illustration of the preparation of $L1_2$-Al-Pt_3Co@Pt/C catalyst. (j) HAADF-STEM image of $L1_2$-Al-Pt_3Co@Pt/C along [110] direction. (k) Normalized Pt L_3 XANES spectra of $L1_2$-Al-Pt_3Co@Pt/C and reference samples; Reproduced with permission from Ref. [134] Copyright 2024, Elsevier.

In a SAA system, the guest single-atom displays a direct influence on the structure of host metal, and also provides an opportunity to modify the host metal such as Pt-based intermetallic NPs. For example, Wu et al. constructed a strain-regulated Pt-based intermetallic catalysts ($L1_2$-Al-Pt_3Co@Pt/C) by introducing Al single-atom into the Pt_3Co alloy core via ALD (Figure 6i) [134]. Specifically, disordered-Pt_3Co/C (D-Pt_3Co/C) was first prepared by mixing disordered-Pt_3Co alloy NPs with Ketjen-300 J carbon in hexane, followed by stirring, washing, and drying. Then, in the ALD reaction chamber at 200 ℃, the D-Pt_3Co/C underwent ALD cycles with a timing sequence consisting of 20 ms Al precursor exposure, 20 s Ar purge, 10 s O_2: Ar (10 sccm:10 sccm) plasma (300 W) exposure, and 20 s Ar purge. After 8 ALD cycles, the resulting products were annealed at 700 °C in a 5% Ar/H_2 atmosphere and acid-etched with 0.5 M H_2SO_4, yielding the $L1_2$-Al-Pt_3Co@Pt/C. The HAADF-STEM images showed alternating intensity distributions due to the Z-contrast difference between Co (27), Al (13) and Pt (78), indicating that Al was embedded in the lattice of Pt_3Co NPs as single atoms by replacing Co atoms (Figure 6j). The Pt L_3-edge XANES spectra showed that introducing Al atoms decreased the white-line peak intensity of $L1_2$-Al-Pt_3Co@Pt/C compared to $L1_2$-Pt_3Co@Pt/C, implying electron transfer from Al to Pt. These results suggested that Al and Pt formed a SAA structure (Figure 6k). Furthermore, the Pt L_3-edge EXAFS spectra revealed a longer Pt-Pt bond length in $L1_2$-Al-Pt_3Co@Pt/C (2.723 Å) than in $L1_2$-Pt_3Co@Pt/C (2.719 Å), implying that approximately 0.2% lattice strain was introduced into the Pt layer after the incorporation of Al atom. This phenomenon arose because the substitution of Al atoms for Co sites relieved the over-compression of the Pt_3Co intermetallic compound.

ALD affords precise atomic-level modulation, thus fabricating SAAs with homogeneous composition, well-defined structural characteristics and excellent reproducibility. Notwithstanding these merits, the ALD approach suffers from relatively high manufacturing costs, which arises from the stringent reaction conditions required and the dependence on specialized, high-precision equipment. Furthermore, the ALD process entails repetitive cycles of metal precursor deposition and inert gas purging to ensure atomic-scale uniformity, resulting in a notably low synthetic efficiency. For these reasons, ALD is not yet feasible for large-scale industrial production and commercialization of SAAs.

3. Unique electronic properties of SAAs

Unlike SACs and conventional bulk metal catalysts, the catalytic properties of the active sites in SAA catalysts are essentially controlled by the interaction of isolated single atoms with the host metal (i.e., alloy bonding). Such interactions form new atomic and electronic structures, which in turn determine their intrinsic catalytic properties [71, 135]. In this section, we first investigate the electronic interactions between guest and host metals in SAAs from a theoretical perspective. Then, combined with practical cases, we delve into the impacts of free-atom-like *d*-state, charge transfer and energy band structure in SAAs on catalytic performance, aiming to systematically clarify their structure-performance relationships.

3.1 Unique free-atom-like *d*-state in SAAs

In most SAAs, the density of active sites is intentionally maintained at a low level. This design ensures atomically dispersed binding sites while reducing the risk of surface aggregation to a minimum. As a result of this low density, the highly diluted solute atoms (i.e., the active sites) interact electronically with the host mental atoms, such as through electron transfer and changes in the width and position of energy bands [68]. These changes can modulate the catalytic activity and product selectivity of the catalyst. Theoretical studies on SAA catalysts using high-throughput density functional theory (DFT) calculations and data-driven approaches based on the Materials Project are significant for developing new SAA catalysts and understanding the mechanisms behind catalytic performance changes [136].

For example, Greiner et al. revealed that, due to minimal energetic and spatial overlap between the solute and matrix atoms, solutes at extremely dilute concentrations (i.e., in the absence of solute-solute bonding) exhibited a weak interaction with the electronic states of the matrix element [75]. This endowed the solute atoms with free-atom-like *d*-state, in which the *d*-electron orbitals were nearly degenerate and extremely narrow. This unusual electronic structure altered the solute element's adsorption properties such that the bonding with adsorbates resembled the bonding in molecular metal complexes. Thus, the adsorption strength of adsorbates can be well tuned, and the selectivity of target products can be remarkably enhanced. For example, the Cu 3*d* states (0.5 eV) in AgCu SAA (0.3 at% Cu) were five times narrower than those of bulk Cu (2.5 eV) (Figure 7a). The narrowness of the Cu 3*d* state gave rise to a strong coupling to the adsorbates, and could lead to the formation of new covalent bonds. Furthermore, the Cu centers in AgCu alloy exhibited a localized negative charge. This resulted in stronger bonding between the alloy and adsorbates with higher electronegativity than Cu, compared to elemental Cu. Specifically, in the case of O bound to Cu_{36}, the O $2p_z$ state split into bonding (σ) and antibonding orbitals (σ*). In contrast, the O $2p_x$ and $2p_y$ states that lay parallel to the surface and had limited spatial overlap with the Cu *d* states remained unsplit, which resulted in broadened non-bonding states (Figure 7b). In $Ag_{35}Cu_1$ SAA, the narrow *d*-band strongly coupled with the 2*p* orbitals of O, splitting them into σ and σ* bonds as well as additional π and π* bonds (Figure 7c). The formation of the π bond for O adsorbed on AgCu alloy increased the bond strength by 0.3 eV stronger than on

elemental Cu. Such free-atom-like *d*-state was also extended to AgNi, AgPd, AgMn, and AgCr SAAs.

In another example, Spivey et al. revealed the selective interactions between free-atom-like *d*- states in SAA catalysts and near-frontier molecular orbitals (MOs) (Figure 7d) [137]. For example, crotonaldehyde could be hydrogenated via the aldehyde group (HOMO) in the ald-mode (aldehyde adsorption) to produce unsaturated alcohols and via the alkene group (HOMO-1) in the ene-mode (alkene adsorption) to produce saturated aldehydes. For monometallic Fe, the high energy center and breadth of *d*-states of Fe led to hybridization with both aldehyde group and alkene group, resulting in poor unsaturated alcohols selectivity. In contrast, the HOMO of crotonaldehyde aligned more closely with the sharp *d*-states of single Fe sites in Fe/Au SAA, leading to more effective hybridization to format unsaturated alcohols through the hydrogenation of aldehyde groups (Figure 7e, f). For Pt/Au SAA, despite their narrower Pt *d*-states, the *d*-band position was positioned between the HOMO and HOMO-1. Compared to monometallic Pt with broad *d*-states, Pt/Au SAA exhibited a comparable degree of hybridization with both the HOMO and HOMO-1, with spatial overlap effects dominated. However, high filling of Pt *d*-states promoted population of antibonding levels and rendered Pauli repulsion dominant, which disfavored hybridization with the HOMO in the ald-mode. Consequently, more precise matching with the HOMO-1 in the ene-mode reduced non-specific interactions, thereby promoting the production of saturated aldehydes (Figure 7d-f).

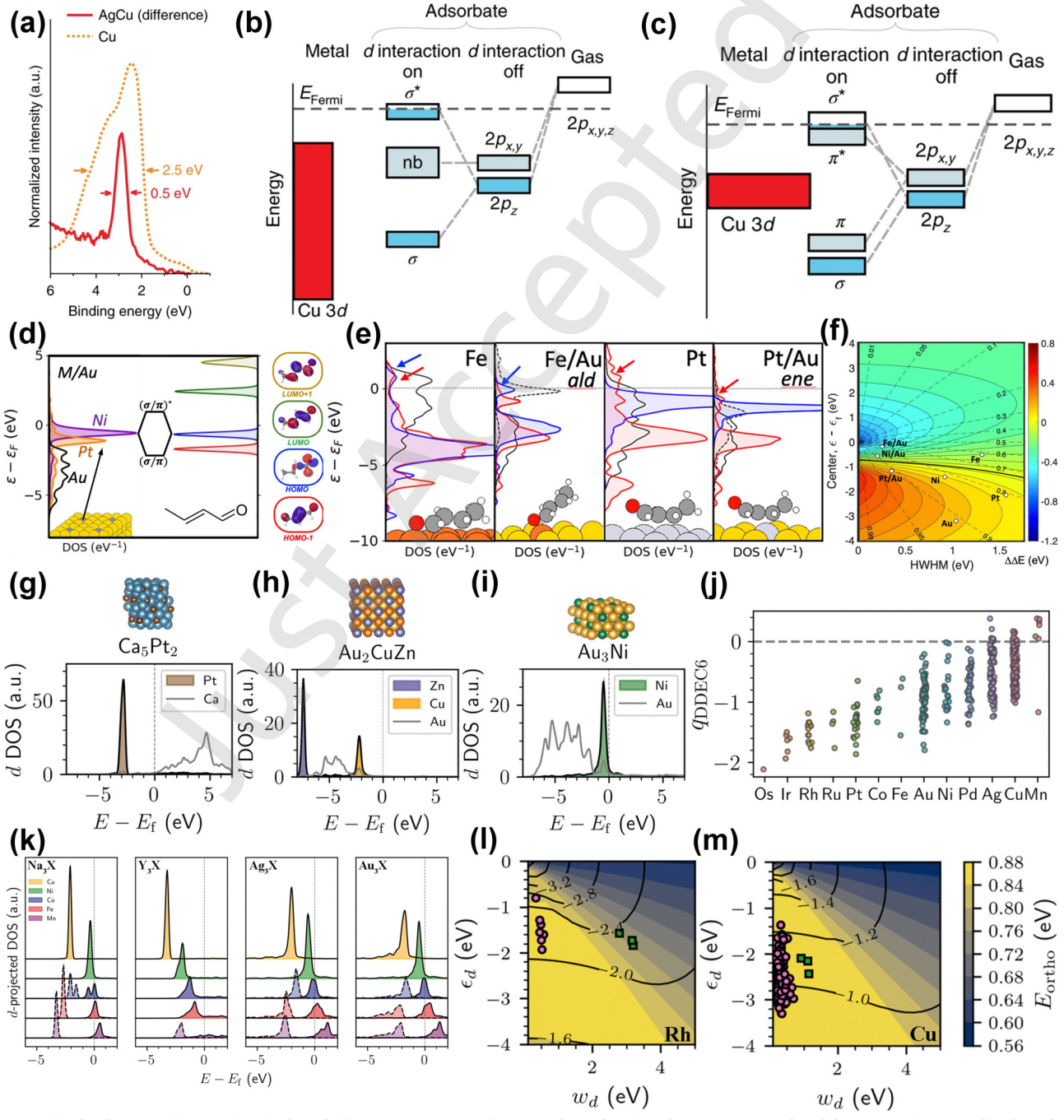

Figure 7. (a) The density of states (DOS) plots difference spectrum of AgCu and Ag. (b), (c) Schematic energy-level diagrams of O 2 *p* orbitals and Cu 3*d* hybridization for O adsorption on Cu (b) and AgCu (c) surfaces, non-bonding (nb). Reproduced with permission from Ref. [75] Copyright 2018, Springer Nature. (d) Left: d-projected DOS for SAAs with an Au(111) host. Ni (purple), Pt (orange), and Au (black). Right: Frontier and adjacent

orbitals for crotonaldehyde. (e) Projected DOS for HOMO (blue) and HOMO-1 (red) of crotonaldehyde in its most stable adsorption geometry (insets) on monometallic Fe(111) and Pt(111) surfaces, as well as for crotonaldehyde MOs adsorbed at isolated guest atom sites of Fe/Au and Pt/Au SAAs. (f) Difference in *d*-band interaction between binding modes (ΔΔE = ΔE (ald) - ΔE (ene) (The difference in adsorption energy between the two modes)) vs band characteristics. Reproduced with permission from Ref. [137] Copyright 2021, American Chemical Society. (g)-(i) Structure and calculated d-projected DOS for bulk Ca_5Pt_2, bulk Au_2CuZn, and bulk Au_3Ni. Atom color code: Ca (turquoise), Pt (brown), Au (yellow), Ni (green), Cu (orange), Zn (light purple). (j) Distribution of DDEC6 partial atomic charges, qDDEC6, for the transition metals with localized *d*-states identified in the screening process. (k) *d*-Projected DOS for atom X (X = Mn, Fe, Co, Ni, Cu) in tetragonal Na_3X, orthorhombic Y_3X, hexagonal Ag_3X, and hexagonal Au_3X. (l), (m) E_{ortho} (colormap) and E_{hyb} (contour lines) with free variation of ε_d, w_d for Rh and Cu. Points represent semi-elliptical fits to *d*-projected DOS of metal binding sites on intermetallic surfaces (pink circles) and corresponding transition metals (green squares). Reproduced with permission from Ref. [136] Copyright 2023, The Royal Society of Chemistry.

Rosen et al. further found that site isolation was necessary for transition metals to exhibit *d*-states of free-atom-like, and that the median interatomic distance between transition metals with localized *d*-states was 4.6 Å [136]. In addition, elements with localized *d*-states were often surrounded by group 1-3 metals (e.g., the *d*-states of Pd, Pt, and Ag in Na_3Pd, Ca_5Pt_2, and Sr_7Ag_3, respectively) and also by late transition metals in many cases (e.g., the *d*-states of Cu and Ni in Ag_3Cu and Au_3Ni, respectively). Except for binary intermetallic, this phenomenon also extended to ternary intermetallic compounds where two different metal elements had localized *d*-states, such as Y_2CuAu, Au_2CuZn, and Pd_2CuSn with localized Cu/Au, Cu/Zn, and Cu/Sn *d*-states, respectively (Figure 7g-i). Additionally, the majority of localized *d*-state transition metals identified from the computational screening study exhibited partial anionic character due to charge transfer from neighboring metal species, which was consistent with the findings of Greiner et al. studies (Figure 7j). This could be attributed to the electronegativity difference between the two metal atoms as well as localized electronic states of the dilute component during alloy formation. Based on this criterion, appropriate metal materials can be selected by considering the electron affinity of different reactant intermediates. In addition, elements with higher group numbers were found to decrease the width of the *d*-band while shifting the *d*-band center (ε_d) to lower energies relative to the Fermi level (E_F). At the same time, the *d*-band width of 3*d* metals was narrower than that of 4*d* and 5*d* metals (Figure 7k). This provides guidance for the selection of catalyst metal materials. On the other hand, the effect of *d*-band center and *d*-band widths (w_d) of SAAs on gas molecule adsorption can be clearly described using the hybridization energy (E_{hyb}) from the electronic mixing between the adsorbate and the metal binding site, as well as the orthogonalization energy penalty (Pauli repulsion, E_{ortho}). For example, when Rh, Ir, Pd, and Pt with localized *d*-states served as metal binding sites in intermetallic compounds, their *d*-band - narrower than those in their elemental forms — could increase the orthogonality energy penalty. This offset the stabilizing effect of hybridization energy, thereby weakening CO adsorption (Figure 7l). In contrast, since the w_d of Cu in intermetallic differed little from that in elemental Cu - unlike the other four elements - the main factor governing differences in CO adsorption energies between them was hybridization energy, mediated by changes in the ε_d position (Figure 7m). In summary, SAAs feature low-density, dispersed active sites, with guest-host electronic interactions (charge transfer, *d*-band modulation) governing catalysis. Theories highlight dilute solutes' free-atom-like narrow *d*-states, selective orbital interactions, and site isolation's role, guiding metal selection for targeted performance.

3.2 Charge transfer

The electron density of metal sites is one of the key parameters to determine the adsorption, activation, and desorption of reactant molecules, intermediates and product molecules on the surface of the catalyst [138-140]. In SAA catalysts, charge polarization may be affected by electronic perturbations between guest metal and the host metal [108]. The charge polarization redistributes the local electron density in the SAAs and affects the electron transfer pathways during catalysis, thus modulating the catalytic activity.

Electron transfer in alloys typically occurs between two metals with a significant electronegativity difference, where electrons transfer from the metal with lower electronegativity to that with higher electronegativity [141, 142]. Such electron transfer leads to an elevated d-orbital electron filling degree in the electron-accepting metal, thereby inducing a downward shift of its ε_d and ultimately regulating the catalyst's adsorption behavior toward reaction intermediates [143]. To verify this mechanism in simple single-atom alloy SAA systems, Chen et al. fabricated a Bi_1Pd SAA via a one-pot wet chemistry route for electrochemical nitrate reduction to ammonia (NO_3RR) [144]. Due to the electronegativity difference between Bi (1.9) and Pd (2.20), DFT calculations confirmed electron transfer (0.12 e) from Bi_1 to its adjacent Pd atoms (Pd1), which directly decreased the ε_d of Pd from -1.48 eV to -1.50 eV ~ -1.55 eV. This reduced the binding strength of *NO at the hollow site surrounded by two Bi_1-adjacent Pd1 atoms and one more distant Pd atom (Pd2) (Figure 8a). Meanwhile, the electron transfer from catalysts to NO_3^- increased from 0.58 *e* on pure Pd to 0.65 *e* on Bi_1Pd SAA, leading to enhanced electron accumulation on the antibonding orbital of $*NO_3^-$ and promoting the activation of NO_3^- (Figure 8b). Thus, the Bi_1Pd exhibited a significantly lower energy barrier for the potential-determining step (PDS) of *NO → *NOH (0.40 eV) than pure Pd (0.63 eV), benefiting the NO_3RR (Figure 8c, d). Another simple SAA system further validated the correlation between electron transfer-induced charge state changes and adsorption regulation. Liu et al. constructed Pd NPs and Pd_1Ni SAA models via DFT calculations to investigate acetylene semi-hydrogenation [145]. Since Ni (1.91) is less electronegative than Pd (2.20), electron transfer from Ni to Pd rendered the Pd single atom negatively charged (-0.33 e), in contrast to the electrically neutral Pd atoms on Pd NPs (Figure 8e). This charge state change weakened ethylene adsorption. Specifically, ethylene adsorbed on Pd NPs' hollow sites with an adsorption energy of -1.46 eV, while on Pd_1Ni SAA, it preferred the PdNi interface or Pd single atom with lower adsorption energies (-1.15 eV and -1.14 eV, respectively) (Figure 8f). This

improvement in adsorption behavior enhanced the selectivity to ethylene.

Beyond simple metal-metal electron transfer, dual charge modulation, including metal-metal and metal-support in complex SAA systems, can further optimize catalytic performance. Ren et al. prepared a core-shell $NiPt_{SA}$@NC SAA catalyst to investigate the effect of dual charge modulation of Pt single atoms (Pt_{SA}) within the metal core and core-shell interface on the catalytic performance of hydrogen oxidation reaction [146]. Pt L_3-edge XANES of $NiPt_{SA}$@NC displays a slight decrease in the white line intensity compared to Pt foil, indicating the electron transfer from Ni to Pt. DFT calculations further revealed that introducing Pt atoms triggered charge polarization, which created an electron-rich environment around Pt atoms and electron depletion in adjacent Ni atoms, coupled with electron transfer from the metallic core to the carbon shell (0.77 *e*) (Figure 8g, h). This dual-electron regulation mechanism downshifted the ε_d from -1.31 eV of Ni to -1.44 eV of $NiPt_{SA}$@NC, and induced hydrogen atoms to adopt a bridge adsorption configuration on $NiPt_{SA}$@NC (Figure 8i). As a result, the free energy of H adsorption on the active center decreased from -0.2 eV on Ni to -0.1 eV on $NiPt_{SA}$@NC, adjacent to the most optimized H adsorption and thus accelerating the hydrogen oxidation reaction (Figure 8j).

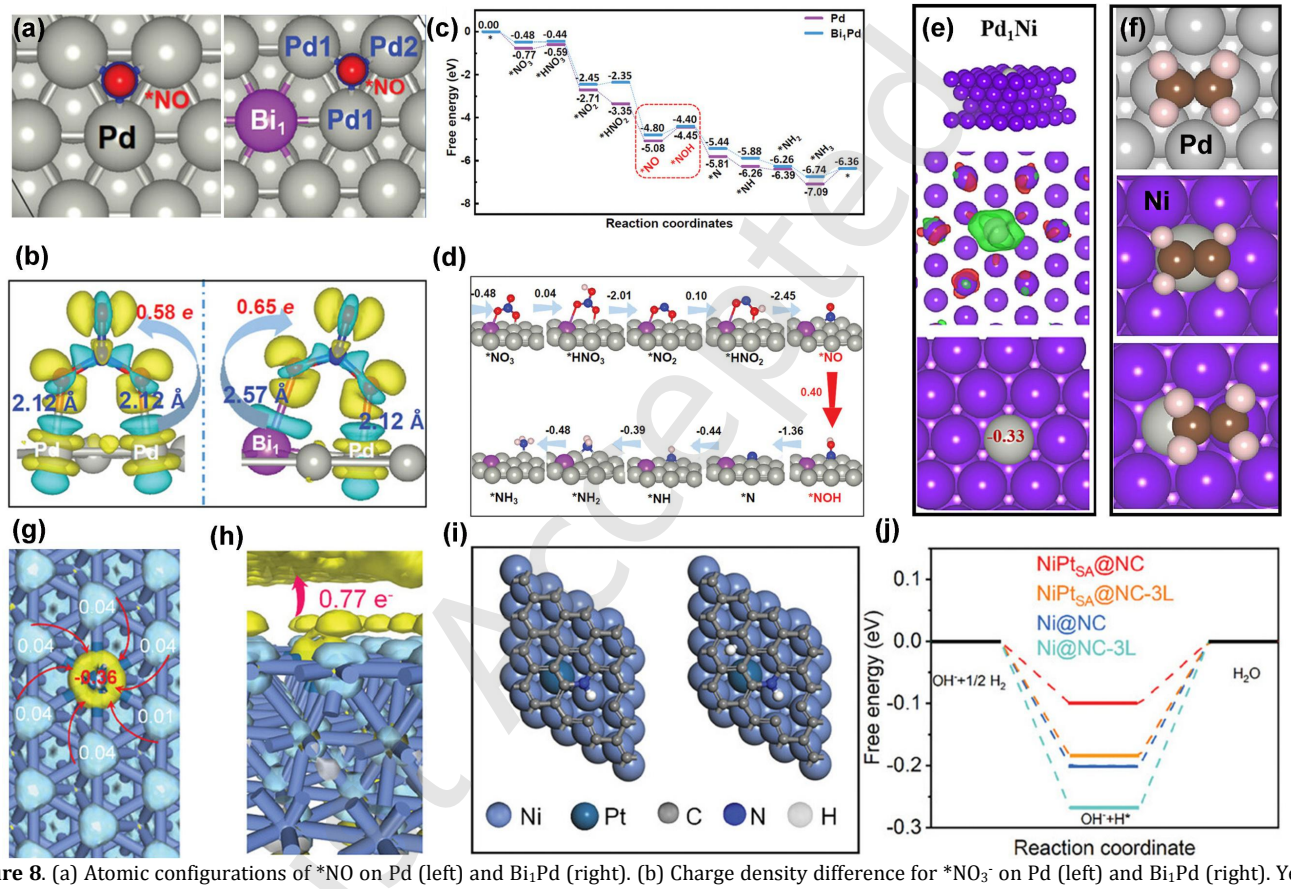

Figure 8. (a) Atomic configurations of *NO on Pd (left) and Bi_1Pd (right). (b) Charge density difference for $*NO_3^-$ on Pd (left) and Bi_1Pd (right). Yellow and cyan denote charge accumulation and depletion regions, respectively. (c) Free energy diagram of energy-preferred NO_3RR pathways on Pd and Bi_1Pd, and corresponding (d) local structures of the reaction intermediates on Bi_1Pd; Reproduced with permission from Ref. [144] Copyright 2024, Wiley-VCH. (e) Diagrams of charge transfer between Pd and Ni atoms over Pd_1Ni SAA by DFT: the red area represents the loss of electrons, while the green area represents the gain of electrons. (f) Top view of the DFT-optimized $*C_2H_2$ adsorption configuration of the reaction intermediates and substrates on the surfaces of Pd (1 1 1) and Pd_1Ni; Reproduced with permission from Ref. [145] Copyright 2024, Elsevier. (g) The top view and (h) the side view of the charge density difference in the interface of $NiPt_{SA}$@NC. (i) Top view of $NiPt_{SA}$@NC and the adsorption configurations of H* intermediate on $NiPt_{SA}$@NC surfaces. (j) Free energy diagram for $NiPt_{SA}$@NC and Ni@NC toward the alkaline hydrogen oxidation reaction; Reproduced with permission from Ref. [146] Copyright 2024, Wiley-VCH.

3.3 Energy band structure

In general, transition metals can provide unpaired d-electrons or empty d-orbitals in catalytic reactions to form adsorbed species with the reactant molecules [147]. Such orbital interplay between the adsorbed compounds and active sites splits the energy levels and forms new energy bands [138]. To simplify the processing, a ε_d (i.e., an average energy of d-electron states) theory that was proposed by Nørskov and co-workers has been widely used to predict and explain the catalytic activity of transition metals [139]. In the case of SAA catalysts, the interaction of different doped metal single atoms with the base metal alters the DOS near the E_F, which further alters the availability and behavior of the ε_d. These electronic modulations modify the binding strength of the key intermediates, ultimately optimizing the catalytic performance.

For example, Wang et al. synthesized a Sb_1Cu SAA through a simple cation exchange strategy to explore the catalytic performance in nitrite reduction reaction (NO_2RR) [148]. DFT calculations revealed significant orbital hybridization between the Sb-5*p* orbital and the Cu-3*d* orbital, indicating a strong Sb_1-Cu electronic interaction (Figure 9a). Such electronic interaction induced a downward shift in the ε_d of Sb_1Cu (-2.57 eV) compared to Cu (-2.38 eV), which could

optimize the intermediate adsorption to promote the protonation energetics of Sb_1Cu (Figure 9b). Specifically, Sb_1Cu (-8.46 eV) exhibited a lowered highest occupied energy (E_p) position of *NO compared to that of Cu (-5.56 eV), while Cu (-4.90 eV) and Sb_1Cu (-5.01 eV) displayed quite similar E_p position of *NHO (Figure 9c, d). Such an alteration suggested that introducing Sb atoms onto Cu mitigated the adsorption strength of *NO while maintaining that of *NHO, thereby reducing the barrier of the rate-determining step (RDS) for *NO → *NHO (from 0.72 eV to 0.40 eV) and promoting the NO_2RR (Figure 9e). Another typical SAA catalyst for NO_2RR was reported by Wang et al., who synthesized a Ni_1Ru SAA catalyst by one-step hydrothermal method to investigate the catalytic properties of NO_2RR [74]. DFT calculations showed that the strong Ni-Ru electronic interactions induced by the hybridization of Ni/Ru orbitals up-shifted the ε_d of Ni_1Ru to -1.19 eV compared to that of pristine Ru (-1.26 eV) (Figure 9f, g). This enhances the orbital overlap between the catalyst and reaction intermediates, thereby selectively regulating the charge transfer efficiency between them. Specifically, the charge transfer numbers from catalyst to $*NH_2O$ were slightly increased from 0.53 |e| (Ru) to 0.56 |e| (Ni_1Ru), while the charge donation from the catalyst to $*NH_2OH$ was significantly boosted from 0.12 |e| (Ru) to 0.23 |e| (Ni_1Ru). This ε_d -mediated selective charge transfer endowed Ni_1Ru with an optimal binding balance between $*NH_2O$ and $*NH_2OH$ intermediates. Consequently, the energy barrier of the RDS ($*NH_2O \rightarrow *NH_2OH$) decreased from 0.79 eV on Ru to 0.44 eV for Ni_1Ru, thus enhancing the rate of NO_2RR (Figure 9h).

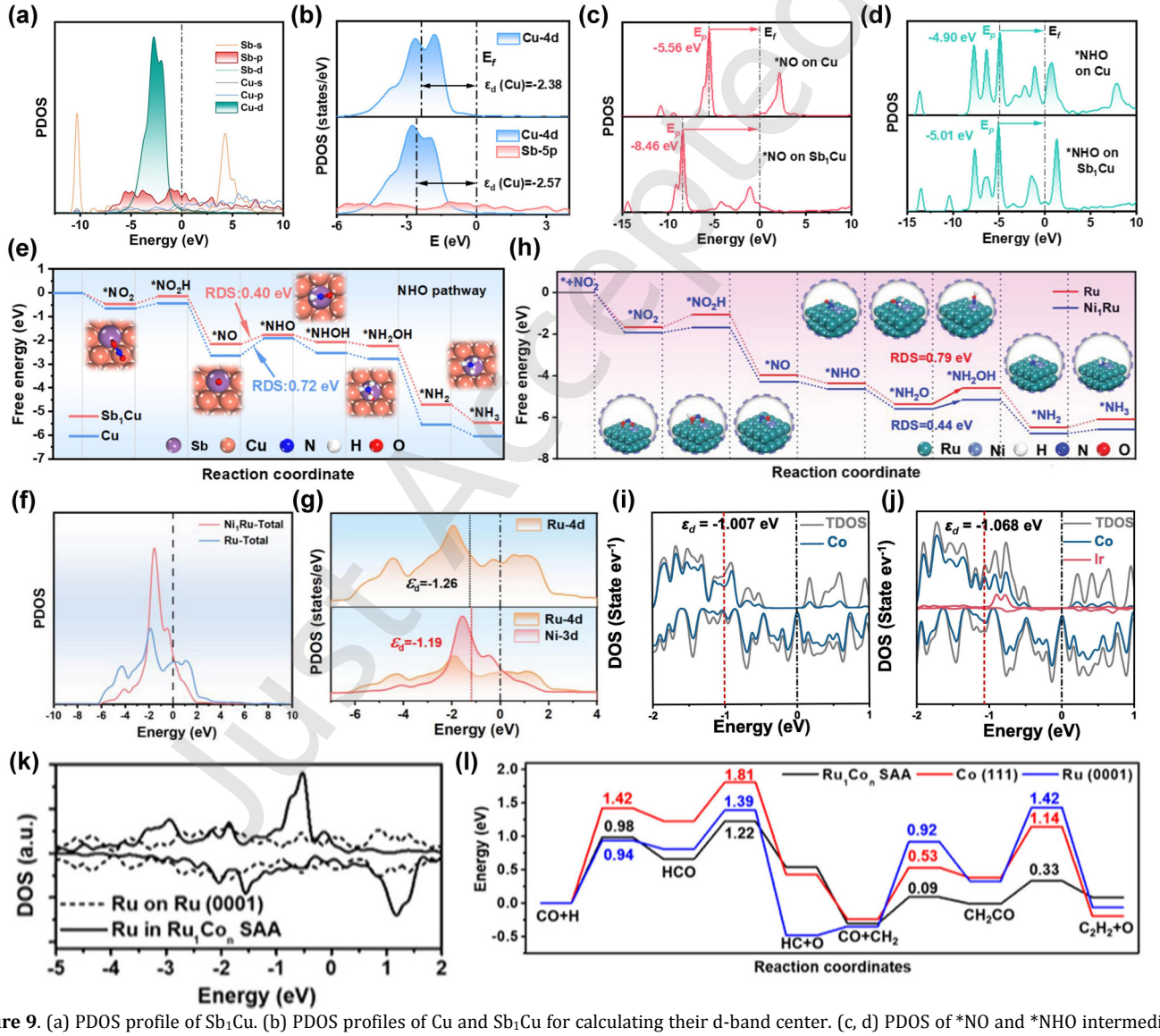

Figure 9. (a) PDOS profile of Sb_1Cu. (b) PDOS profiles of Cu and Sb_1Cu for calculating their d-band center. (c, d) PDOS of *NO and *NHO intermediates on Cu and Sb_1Cu. (e) Free energy diagrams of NO_2RR pathways on Cu and Sb_1Cu; Reproduced with permission from Ref. [148] Copyright 2024, American Chemical Society. (f) PDOS analyses of Ru and Ni_1Ru. (g) PDOS profiles of Ru and Ni_1Ru for calculating their *d*-band center. (h) Free energy diagrams of the energetically favorable NHO pathway on Ru and Ni_1Ru; Reproduced with permission from Ref. [74] Copyright 2023, Wiley-VCH. (i-j) DOS of Ir/Co *d* orbitals for Co-N-C and IrCo-N-C. Short dotted lines black indicate the E_F, dashed red lines indicate the ε_d; Reproduced with permission from Ref. [149] Copyright 2023, Elsevier. (k) PDOS on *d* orbitals of the surface Ru atom on Ru(0001) (dashed line) and in Ru_1Co SAA (solid line) (l) Energy profiles of CO conversion to C_1 and C_2 products on Ru_1Co_n SAA, Co(111) and Ru(0001); Reproduced with permission from Ref. [80] Copyright 2021, Elsevier.

Beyond NO_2RR, the ε_d modulation mechanism of SAA catalysts also works effectively for the hydrogen evolution

reaction. Zhang et al. prepared IrCo SAA catalyst with an Ir loading of 2.17 wt.% by encapsulating IrCo in NCNTs (denoted as IrCo@NCNTs) [149]. Based on DFT calculations, the ε_d decreased form -1.007 eV in Co@NCNTs to -1.068 eV in IrCo@NCNTs after the decoration of single Ir atom (Figure 9i, j). Such downshift of ε_d weakened the adsorption energy between H* and IrCo@NCNTs from -0.46 eV for Co@NCNTs to 0.2 eV for IrCo@NCNTs, thus promoting the desorption of H* from IrCo@NCNTs and accelerating the hydrogen evolution reaction process. Notably, this electronic modulation strategy of SAAs is not limited to electrocatalysis but also extends to thermal-catalysis, as exemplified by Fischer-Tropsch synthesis (FTS). Meng et al. designed a Ru_1Co_n SAA to explore its catalytic performance in FTS via a two-dimensional confinement strategy. [80] At a reaction temperature of 200 °C, the C_{5+} selectivity was significantly enhanced from 69.2% (Ru/Co NPs) and 60.8% (Co NPs) to 86.3% (Ru_1Co_n SAA) after the introduction of isolated Ru atoms into the Co NP matrix. DFT calculations revealed that the Ru atoms in Ru_1Co_n SAA exhibited a much higher and more localized electron density near the E_F compared to Ru (0001) (Figure 9k). This enhanced the interaction between Ru and reactants, thereby reducing the transition-state energy for chain growth from 1.14 eV on Co (111) and 1.42 eV on Ru (0001) to 0.33 eV on Ru_1Co_n SAA. Consequently, the formation of long carbon chains on Ru_1Co_n SAA was facilitated a low temperature (Figure 9l).

Following the guideline that the unique free-atom-like *d*-states of SAAs can significantly affect reaction selectivity, and that charge transfer and orbital hybridization can regulate the ε_d, we have further extracted general design principles for target reactions. Taking NO_2RR as an example, we summarize the strategies for screening suitable host-guest metal combinations: (1) matching the localized *d*-states with the molecular orbitals of NO_2^- and reaction intermediates to improve product selectivity; (2) tuning the direction of charge transfer between host and guest metals based on differences in electronegativity to optimize the ε_d and intermediate adsorption, thus promoting the NO_2RR process. (3) regulating the *d*-band width and ε_d via orbital hybridization between host and guest metals to optimize the adsorption-desorption balance of key intermediates (*NO, *NHO, *NH_2O, *NH_2OH etc.) and lower the energy barrier of the rate-determining step. (4) enhancing the localized electron density near the Fermi level of guest metal sites to strengthen orbital overlap with reactants and selectively stabilize critical transition states.

4. Electrocatalytic applications

SAAs have become a research frontier in the field of electrocatalysis due to its unique electronic structure and efficient catalytic performance. By uniformly dispersing individual metal atoms on a metal carrier, SAAs can significantly enhance the activity and selectivity in a series of electrocatalytic reactions. In this section, some representative electrocatalytic reactions are summarized to illustrate the unique structure-performance relationship of SAAs.

4.1 Hydrogen Evolution Reaction (HER)

HER is a key component in the electrolysis of water and is mainly responsible for the decomposition of water into hydrogen. It is a process that is of great importance in the storage and conversion of renewable energy sources, especially in the fields of hydrogen energy production, renewable energy storage and electrochemical synthesis [150-152]. The reaction mechanism of HER may vary from electrode to electrode material, but it can be divided into the following two steps. Water molecules first adsorb and accept electrons on the cathode surface to generate adsorbed hydrogen atoms (H*) via the reaction $H_2O + e^- \rightarrow H^* + OH^-$, which is known as the Volmer step. After this step, the generated H* can be converted to hydrogen by two pathways: (1) the Tafel pathway: two hydrogen atoms in the adsorbed state combine to form a hydrogen molecule ($2H^* \rightarrow H_2$); (2) the Heyrovsky pathway: a hydrogen atom in the adsorbed state reacts with a water molecule, releasing a molecule of hydrogen, while generating an OH^- ($H^* + H_2O + e^- \rightarrow H_2 + OH^-$). To date, catalysts containing Pt group elements have been widely used in HER because of their high ability to adsorb H atoms.

For example, Gao et al prepared an alloyed Pt single atoms on Ru substrate (denoted as alloyed Pt SA) via a high-temperature plasma strategy [153]. This strategy entailed the generation of a large number of defects on the Ru surface by plasma, which subsequently served as anchor sites for Pt atoms. These Pt atoms were then alloyed in a high-temperature environment, resulting in the formation of a SAA structure. Impressively, the alloyed Pt SA exhibited an overpotential of as low as 23 mV at a current density of 10 mA cm^{-2} in 0.5 M H_2SO_4 solution, surpassing Pt/C-JM (commercial Pt/C with a 40 wt.% Pt) (28 mV) and Pt-VN (Pt single atoms fabricated on N-terminated vanadium nitride) (82 mV) (Figure 10a). Moreover, the alloyed Pt SA exhibited a higher mass activity (MA) of 18.84 A mg_{Pt}^{-1} at the overpotential of 50 mV than Pt/C-JM of 0.812 A mg_{Pt}^{-1} and Pt-VN of 0.82 A mg_{Pt}^{-1} (Figure 10b). More importantly, the alloyed Pt SA catalyst can be stably operated at 1 A cm^{-2} for over 1000 h with a voltage-degradation rate of only 0.061 mV h^{-1} in a proton exchange membrane water electrolyzer, significantly outperforming VN-supported Pt SACs, which have a voltage degradation rate of 18.04 mV h^{-1} under the identical working conditions. DFT calculations revealed that the integrated crystal orbital bond index (ICOBI) of the Pt-Ru bond was 0.65118, which is higher than the ICOBI values of the Pt-N bonds in Pt-VN (0.40109) and Pt supported on N-doped graphene (0.38909). This result indicates that the Pt-Ru bond has a stronger covalent interaction compared to the Pt-N bonds in the aforementioned systems. Such a strong covalent interaction can effectively stabilize the Pt single atoms, thereby enhancing the durability of the alloyed Pt SA catalyst during the HER process. The doping of non-metallic N atoms could further enhance the HER performance of SAA catalysts. Luo et al. prepared a (Ru-N)@Pt SAA catalyst via thermal annealing, where N and Pt co-doped Ru NPs were supported on multi-walled carbon nanotubes [154]. In an 1.0 M KOH electrolyte, the (Ru-N)@Pt achieved a current density of 10 mA cm^{-2} at an overpotential of only 15 mV, which was significantly lower than those of Pt/C (35 mV), Ru@Pt (41 mV), and Ru/C (64 mV) (Figure 10c). The Tafel slope of (Ru-N)@Pt that is 25 mV dec^{-1} was notably lower than those of Ru/C (66 mV dec^{-1}) and Pt/C (53 mV dec^{-1}),

indicating that the Tafel step served as the RDS for (Ru-N)@Pt and that the incorporation of N and Pt substantially enhanced the kinetics of water dissociation. DFT calculation revealed that doping N induced a downshift of the Ru d_z^2orbital and made the Ru d_z^2 orbital symmetry more suitable to the *p* orbital of H_2O. This not only decreased the adsorption energy of H_2O from -0.42 eV on Ru@Pt and -0.45 eV on Ru to -0.69 eV on (Ru-N)@Pt, but also decreased the dissociation energy of H_2O from 1.08 eV on Ru@Pt and 1.31 eV on Ru to 0.87 eV on (Ru-N)@Pt, thus accelerating the water adsorption and dissociation kinetics during HER (Figure 10d). Furthermore, the introduction of Pt decreased the ε_d from -1.93 eV for Ru-N and -2.01 eV for Ru to -2.81 eV for (Ru-N)@Pt (Figure 10e). This optimized the Gibbs free energy of H* adsorption (ΔG_{H^*}) from -0.37 for Ru-N and -0.38 eV for Ru to -0.12 eV for (Ru-N)@Pt, thus promoting the desorption of H_2.

Considering the scarcity of precious metals, replacing precious metal substrates with non-precious metal substrates can reduce the preparation cost of SAAs. For example, Yuan et al. successfully incorporated Pt single atoms in Mo foil to fabricate Pt-$SA_{0.056}$/Mo-L SAA catalyst via laser ablation strategy [155]. In 0.5 M H_2SO_4 electrolyte, the Pt-$SA_{0.056}$/Mo-L exhibited an overpotential of 31 mV at a current density of 10 mA cm^{-2}, which was lower than that of Pt-$NP_{0.473}$/Mo-L (36 mV) and 20 wt.% Pt/C (32 mV) (Figure 10f). Moreover, the MA of Pt-$SA_{0.056}$/Mo-L was about three times higher than that of the commercial 20 wt.% Pt/C catalyst (Figure 10g). XPS characterization revealed that the binding energy peaks of Pt^0 in Pt-$SA_{0.056}$/Mo-L exhibited a slight negative shift relative to Pt foil, whereas that of Mo^0 showed a positive shift compared with Mo-L. These results confirm the occurrence of electron transfer from Mo to Pt. DFT calculations further revealed that electronic interactions between Pt single atoms and the Mo substrate rendered Pt-$SA_{0.056}$/Mo-L a ΔG_{H^*} of -0.07 eV, which was much closer to zero than that of Pt NPs (-0.14 eV), thereby facilitating the desorption of H_2 during HER (Figure 10h). In addition, the adsorption energy (E_{ads}) of single Pt atom on metallic molybdenum was -2.53 eV, which was much larger than that on molybdenum oxide (-0.69 eV), indicative of the excellent structural stability between Pt single atoms and metallic molybdenum. Such structural stability allowed Pt-$SA_{0.056}$/Mo-L to be operated stably at a high current density of 850 mA cm^{-2} for 50 h. Wang et al. also prepared a MoO_2-supported Ir_1Ni SAA (denoted as $Ir_1Ni@MoO_2$) via a GR method, where Ir atoms substituted for some Ni atoms in the lattice [109]. In 1 M KOH electrolyte, the $Ir_1Ni@MoO_2$ delivered an overpotential of 48.6 mV at a current density of 10 mA cm^{-2}, which was lower than that of Pt/C (59 mV). In addition, at a voltage of -0.07 V vs. RHE, the $Ir_1Ni@MoO_2$ showed a MA of 1.82 mA μg_{Ir}^{-1}, which was 14 times higher than that of Pt/C catalysts. At -0.07 V vs. RHE, the $Ir_1Ni@MoO_2$ exhibited the highest turnover frequency (TOF) of 1.77 s^{-1} compared to 0.20 s^{-1} on IrNi/MoO_2 (Ir for NPs) and 0.13 s^{-1} on Pt/C, respectively. DFT calculations revealed that the Ir $5d_z^2$ orbital was broader than the Ni $3d_z^2$ orbital, which benefitted the bonding interaction between the H 1*s* orbital and Ir $5d_z^2$ orbital, strengthening the binding of H to the Ir atop site. Thus, at a higher H coverage (greater than 1 monolayer), H could adsorb on the Ir atop site with a binding energy of approximately 0 eV in the Ir-Ni (111), which was stronger than the weak adsorption on the Ni atop site (+0.4 eV) of Ni(111). The favorable binding for H* on Ir-Ni (111) reduced the energy barrier of Volmer step on the H saturated surface, thus promoting the HER.

In another example, Tong et al. prepared a 3D N-doped carbon encapsulated RuCo SAA core-shell catalyst (denoted as Ru SA-Co-N-C) via stepwise templating induced-annealing method, where the Ru single atoms were atomically dispersed within Co NPs as the core [156]. This SAA modification strategy endowed the catalyst with good HER performance. Specifically, the Ru SA-Co-N-C delivered an overpotential of 43 mV at a current density of 10 mA cm^{-2} in 0.1 M KOH solution, which was lower than that of Pt/C (83 mV) (Figure 10i). Furthermore, Ru SA-Co-N-C showed a far smaller Tafel slope of 98 mV dec^{-1} than that of Co-N-C (136 mV dec^{-1}), indicating that the HER mechanism of Ru SA-Co-N-C followed the Volmer-Heyrovsky pathway, with H* desorption as the RDS. DFT calculations revealed that the cooperation among Ru single atoms, Co NPs, and N-doped carbon sheath could effectively optimize the bonding interaction of Ru SA-Co-N-C toward atomic hydrogen. Substituting a surface Co atom with a single Ru atom reduced the ΔG_{H^*} from 0.15 eV on Co-N-C to 0.02 eV for Ru SA-Co-N-C, thereby achieving the extremely desirable thermoneutral HER (Figure 10j). Such enhanced interaction could be further confirmed by electronic structure analysis. The C-H σ-bonding state on Ru SA-Co-N-C lay about 0.15 eV lower in energy than that on Co-N-C, coupled with a slightly shorter C-H bond length (1.13 Å) on Ru SA-Co-N-C than that on Co-N-C (1.15 Å). Doping non-precious metal single atoms on precious metal substrates had also been investigated for HER. For instance, Yang et al. prepared a Co-doped Pd-based nanosheet SAA catalyst (denoted as Co/Pdm-4, where 4 indicates the molar percentage of Co) via a one-pot synthetic method [157]. In 0.5 M H_2SO_4 solution, the Co/Pdm-4 exhibited an overpotential of 24.7 mV at a current density of 10 mA cm^{-2}, which was superior to that of commercial Pt/C and Pd/C (Figure 10k). Moreover, the Tafel slope of Co/Pdm-4 was 8.2 mV/dec^{-1}, which was much lower than that of Pd/C (24.5 mV/dec^{-1}) and Pt/C (28.6 mV/dec^{-1}). High-resolution XPS spectra of Pd 3*d* for Co/Pdm-4 revealed that peaks corresponding to Pd^0 and Pd^{2+} were shifted toward higher binding energy, which was attributed to electron transfer from Pd to Co in the alloy. DFT calculations further verified that such electron transfer downshifted the ε_d of Pd from -1.67 eV to -1.69 eV (Figure 10l). Thus, the ΔG_{H^*} decreased from -0.47 eV on Pdm to -0.35 eV on Co/Pdm-4, thereby promoting the desorption of H_2 during HER. Furthermore, the doping of Co atoms also decreased the ΔG between the initial state and the transition state for H_2O dissociation process from 0.87 on Pdm to 0.63 eV on Co/Pdm-4. This facilitated H_2O dissociation and the production of additional H* intermediates, promoting the HER.

In summary, the ΔG_{H^*} serves as the dominant thermodynamic descriptor for the HER activity of SAA catalysts, and optimal performance is typically achieved when ΔG_{H^*} approaches the thermoneutral value. As systematically demonstrated in this section, the adsorption

strength of H* is predominantly governed by the ε_d position of the active sites, which can be rationally tuned via the electronic metal-metal interactions within the SAA structure. Among the various metal combinations investigated, the combination of a noble-metal host and noble-metal single-atom guest, as exemplified by the (Ru-N)@Pt catalyst, delivers exceptional HER activity with an ultralow overpotential of only 15 mV at a current density of 10 mA cm^{-2}. This superior performance arises from the favorable electronic modulation: the bimetallic coupling and nonmetal doping cooperatively downshift the ε_d, optimize the H* adsorption energy, and accelerate water dissociation kinetics. We can take this as a reference to sequentially conduct further research on the combinations of noble metals (as hosts) and noble metals (as single-atom guests), thereby achieving the optimal HER performance.

4.2 Oxygen Evolution Reaction (OER)

OER is an electrochemical reaction that occurs at the anode during the electrolysis of water. It is a key electrochemical process in a wide range of energy conversion and storage technologies, particularly in water decomposition and renewable energy technologies [158, 159]. The widely accepted adsorption evolution mechanism (AEM) describes OER as the transformation of OH^- to O_2 under alkaline conditions and H_2O to O_2 under acidic conditions [160, 161]. Specifically, in acid conditions : (1) $H_2O + * \rightarrow *OH + H^+ + e^-$, (2) $*OH \rightarrow *O + H^+ + e^-$, (3) $H_2O + *O \rightarrow *OOH + H^+ + e^-$, (4) $*OOH \rightarrow O_2 + H^+ + e^-$; and in alkaline conditions : (1) $* + OH^- \rightarrow *OH + e^-$; (2) $*OH + OH^- \rightarrow *O + H_2O + e^-$; (3) $*O + OH^- \rightarrow *OOH + e^-$; (4) $*OOH + OH^- \rightarrow * + O_2 + H_2O + e^-$ (* denotes a site on the catalyst surface) [162, 163]. Benefitting from the synergy between metal single atoms and metal substrate, the SAA catalysts can enhance OER catalytic performance by increasing active site density or by optimizing oxygen-containing intermediates adsorption energy, thus gaining the interests from the researchers [160, 164, 165].

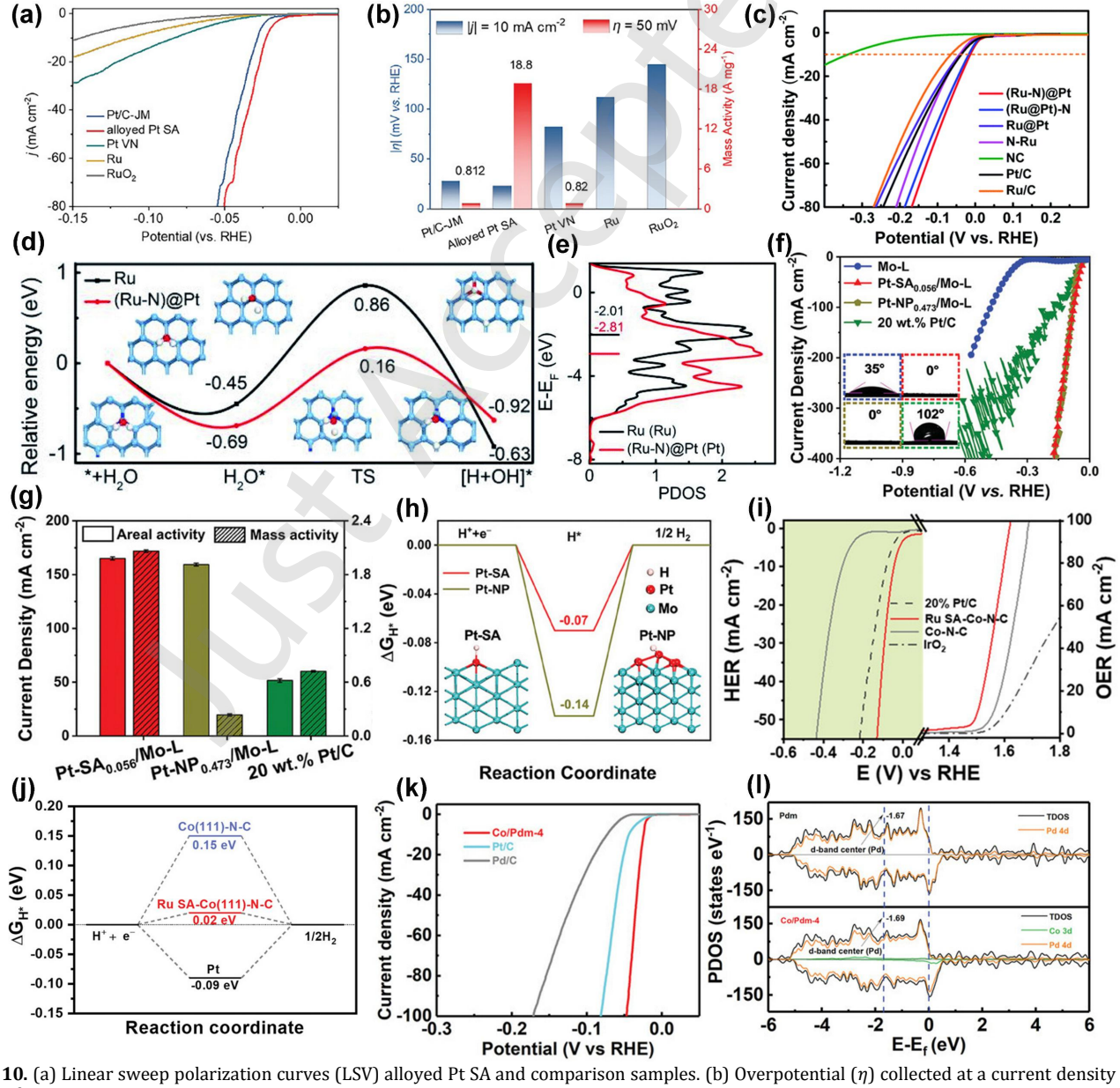

Figure 10. (a) Linear sweep polarization curves (LSV) alloyed Pt SA and comparison samples. (b) Overpotential (η) collected at a current density (j)of 10mAcm^{-2} and mass activity at η = 50 mV (vs RHE) for alloyed Pt SA and comparison samples; Reproduced with permission from Ref. [153] Copyright 2023, Wiley-VCH. (c) The LSV of (Ru-N)@Pt and comparison samples. (d) the relative energy diagram in the water adsorption and dissociation processes with relative structural information on Ru and (Ru-N)@Pt surfaces.(e) The d band PDOS of active Ru sites on the Ru surface and active Pt

sites on the (Ru-N)@Pt surface for H adsorption and desorption; Reproduced with permission from Ref. [154] Copyright 2021, The Royal Society of Chemistry. (f) Polarization curves of Mo-L, Pt-$SA_{0.056}$/Mo-L, Pt-$NP_{0.473}$/Mo-L, and 20 wt.% Pt/C for HER. The insets were the surface contact angle of these electrodes. (g) Areal activity and Pt mass activity of Pt-$SA_{0.056}$/Mo-L, Pt-$NP_{0.473}$/Mo-L, and 20 wt.% Pt/C with an overpotential of 0.1 V. (h) Calculated free energy for H adsorption on Pt-SA/Mo and Pt-NP/Mo. Reproduced with permission from Ref. [155] Copyright 2023, Wiley-VCH. (i) LSV curves of HER (left) and OER (right) of Ru SA-Co-N-C and comparison samples. (j) Free energy diagram for hydrogen evolution on Ru SA-Co-N-C and comparison samples. Reproduced with permission from Ref. [156] Copyright 2022, Wiley-VCH. (k) HER polarization curves of Co/Pdm-4, commercial Pt/C, and Pd/C in 0.5 M H_2SO_4. (l) Calculated density of states of Pdm and Co/Pdm-4. Reproduced with permission from Ref. [157] Copyright 2023, Wiley-VCH.

For example, Chae et al. prepared a chiral plasmonic SAA catalyst (denoted as Ir SA/L-Au NF) via a straightforward electrodeposition process using L-cysteine as a chiral inducer, where Ir single atoms (Ir SA) were uniformly distributed in chiral Au nanoflowers (L-Au NF) supported on a titanium felt substrate [166]. In 0.5 M H_2SO_4 solution, the Ir SA/L-Au NF under light showed an overpotential of 272.6 mV at a current density of 10 mA cm^{-2}, lower than that of Ir SA/L-Au NF (313.8 mV) in the dark, Ir SA/DL-Au NF (340 mV, achiral reference sample), and even the commercial IrO_2 (311.3 mV) (Figure 11a). Moreover, at 1.575 V vs. RHE, the Ir SA/L-Au NF under light exhibited a specific activity (SA) of 60.2 mA cm^{-2} and TOF of 0.03 s^{-1}, which were superior to those of Ir SA/L-Au NF in the dark and Ir SA/DL-Au NF, respectively (Figure 11b). DFT calculations and *operando* X-ray spectroscopy further elucidated the enhanced mechanisms of electrocatalytic OER on Ir SA/L-Au NF. Specifically, the chirality-induced spin selectivity (CISS) effect of chiral L-Au NF caused a better match between the spin polarization of the Ir atoms and the spin polarization of the oxygen atoms in the oxygen-containing intermediate (Figure 11c). This spin alignment optimized the adsorption energy of oxygen-containing intermediates, thereby reducing the calculated OER overpotential from 0.66 V on Ir SA/DL-Au NF to 0.46 V on Ir SA/L-Au NF. Furthermore, under light irradiation, the chiral Au substrates could generate hot carriers via localized surface plasmon resonance and transferred these hot carriers to Ir atoms, further enhancing the CISS effect and thereby promoting the OER performance. Meanwhile, *operando* X-ray spectroscopy of Ir SA/L-Au NF revealed that the Ir-Au bond length decreased from 2.39 Å without light irradiation to 2.33 Å with light irradiation at 1.45 V vs. RHE. Such contraction of the Ir-Au bonds stabilizes the isolated Ir single atoms, preventing agglomeration and degradation, thereby preserving active sites.

SAAs that are constructed with non-precious metal substrates have also exhibited excellent electrocatalytic performance for the OER. For example, Tong et al. prepared a 3D N-doped carbon encapsulated RuCo SAA core-shell catalyst (denoted as Ru SA-Co-N-C) via a stepwise templating induced-annealing method, where the Ru atoms were atomically dispersed within Co NPs [156]. In 0.1 M KOH solution, the Ru SA-Co-N-C exhibited an overpotential of 270 mV at a current density of 10 mA cm^{-2}, lower than the values of 370 mV of commercial IrO_2 (Figure 10i). DFT calculations revealed that, for Co-N-C, the adsorption energies of oxygen-containing intermediates (denoted as ΔE_{OH*}, ΔE_{O*}, and ΔE_{OOH*}) were 0.66 eV, 2.63 eV, and 3.85 eV, respectively. Upon Ru atom doping, these values were reduced to 0.54 eV, 2.45 eV, and 3.72 eV respectively (Figure 11d). By optimizing the adsorption energy of oxygen-containing intermediates, the incorporation of Ru decreased the OER calculated overpotential from 0.42 V for Co-N-C to 0.36 V for Ru SA-Co-N-C, thereby promoting the electrocatalytic performance of OER. In another example, Lee et al. prepared a graphitic carbon encapsulated Ru single-atom $CoFe_2$ SAA catalyst with abundant surface oxygen (denoted as $Ru_{SA}CoFe_2$/G), via a two-step micelle-incorporated sol-gel method and carbothermal reduction [79]. Herein, the Ru single atoms were uniformly dispersed in the CoFe alloy matrix. In 1 M KOH electrolyte, $Ru_{SA}CoFe_2$/G showed an overpotential of 180 mV at a current density of 10 mA cm^{-2}, which was lower than the 298 mV of RuO_2, 344 mV of 5% Ru/C and 313 mV of $CoFe_2$/G (Figure 11e). Meanwhile, the Tafel slope of $Ru_{SA}CoFe_2$/G (51 mV dec^{-1}) was lower than that of $CoFe_2$/G (86 mV dec^{-1}), highlighting that the incorporation of single Ru atoms promoted the OER kinetics. DFT calculations revealed that the (110) facet of $CoFe_2$ with 8 pre-adsorbed O ($CoFe_2$(O-8)(110)) could mitigate the excessive decomposition of OOH* into H* and OH*, which was caused by high surface energy active atoms on the pure metallic CoFe alloy, thus stabilizing the key OOH* intermediate. Moreover, the Ru K-edge XANES spectra of $Ru_{SA}CoFe_2$/G showed a lower leading edge at 22121 eV compared to that of RuO_2 (22124 eV), while higher than that of Ru foil (22115 eV). This confirmed that the oxidation state of isolated Ru was +2.5, which was due to the electron transfer from Ru to the pre-adsorbed surface O. The charge transfer from Ru to coordinated surface O in $Ru_{SA}CoFe_2$(O-8)(110) created an electron-deficient Ru centers, which facilitated the adsorption of key intermediates. Thus, the ΔG of RDS (O* → OOH*) decreased from 3.25 eV on $CoFe_2$(O-8)(110) to 2.53 eV on $Ru_{SA}CoFe_2$(O-8)(110), thereby accelerating the OER.

In another example, Wang et al. prepared a MoO_2-supported Ir_1Ni SAA catalyst (denoted as $Ir_1Ni@MoO_2$) via a GR method, where Ir atoms substituted for some Ni atoms in the lattice [109]. .In 1 M KOH solution, the $Ir_1Ni@MoO_2$ exhibited an overpotential of 280 mV at a current density of 10 mA cm^{-2}, which was lower than 310 mV of $Ni@MoO_2$, 316 mV of $IrNi/MoO_2$ (Ir for NPs), and 438 mV of commercial IrO_2. In the chronopotentiometry test, $Ir_1Ni@MoO_2$ exhibited a negligible activity degradation, even after continuous operation for over 100 h at 100 mA cm^{-2} current density, whereas commercial IrO_2 showed a rapid deactivation. *In situ* Raman spectra collected under OER conditions disclosed that the reconstruction potential for the transformation of Ni species into NiOOH decreased from 0.75 V (vs. HgO/Hg) for $Ni@MoO_2$ to 0.6 V (vs. HgO/Hg) for $Ir_1Ni@MoO_2$. These results clearly demonstrate that Ir decoration effectively promotes the reconstruction of Ni species. DFT calculations further revealed that the 5*d* orbitals of Ir in Ir-β-NiOOH strongly hybridized with the O 2*p* orbitals of oxygenated species near the E_F, leading to a much stronger adsorption for the O*, OH*, and OOH* (Figure 11f-h). Consequently, the

calculated OER overpotential decreased from 0.95 V on β-NiOOH to 0.85 V on Ir-β-NiOOH, thereby promoting the OER (Figure 11g, h). The researchers also investigated the performance of SAA catalysts consisting of noble metal substrates and non-precious metal single atoms in electrocatalytic OER. For example, Yang et al. prepared a Bi-RuO_2 SAA oxide (denoted as Bi-RuO_2 SAAO) catalyst via a stepwise wet-chemistry synthesis and calcination, where isolated Bi atoms were confined within the RuO_2 lattice [162]. In 0.5 M H_2SO_4 solution, the Bi-RuO_2 SAAO catalyst exhibited an overpotential of 192 mV at a current density of 10 mA cm^{-2}, which was lower than that of commercial RuO_2 (272 mV) and Bi-Ru oxide (260 mV) (Figure 11i). In addition, in a proton exchange membrane water electrolyzer, using Bi-RuO_2 SAAO as the anode catalyst for OER and commercial Pt/C as the cathode catalyst for HER, only 1.59 V is needed to reach 1.0 A cm^{-2}, 1.77 V to reach 2.0 A cm^{-2}, and 1.97 V to reach 3.0 A cm^{-2} at 60 °C. This outperforms commercial RuO_2 and most of the advanced RuO_2-based catalysts, indicating its industrial application value. Ru K-edge XANES spectra of Bi-RuO_2 SAAO exhibited a shift toward higher near-edge absorption energy and white line intensity compared with RuO_2, indicating the electron transfer between Ru and RuO_2. DFT calculations further revealed that doping Bi atoms into RuO_2 endowed the Ru with more positive valence and the O with more electrons, compared to pure RuO_2 (Figure 11j, k). This optimization of electronic structure further tuned the adsorption energy of oxygen-containing intermediates. Consequently, Bi-RuO_2 SAAO exhibited a lower energy barrier of 0.74 eV for the RDS (*O→*OOH), compared to pure RuO_2 (0.80 eV), thus promoting the OER (Figure 11l)

The OER involves the adsorption and desorption processes between the catalyst and various oxygen-containing intermediates. The optimal adsorption of intermediates can be achieved by regulating the ε_d of the guest or host metal through electronic interactions. Meanwhile, due to the matching electronic structures between the O active sites of oxygen-containing catalysts and oxygen-containing intermediates, they can specifically adsorb oxygen-containing intermediates, inhibit the occurrence of side reactions, and thus exhibit excellent OER performance. Therefore, the regulation of electron transfer or energy band structure in OER should no longer be limited to the two metals of the alloy, but the regulatory effect of O atoms should also be incorporated. Among the content we mentioned, most studies focus on the doping of noble metal guest single atoms into no-noble metals. For example, $RuSACoFe_2/G$ achieves an overpotential as low as 180 mV at a current density of 10 mA cm^{-2}. Therefore, we can focus our attention on the combination of noble metals and no-noble metals in future research.

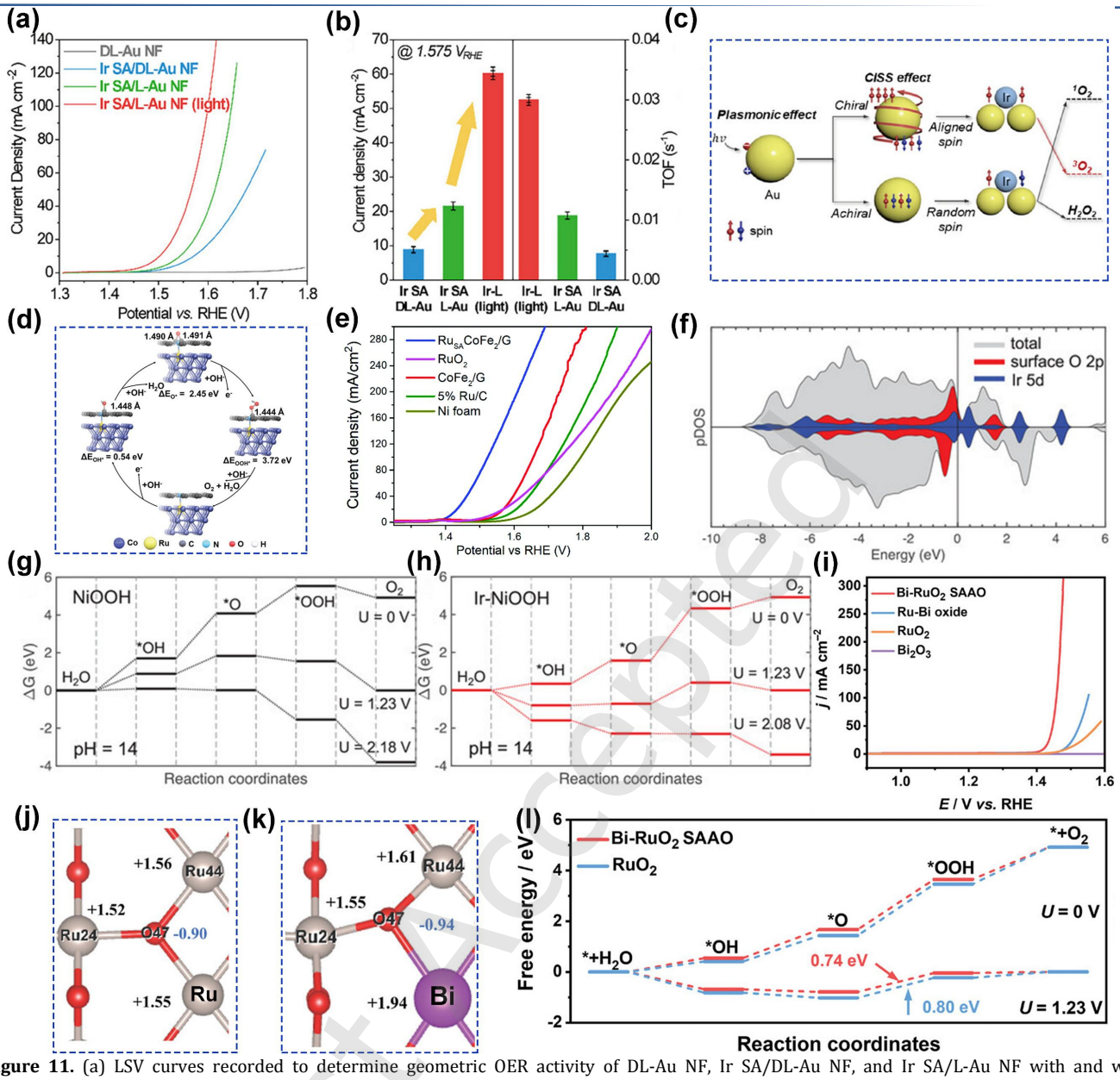

Figure 11. (a) LSV curves recorded to determine geometric OER activity of DL-Au NF, Ir SA/DL-Au NF, and Ir SA/L-Au NF with and without illumination. (b) Specific activities and TOF values of Ir SA/L-Au NF and reference samples at 1.575 V vs. RHE. (c) Schematic illustration of the chirality-induced spin selectivity effect in chiral plasmonic materials. Reproduced with permission from Ref. [166] Copyright 2025, Wiley-VCH. (d) The schematic OER paths on Ru SA-Co-N-C. The H, C, N, O, Co, and Ru atoms are denoted by white, black, cyan, red, blue, and yellow balls, respectively. Reproduced with permission from Ref. [156] Copyright 2022, Wiley-VCH. (e) OER polarization curves of $Ru_{SA}CoFe_2$/G and reference samples. Reproduced with permission from Ref. [79] Copyright 2020, The Royal society of Chemistry. (f) Projected density of states of total, 2*p* orbitals of surface oxygens, and 5*d* orbitals of Ir. Free energy diagram of OER at various potentials on (g) *β*-NiOOH and (h) Ir-*β*-NiOOH. Reproduced with permission from Ref. [109] Copyright 2024, Wiley-VCH. (i) LSVs of Bi-RuO_2 SAAO and reference samples recorded in O_2-saturated 0.5 M H_2SO_4 at a scan rate of 5 mV s^{-1}. The difference in electron transfer between perfect rutile (j) RuO_2 and (k) defect Bi-RuO_2 SAAO. (l) Computed free energy of OER via AEM pathway on the RuO_2 and Bi-RuO_2 SAAO (110) surface. Reproduced with permission from Ref. [162] Copyright 2025, Wiley-VCH.

4.3 Oxygen Reduction Reaction (ORR)

ORR is a very critical reaction in electrochemical energy conversion and storage systems, which occurs mainly at the cathode of fuel cells and metal-air batteries. At the cathode, oxygen can be reduced to H_2O via the $4e^-$ pathway ($O_2 + 4H^+ + 4e^- \rightarrow 2H_2O$) or to by-product H_2O_2 via the $2e^-$ pathway ($O_2 + 2H^+ + 2e^- \rightarrow H_2O_2$) [167]. The four-electron pathway of ORR is mainly divided into an associative mechanism and a dissociative mechanism due to the different activation modes of oxygen and the formation pathways of intermediates [168, 169]. Specifically, the associative mechanism : (1) $* + O_2 + H^+ + e^- \rightarrow *OOH$, (2) $*OOH + H^+ + e^- \rightarrow *O + H_2O$, (3) $*O + H^+ + e^- \rightarrow *OH$, (4) $*OH + H^+ + e^- \rightarrow H_2O + *$; and the dissociative mechanism : (1) $2* + O_2 \rightarrow 2*O$, (2) $*O + H^+ + e^- \rightarrow *OH$, (3) $*OH + H^+ + e^- \rightarrow H_2O + *$. Notably, the SAA catalysts have emerged as promising candidates for promoting the four-electron ORR pathway [14].

Researchers have conducted extensive studies on SAA catalysts formed by doping foreign metal single-atoms into precious metal substrates. For example, Luo et al. fabricated a series of MAu_1 SAA (M = Pd, Pt) catalysts via a stepwise wet-chemistry and electrochemical dealloying method, in which Au atoms were atomically dispersed within the Pd and Pt shell of the PdBi and PtBi intermetallic compounds, respectively [170]. When these catalysts were tested in an O_2-saturated 0.1 M KOH solution, the half-wave potential ($E_{1/2}$) of $PdAu_1$ SAA was 0.928 V vs. RHE, which was higher than those of $PtAu_1$ SAA (0.886 V vs. RHE), PdBi intermetallic

compounds (0.878 V vs. RHE), and commercial Pt/C (0.858 V vs. RHE) (Figure 12a). Meanwhile, $PdAu_1$ SAA also exhibited an ultrahigh MA of 5.37 A $mg_{(Pt + Au)}^{-1}$ at 0.9 V vs. RHE, which was 31.6-fold, 7.6-fold, and 35.8-fold higher than that of $PtAu_1$ SAA, PdBi intermetallic compounds, and commercial Pt/C, respectively. DFT calculations revealed that doping Au atoms into the Pd shell caused a more delocalized electronic surface, whereas doping Au atoms into Pt shell led to a reduced electron density around the neighboring Pt atoms. This difference in electronic structure affected the performance of ORR between $PdAu_1$ SAA and $PtAu_1$ SAA. From the reaction free energy profiles, at an applied potential (U) of 1.23 V vs. RHE, the $PdAu_1$ SAA exhibited a PDS of *OH → H_2O in the ORR, with an energy barrier of 0.74 eV, which was lower than the 0.84 eV barrier of $PtAu_1$ SAA (Figure 12b). Therefore, $PdAu_1$ SAA showed significantly better ORR performance than $PtAu_1$ SAA. In another example, Qiu et al. prepared a $PdPbH_x$ metallenes SAA catalyst via a seed-mediated method by co-confining single Pb atoms and H atoms within Pd metallenes [171]. In an O_2-saturated 0.1 M KOH solution, the $E_{1/2}$ of $PdPbH_x$ metallenes/C ($PdPbH_x$ metallenes uniformly loaded on Ketjen carbon, same below) was 0.958 V vs. RHE, which was much more positive than PdH_x metallenes/C of 0.910 V vs. RHE, PdPb metallenes/C of 0.907 V vs. RHE, and commercial Pt/C of 0.845 V vs. RHE (Figure 12c). At 0.95 V vs. RHE, the $PdPbH_x$ metallenes/C exhibited outstanding MA (1.36 A mg_{Pd}^{-1}) and SA (1.59 mA cm^{-2}), which were 46.9-fold and 31.9-fold higher compared to commercial Pt/C, respectively (Figure 12d). In the *in situ* attenuated total reflection Fourier transform infrared spectra, only a peak (~1175 cm^{-1}) corresponding to *O-O* species was observed in $PdPbH_x$ metallenes/C and PdH_x metallenes/C, revealing that interstitial H atoms could trigger the oxygen dissociative pathway (O_2 → *O-O*). DFT calculations further demonstrated that doping H atoms significantly decreased the ΔG of $*O_2$ → 2*O from 0.81 eV on PdPb to -0.87 eV on $PdPbH_x$ for dissociative pathway, which was also lower than the 0.64 eV of $*O_2$ → *OOH on $PdPbH_x$ for associative pathway, thereby providing a more efficient pathway for ORR (Figure 12e).Furthermore, doping H atoms caused the Pd-4*d* and Pb-6*p* orbitals in $PdPbH_x$ to be more concentrated and closer to the E_F compared to those in PdPb (Figure 12f, g). This phenomenon favored *p-d* orbital overlapping, thereby enhancing electron transfer and exchange efficiency during the ORR process.

Moreover, the preparation of non-precious metal supported SAA catalysts has the potential to eliminate the reliance on precious metals in ORR. For example, Balamurugan et al. prepared RhNi SAA dispersed on the FeV_3O_8 support (denoted as FeV_3O_8@RhNi) via a stepwise hydrothermal reaction, in which the Rh existed as a single atom within Ni NPs [172]. From the XANES analysis, the Ni L-edge position of RhNi SAA exhibited a slight positive shift relative to that of monometallic Ni, while the Rh L-edge position showed a slight negative shift relative to that of monometallic Rh. This phenomenon indicated electron transfer from Ni to Rh in the RhNi SAA, thereby inducing an electrical polarization effect (Figure 12h). Such electrical polarization on RhNi SAA could induce severe band bending to establish a desirable ohmic contact with FeV_3O_8. Thus, the FeV_3O_8@RhNi exhibited a charge-transfer resistance of 311 Ω, which was lower than the 1965 Ω of FeV_3O_8 and the 920 Ω of RhNi SAA. Hence, the polarization-enhanced ohmic contact in FeV_3O_8@RhNi allowed an efficient charge transfer between interface, dramatically improving the electrocatalytic ORR efficiency. In an O_2-saturated 0.1 M KOH solution, the FeV_3O_8@RhNi delivered a $E_{1/2}$ of 0.90 V vs. RHE and reached a limiting current density of -5 mA cm^{-2}, which were higher than those of FeV_3O_8 (0.46 V vs. RHE and -3.5 mA cm^{-2}, respectively), FeV_3O_8@Ni (0.65 V vs. RHE and -4 mA cm^{-2}, respectively) and even the benchmark Pt/C (0.74 V vs. RHE and -4.5 mA cm^{-2}, respectively) (Figure 12i). In another example, Cheng et al. prepared a Pt_1Co_{100} SAA encapsulated in N-doped graphitic carbon nanotubes (denoted as Pt_1Co_{100}/N-GCNT) via melamine pyrolysis method, possessing abundant surface Pt-Co dual sites [173]. The Co L-edge XAS (Total Electron Yield mode, surface-sensitive) showed that the peak intensity of Pt_1Co_{100}/N-GCNT was lower than that of Co/N-GCNT, revealing the apparent charge transfer between surface Co and Pt atoms. This interatomic interaction could optimize the adsorption of oxygen-containing intermediates at the Pt-Co dual sites, thereby promoting the performance of electrocatalytic ORR. In an O_2-saturated 0.1 M $HClO_4$ solution, the $E_{1/2}$ of Pt_1Co_{100}/N-GCNT approached 0.85 V vs. RHE, comparable with the commercial Pt/C. Moreover, the MA of Pt_1Co_{100}/N-GCNT was 2.57 A mg_{Pt}^{-1} at 0.85 V vs. RHE, being 6.4 times higher than that of commercial Pt/C. DFT calculations showed that in Pt_1Co_{100}/N-GCNT, the Co atoms with a lower electronegativity moderately adjusted the electronic structure of Pt, resulting in a more dispersed Pt 5*d* electron, which improved the oxo-phylicity properties of the Pt-Co dual site. Such increased oxo-philicity was favorable for the stable adsorption of OOH*, thus leading to easy cleavage of the O-O bond in subsequent steps (Figure 12j). On the other hand, unlike the bridge adsorption of OH* intermediates on two adjacent Pt atoms in Pt_2Co_{100}/N-GCNT, the Pt_1Co_{100}/N-GCNT exhibited an end-on adsorption of OH* on the Pt site of the Pt-Co active center (Figure 12j, k). The end-on adsorption endowed Pt_1Co_{100}/N-GCNT with a lower OH* desorption energy than the Pt_2Co_{100}/N-GCNT, which benefitted the OH* desorption, indicating the important role of Pt-Co dual sites in ORR.

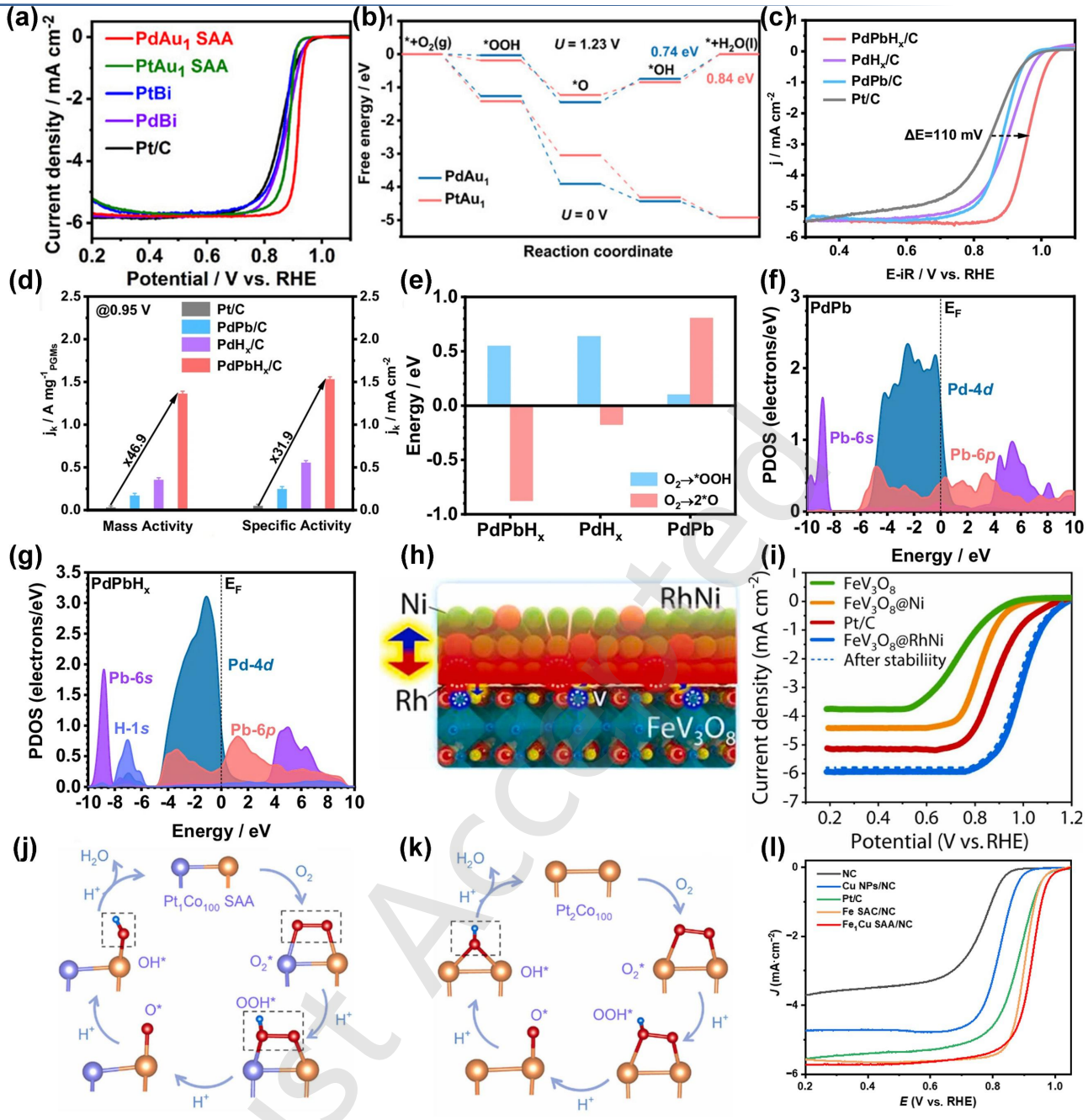

Figure 12. (a) ORR polarization curves of $PdAu_1$ SAA and comparison samples. (b) Free energy profiles of the ORR steps on the $PdAu_1$ and $PtAu_1$ with U = 0 and 1.23 V vs. RHE. Reproduced with permission from Ref. [170] Copyright 2025, Wiley-VCH. (c) ORR polarization curves of PdPbHx/C and comparison samples recorded in O_2-saturated 0.1 M KOH electrolyte. (d) The comparisons in mass activity and specific activity at 0.95 V vs. RHE. (e) The comparison of ΔG of $*O_2 \rightarrow *OOH$ and $*O_2 \rightarrow 2*O$ reaction steps for $PdPbH_x$ metallenes, PdH_x metallenes and PdPb metallenes. The PDOSs of (f) PdPb and (g) $PdPbH_x$. Reproduced with permission from Ref. [171] Copyright 2025, Springer Nature. (h) Schematic image for a formation of electrical polarization of RhNi on FeV_3O_8 originated from the difference of charge density between Rh and Ni. (i) ORR polarization curves for FeV_3O_8@RhNi and comparison samples. Reproduced with permission from Ref. [172] Copyright 2024, Elsevier. The proposed ORR mechanism of (j) Pt_1Co_{100}/N-GCNT and (k) Pt_2Co_{100}/N-GCNT. (grey, carbon; purple, cobalt; orange, platinum; red, oxygen; blue, hydrogen). Reproduced with permission from Ref. [173] Copyright 2022, Elsevier. (l) ORR polarization curves of Fe_1Cu SAA/NC and comparison samples. Reproduced with permission from Ref. [174] Copyright 2024, Springer Nature.

Niu et al. also fabricated an Fe_1Cu SAA catalyst attached to N-doped C carriers (denoted as Fe_1Cu SAA/NC) via a stepwise wet chemistry-pyrolysis method, in which the Fe single atoms uniformly doped in Cu NPs [174]. Notably, the Cu K-edge absorption edge of Fe_1Cu SAA/NC was slightly shifted toward lower energy compared to that of Cu NPs/NC, indicating the existence of charge transfer between Cu and Fe atoms. This synergistic effect between Fe-Cu dual sites could optimize the binding energy of oxygen-containing intermediates, thereby promoting the ORR. Specifically, in an O_2-saturated 0.1 M KOH solution, the $E_{1/2}$ and onset potential of Fe_1Cu SAA/NC were 0.917 and 1.106 V vs. RHE, respectively, which were superior to those of NC (0.761 and 0.857 V vs. RHE), Cu NPs/NC (0.821 and 0.914 V vs. RHE), commercial Pt/C (0.880 and 0.996 V vs. RHE), and Fe SAC/NC (0.900 and 0.964 V vs. RHE) (Figure 12l). Moreover, after 5000 cycle stability tests, the $E_{1/2}$ of Fe_1Cu SAA/NC decreased by only 5 mV, which was smaller than commercial Pt/C of 6 mV, Cu NPs/NC of 8 mV, and the pure NC carrier of 14 mV, indicating its excellent catalytic stability.

For ORR catalysis of SAA catalysts, electron transfer plays a more dominant role than energy band structure, which acts as a bridge linking electron transfer to catalytic performance. Directional and quantitative electron transfer between guest single atoms and host metals induces electronic structure reconstruction, and the resulting energy band optimization tunes oxygen-containing intermediate adsorption and ORR pathways. For example, $PdAu_1$ and $PtAu_1$ SAAs show different electron transfer modes, leading to distinct rate-determining step barriers (0.74 eV vs. 0.84 eV) in the ORR. $PdPbH_x$ SAA's interstitial H-induced electron transfer alters the ORR reaction pathway from $*O_2 \rightarrow *OOH$ to $O_2 \rightarrow *O\text{-}O*$. In non-precious metal-based SAAs, electron transfer from Ni to Rh in in FeV_3O_8@RhNi reduces charge-transfer resistance (311 Ω). In addition, in the discussed research, we can find that the combination of noble metal single atoms and noble metal substrates exhibits the optimal $E_{1/2}$ of ORR. For example, $PdAu_1$ SAA exhibited an $E_{1/2}$ of 0.928 V vs. RHE. We can further adjust the noble metal-noble metal combinations to further regulate the ORR performance.

4.4 CO_2 Reduction Reaction (CO_2RR)

The electrocatalytic conversion of CO_2 into valuable fuels and chemicals powered by renewable energy sources has great potential for reducing carbon emissions [175, 176]. However, the catalytic conversion of CO_2 is difficult due to the molecule's thermodynamic stability and kinetic inertia [177]. Furthermore, CO_2 can be converted into C_1 (e.g., CO, formate, methane, etc.) and multi-carbon products (e.g., ethanol, ethylene, propanol, etc.) through different multi-electron/proton transfer pathways [178]. Thus, catalyst design for enhancing the activity and selectivity of CO_2 catalytic conversion has become a significant challenge. Fortunately, the synergistic effect between metal atoms in the SAA catalysts can significantly improve the activity and product selectivity of electrocatalytic CO_2 conversion [83].

When considering the electrocatalytic reduction of CO_2 to C_1 product, the selectivity of COOH* and HCOO* intermediates can be adjusted by changing the single atom doping species, thus facilitating the production of CO or formate [179]. For example, Li et al. synthesized a Sb_1Cu SAA catalyst with isolated Sb-Cu interfaces via a co-reduction method [180]. The catalyst exhibited the optimal electrocatalytic CO_2 to CO performance when the concentration of Sb reached 5.0 at% (denoted as Sb_1Cu-5). In a flow-cell with CO_2-saturated 0.5 M $KHCO_3$ electrolyte, the Sb_1Cu-5 achieved a CO Faradaic efficiency (FE) of 95% at a current density of -150 mA cm^{-2}, and still maintained a CO FE above 90% even at a high current density of -500 mA cm^{-2} (Figure 13a). The CO FE of Sb_1Cu-5 was higher than the optimal values of pure Sb (34.8%), pure Cu (~68%) and Sb_1Cu-1.5 (89%), respectively. Moreover, Sb_1Cu-5 retained a CO FE of ~95% over 11 h of continuous electrolysis at -100 mA cm^{-2} in a membrane electrode assembly (MEA), confirming the robust stability for CO production. DFT calculations revealed that doping Sb atoms into Cu NPs modulated the electronic structure of Cu substrate. This electronic structure modulation not only reduced the ΔG of $CO_2 \rightarrow$ COOH* step from 0.43 eV on Cu(211) to 0.41 eV on Sb_1Cu-5(211), but also downshifted the ε_d from -2.07 eV of Cu(211) to -2.17 eV of Sb_1Cu-5(211), thus promoting the activation of CO_2 and the desorption of CO (Figure 13b, c). Furthermore, Sb_1Cu-5(211) exhibited a higher ΔG for the $CO_2 \rightarrow$ HCOO* step compared to Cu(211), thereby inhibiting the formation of formate and further promoting CO selectivity (Figure 13b). Alloying Cu catalysts with other isolated metal atoms can also modulate their intrinsic properties, which can promote CO_2 protonation to HCOO* intermediates and thus enhance formate selectivity. For example, Zheng et al. synthesized a Pb-doped Cu SAA catalyst (denoted as Pb_1Cu) using an epoxide gelation method [116]. In a flow-cell with CO_2-saturated 0.5 M $KHCO_3$ electrolyte, Pb_1Cu achieved a formate FE of 96% at a partial current density of -800 mA cm^{-2}, and maintained 92% formate FE even at a high partial current density exceeding -1000 mA cm^{-2} (Figure 13d). DFT calculations revealed that doping Pb atoms induced a lower energy barrier for the protonation CO_2 to HCOO* (0.55 eV) compared to the competing pathway of CO_2 protonation to COOH* (0.64 eV), thermodynamically favoring the selective formation of formate intermediates. Furthermore, the Heyrovsky step ($(H^+ + e^-) + H^* \rightarrow H_2 + *$) exhibited a higher energy barrier (0.96 eV) than the CO_2 protonation to HCOO* step, which inhibited the HER and enhanced the formate selectivity (Figure 13e). Both of the aforementioned studies have achieved the highly selective production of CO and formate, respectively, yet their carbon source tracing systems are notably inadequate. Although both works have indirectly corroborated the correlation between the C element in the products and CO_2 by comparing the catalytic current densities under CO_2 atmosphere and inert atmosphere (Ar/N_2), such evidence can only reflect the participation of CO_2 in the reaction. It fails to clarify the unique source of C at the atomic level, resulting in insufficient rigor of the argumentation. To accurately quantify the net conversion efficiency of CO_2 to target products (CO/formate), a ^{13}C isotope labeling strategy can be adopted. Using $^{13}CO_2$ as the reaction gas source, combined with nuclear magnetic resonance (NMR) for quantitative characterization of the products. By tracking the enriched signal of ^{13}C in CO or formate, the source of C (either CO_2 or bicarbonate (HCO_3^-) in the electrolyte) can be directly distinguished. Furthermore, this enables the accurate calculation of the yield of target products from CO_2 reduction, providing core support for the objective evaluation of catalytic performance.

Electrocatalytic CO_2RR to multi-carbon (C_{2+}) products possessed a significant challenge because it involved the activation of lazy CO_2 molecular and the coupling of adsorbed C_1 intermediate species (e.g. *CO, *CHO etc.) (C-C coupling) [181]. Copper is known as the only metal to catalyze the conversion of CO_2 to C_{2+} products due to its unique electronic structure. However, the slow C-C coupling kinetics on the surface of pure Cu severely inhibit the generation of large amounts of C_{2+} products [182-184]. The synergistic effect of single-atoms and Cu substrates in SAA can effectively increase C_{2+} yield. For example, Xiao et al. fabricated a Pr-doped Cu SAA with a Pr loading of 6.0 wt.% (denoted as Pr@Cu-2) through a chemical reduction approach, employing $NaBH_4$ as the reducing agent [185]. In a flow-cell with CO_2-saturated 1.0 M KOH solution, the Pr@Cu-

2 achieved a maximum C_2H_4 FE of 64.2% at a current density of 1200 mA cm^{-2} (Figure 13f). Meanwhile, the C_2H_4 partial current density of Pr@Cu-2 outperformed those of Cu, Pr@Cu-1 (3 wt.% Pr), and Pr@Cu-3 (23 wt.% Pr) across the entire potential range of -0.8 to -1.8 V vs RHE, reaching a peak value of 762 mA cm^{-2} at -1.6 V vs RHE (Figure 13g). Furthermore, when integrated into a 100 cm^2 MEA electrolyzer, the Pr@Cu-2 maintained a continuous C_2H_4 production rate of 21.3 mL min^{-1} at 20 A for over 200 h. These results highlighted the robustness and scalability of Pr@Cu-2 for large-scale CO_2-to-C_2H_4 conversion. DFT calculations revealed that the doping Pr atoms reduced the activation barriers of water from 2.7 eV on pristine Cu to 1.44 eV on Pr@Cu-2, which promoted water dissociation and the interfacial proton (H^+) supply, in turn accelerating the combination of *CO and H^+ to generate the *CHO intermediate. The accumulation of *CHO intermediate reduced the C-C coupling energy between *CHO and *CO from 0.065 eV on pristine Cu to -0.00012 eV on Pr@Cu-2, thereby facilitating efficient C_2H_4 production. In another example, Cao et al. modified the electronic structure of metallic Cu NPs via Bi single-atom to promote efficient C-C coupling, thereby achieving the optimal C_{2+} FE of 73.4% [115]. In a bid to further enhance the selectivity toward C_{2+} products, Jin et al. synthesized a 0.7%-Mo_1Cu SAA catalyst (0.7% mol ratio for Mo and Cu) with multiple active sites via a electroreduction method [81]. In a flow-cell with CO_2-saturated 1M KOH solution, the 0.7%-Mo_1Cu achieved a FE of 86.4% for C_{2+} products (C_2H_4, C_2H_5OH, and C_3H_7OH, etc.) at 800 mA cm^{-2}, superior to that of Cu (65.2%) (Figure 13h). Moreover, the FE of C_{2+} maintained above 74.3% even at 1.8 A cm^{-2}, and the partial current density of C_{2+} reached a remarkable 1.33 A cm^{-2}, more than twice that of Cu (0.6 A cm^{-2}). It is worth nothing that 0.7% Mo_1Cu gains a long-term stability up to 40 h at 0.8 A cm^{-2} with the FE of C_{2+} kept ≈84% in a flow-cell-reactor. DFT calculations revealed that the atomically dispersed Mo sites facilitated water dissociation to generate active *H species. Concurrently, the Cu sites (Cu^0) away from Mo atom (Mo_{far}-Cu) served as active centers for CO_2 activation to *CO intermediates. Owing to the higher electronegativity of Mo (2.16) compared to Cu (1.90), electron transfer from Cu to Mo occurred during alloy formation, which elevated the oxidation state of Cu sites ($Cu^{\delta+}$) adjacent to Mo atom (Mo_{near}-Cu). These Mo_{near}-Cu sites exhibited enhanced adsorption capacity for both *H and *CO, thereby favoring the hydrogenation of *CO to the *CHO intermediate. This reduced the coupling energy barrier between *CHO and *CO from 0.6 eV on Cu to 0.55 eV on Mo_{near}-Cu, thereby promoting the formation of C_{2+} products (Figure 13i). Such multi-metallic active sites synergistic catalysis represents a unique merit of SAA catalysts, which is essentially inaccessible in conventional N-doped carbon-supported SACs.

Moreover, Wang et al. also compared the role of Ag single atom (denoted as Ag_1Cu NW) and Ag nanoparticles (denoted as AgCu NW) on Cu substrates in controlling the C_{2+} product selectivity [186]. In a flow-cell with CO_2-saturated 1 M KOH electrolyte, the Ag_1Cu NW achieved the optimal ethanol FE of 56.3% with a current density of 172.8 mA cm^{-2} at -1.0 V vs. RHE, while the AgCu NW reached the maximum ethylene FE of 54.9% with a current density of 156.0 mA cm^{-2} at -1.1 V vs RHE (Figure 13j). Moreover, compared to AgCu NW, the Ag_1Cu NW exhibited a more than 10-fold increase of C_2 selectivity in CO_2 reduction to ethanol, with ethanol-to-ethylene ratio increased from 0.41 over AgCu NW to 4.26 over Ag_1Cu NW. *Quasi in situ* XPS of Ag_1Cu NW spectra revealed that the oxidation state of Ag increased gradually from open-circuit voltage to -1.2 V vs. RHE, and this variation trend was consistent in both CO_2 and Ar atmospheres. *Operando* Raman spectroscopy measurements further revealed that this change is due to Ag promoting the dissociation of water to form HO-Ag_1Cu NW. DFT calculations revealed that the *in situ* formation of HO-Ag_1Cu NW could reduce the ΔG of *CO hydrogenation to *CHO from 1.16 eV on Cu NW to 0.83 eV, which facilitated the asymmetric *CO-*CHO coupling over the adjacent paired Cu atoms (HO-Ag_1-Cu-Cu) to favor ethanol production (Figure 13k). In contrast, doping Ag clusters reduced the energy barrier for *CO_2 hydrogenation to *COOH from 0.83 eV on Cu to 0.63 eV on AgCu NW, facilitating *CO production via the *COOH → *CO pathway. Additionally, the *CO arising from Ag clusters was transferred to Cu sites, leading to *CO accumulation. Such aggregation of *CO lowered the ΔG of symmetrical *CO-*CO coupling, thereby facilitating symmetric *CO-*CO coupling and thus favoring ethylene production. Such difference in product selectivity was also observed by Wang and coworkers by testing an Ag single atoms-modified Cu catalyst (denoted as AgCu-SAA) and an Ag NPs-modified Cu catalyst (denoted as AgCu-Nano) [119]. In a flow-cell with CO_2-saturated 1 M KOH electrolyte, the FE of C_{2+} products over AgCu-SAA reached 83.4% at 900 mA cm^{-2} and remained at 74.8% even at a high current density of 1100 mA cm^{-2}. In contrast, the C_{2+} FE over AgCu-Nano was only 57.83% at 900 mA cm^{-2}, while the CO FE was much higher than that over AgCu-SAA. DFT calculations revealed that the energy barrier for *CO transfer from Ag clusters to adjacent Cu sites in AgCu-Nano was significantly higher than that for direct desorption to the electrolyte, favoring *CO desorption to become CO gas (Figure 13l). In contrast, the energy barrier for *CO transfer from isolated Ag atoms to adjacent Cu sites in AgCu-SAA was comparable to that of direct desorption to the electrolyte. Notably, the subsequent exothermic adsorption of *CO on Cu sites promoted *CO inter-migration, which favored *CO to participate in C-C coupling to form C_{2+} products (Figure 13m).

The CO_2RR involves adsorption processes of multiple intermediates, and the adsorption differences among different intermediates lead to variations in catalytic selectivity. Therefore, the energy band structure is crucial in regulating the products of CO_2RR. For example, the doping of Sb atoms into Cu NPs downshifts the ε_d of Cu, thereby facilitating the desorption of CO and achieving a CO FE of 95%. For the CO_2 reduction to C_{2+} products, the core challenge of C-C coupling is also directly solved by the optimized energy band structure, while electron transfer only provides the necessary conditions for such band optimization. In the Pr@Cu-2 SAA, the electron transfer induced by Pr only helps reduce the energy barrier of water dissociation, while the key to promoting the formation of *CHO intermediates and lowering the C-C coupling energy

barrier lies in the energy band reconstruction triggered by this electron transfer. In the 0.7%-Mo_1Cu SAA, the electron transfer from Cu to Mo only serves to elevate the oxidation state of adjacent Cu sites, whereas the enhanced adsorption capacity of Cu sites for *H and *CO as well as the reduction of coupling energy barrier are essentially attributed to the optimized energy band structure. Given the critical role of energy band structure in regulating CO_2RR products, Cu is regarded as the preferred host metal in the CO_2RR. When introducing guest metals to modulate the electronic structure of Cu-based catalysts, key reaction processes including proton generation, *CO intermediate formation, C-C coupling, and product desorption should be comprehensively considered.

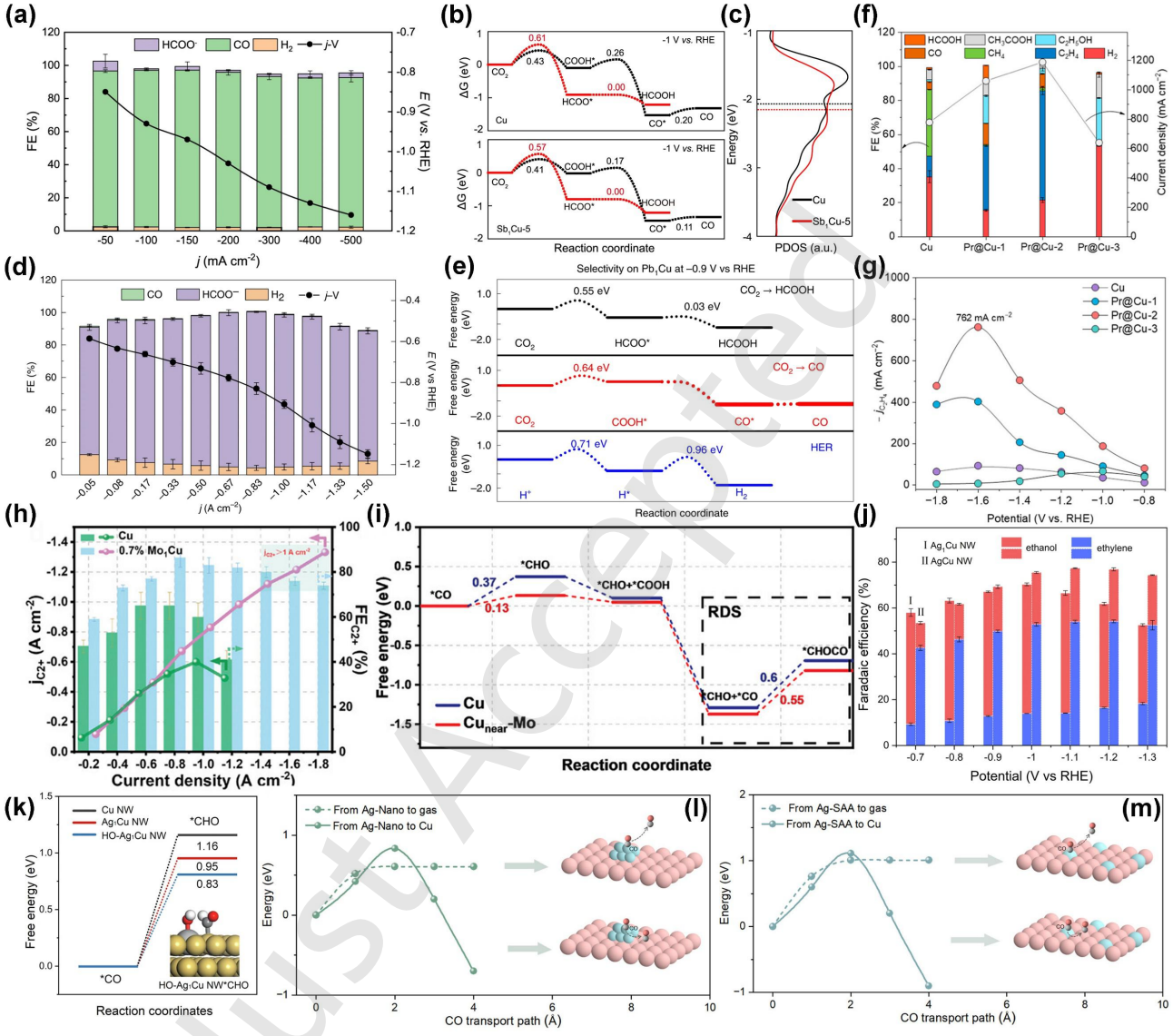

Figure 13. (a) FEs of all CO_2RR products at different current densities and the corresponding j-V curve of Sb_1Cu-5. (b) Calculated Gibbs free energy diagrams for CO_2RR to CO and HCOOH on Cu (211) and Sb_1Cu-5 (211). (c) The projected d-band states of Cu atoms on Cu (211) and Sb_1Cu-5(211); Reproduced with permission from Ref. [180] Copyright 2023, Springer Nature. (d) FEs of all CO_2RR products at different current densities and the corresponding j-V curve of Pb_1Cu SAA. (e) Free-energy diagrams for the competition between CO_2RR producing formate or CO and the HER reaction at the electrode potential of -0.9 V vs RHE. Reproduced with permission from Ref. [116] Copyright 2021, Springer Nature. (f) FEs of different products on Pr@Cu at -1.6 V vs RHE and the corresponding current density. (g) C_2H_4 partial current density of Pr@Cu at different potentials. Reproduced with permission from Ref. [185] Copyright 2025, American Chemical Society. (h) FE and partial current density of C_{2+} over Cu and 0.7% Mo_1Cu. (i) Free energy diagram for C-C coupling of *CO to *CHOCO with *H at 0 V; Reproduced with permission from Ref. [81] Copyright 2025, Wiley-VCH. (j) FEs for CO_2-to-C_2 products on Ag_1Cu NW and AgCu NW. Error bars represent the standard deviation of three independent measurements. All voltage was recorded without *i*R correction. (k) Gibbs free energy diagrams for *CO hydrogenation to *CHO over Cu NW, Ag_1Cu NW and HO-Ag_1Cu NW. Reproduced with permission from Ref. [186] Copyright 2024, Springer Nature. (l) Energy barriers of *CO desorption on Ag-Nano models; upper inset: illustration of CO desorbed from Ag-Nano into the gas phase; lower inset: illustration of CO desorbed from Ag-Nano and transferred to the Cu surface. (m) Energy barriers of *CO desorption on Ag-SAA models; upper inset: illustration of CO desorbed from Ag-SAA into the gas phase; lower inset: illustration of CO desorbed from Ag-SAA and transferred to the Cu surface. Reproduced with permission from Ref. [119] Copyright 2025, American Chemical Society.

4.5 NH_3 synthesis reaction

NH_3 is not only an indispensable key chemical raw material in many industrial and agricultural processes, but also an important carrier of clean energy [187, 188]. However, the traditional Haber-Bosch process, widely employed for industrial NH_3 synthesis, is plagued by high energy consumption and significant greenhouse gas emissions [41, 189]. In the search for sustainable alternative, electrochemical reduction reactions, including N_2-to-NH_3 (NRR), NO-to-NH_3 (NORR), NO_2^--to-NH_3 (NO_2RR), and NO_3^--

to-NH_3 (NO_3RR), have emerged as compelling strategies for sustainable NH_3 synthesis under ambient conditions [190-192]. SAA catalysts hold promise for advancing this goal.

The overall chemical reaction formula for electrochemical NRR is $N_2 + 6H^+ + 6e^- \rightarrow 2NH_3$, and the key lies in N_2 adsorption, activation, and inhibition of the side reaction [193]. Adjusting the electronic structure of SAAs can promote N_2 activation and suppress competing reactions such as HER, thereby achieving excellent NRR performance. For example, Li et al. prepared a $PdFe_1$ SAA with Fe loading of 3.91 at% via one-step wet chemistry strategy [194]. In an H-type electrolytic cell with N_2-saturated 0.5 M $LiClO_4$, the $PdFe_1$ achieved the highest NH_3 yield of 111.9 $\mu g h^{-1} mg^{-1}$ at -0.2 V vs. RHE, which was 7.1 and 2.4 times higher than that of Pd and $PdFe_x$ (x > 1), respectively(Figure 14a). UV-vis spectrophotometry was employed to verify the absence of NH_3/NO_x impurities in the Ar, N_2, $^{14}N_2$ and $^{15}N_2$ gases used in the experiments. Meanwhile, the ammonia yield was jointly quantified by ^1H NMR and UV-vis spectrophotometry, which ruled out the interference of pH variations on the quantitative results and thus ensured the credibility of the experimental data. DFT calculations revealed that the electron-deficient Fe acted as a Lewis acid site, attracting lone pair electrons of Lewis base N_2 (σ donation) to promote N_2 adsorption and activation. Furthermore, doping Fe atoms modulated the electronic structure of $PdFe_1$, resulting in more occupied electron state at the E_F and a lower work function than pure Pd, thereby facilitating rapid electron transport to enhance NRR kinetics. Specifically, $PdFe_1$ exhibited an energy barrier of 0.72 eV for the RDS (NHNH → $*NHNH_2$), lower than that of 1.79 eV on Pd for its RDS ($*N_2$ → $*N_2H$) (Figure 14b). Additionally, $PdFe_1$ exhibited strong H-adatom binding, which could impede H_2 formation/desorption, thereby inhibiting the HER and improving NRR selectivity. However, given the large N≡N dissociation energy (942 kJ mol^{-1}) that limits N_2-to-NH_3 efficiency and the lower N=O dissociation energy (631 kJ mol^{-1}) in NO, the use of SAA for electrocatalytic NORR conversion provides a feasible approach for efficient NH_3 synthesis [192, 195, 196]. For example, Chen et al. prepared a Pd_1Cu SAA catalyst with single atomic Pd confined in a Cu matrix via a facile cation exchange strategy [73]. In a gastight H-type cell with NO-saturated 0.5 M Na_2SO_4, the Pd_1Cu achieved the maximum NH_3 FE of 96.7% with a corresponding NH_3 yield rate of 305.8 $\mu mol\ h^{-1}\ cm^{-2}$ at -0.4 V vs. RHE (Figure 14c).It is widely recognized that the indophenol blue (IB) method exhibits decreased accuracy and reliability at high concentrations (>2.94×10^{-5} mol/L) and in acidic environments [197, 198]. Therefore, quantifying NH_3 yield using the IB method in the referenced study may lead to a certain overestimation of the actual yield. DFT calculations revealed that the Pd_1Cu_2 sites of Pd_1Cu donated more electrons to *NO (-0.62|e|) than the Cu_3 sites of Cu (-0.48|e|), which resulted in a more elongated N=O bond length (1.251 Å vs 1.245 Å) and enhanced NO activation on Pd_1Cu (Figure 14d). Specifically, the activation barrier of the RDS (*NO to *NHO) decreased from 0.84 eV on Cu to 0.52 eV on Pd_1Cu, thereby promoting the NO-to-NH_3 conversion. In addition, *operando* Pd K-edge XANES profiles of Pd_1Cu exhibited no adsorption edge alteration relative to the pristine sample over the working potential range of OCP to -0.4 V vs. RHE. Meanwhile, the corresponding EXAFS spectra displayed only the dominant peak at ~2.19 Å assigned to the Pd-Cu bond, confirming the structural stability of Pd_1Cu. Accordingly, Pd_1Cu achieved stable operation at 210 mA cm^{-2} for 200 h in a flow cell, demonstrating promising industrial application potential.

Compared to N_2 and NO, NO_2^- has higher water solubility and lower N=O bond dissociation energy. Thus, the electrocatalytic NO_2RR is kinetically more favorable for NH_3 electrosynthesis than the NRR and NORR [190, 199]. Additionally, this reaction can convert NO_2^- pollutants, contributing to ecosystem protection. The total reaction pathway is $NO_2^- + 7H^+ + 6e^- \rightarrow NH_3 + 2H_2O$, which involves various by-products and is hampered by the competitive HER [200, 201]. SAA can precisely adjust the electronic structure of the catalyst to catalyze NO_2RR. For example, Xiang et al. prepared a $CuRh_1$ SAA tandem catalyst via stepwise cation exchange and thermal annealing methods [200]. In an H-cell containing 0.5 M Na_2SO_4 with 0.1 M $NaNO_2$ solution, the $CuRh_1$ exhibited a maximum NH_3 FE of 94.1% at - 0.6 V vs. RHE, corresponding to an NH_3 yield rate of 448.8 $\mu mol\ h^{-1}\ cm^{-2}$, which were both higher than those of pure Cu (Figure 14e). In Rh K-XANES spectra, $CuRh_1$ showed a slight negative shift in the absorption edge position relative to Rh foil, indicating partial electron transfer from Cu to Rh_1. DFT calculations revealed that the electron accumulation on Rh_1 sites in $CuRh_1$ enabled a larger electron transfer to $*NO_2$ (-0.45 |e|) in comparison with pure Cu (-0.39 |e|), thereby accelerating the conversion of NO_2^- to *NO via the pathway of NO_2^- → $*NO_2$ → *NOOH → *NO. Additionally, due to the lower energy barrier of RDS (*NO → *NHO) on Cu sites (0.14 eV) than on Rh_1 sites (0.45 eV), the *NO species that was generated on Ru_1 sites was transferred to Cu sites and further hydrogenated to NH_3 (Figure 14f). On the other hand, $CuRh_1$ showed a more negative binding free energy for NO_2^- adsorption (-0.44 eV) than for H (-0.07 eV), inhibiting competitive HER and improving NH_3 selectivity. In another example, Wang et al. synthesized In_1Cu (In: 3.4 at%) SAA using a straightforward cation exchange method [202]. In an H-shaped cell containing 0.5 M Na_2SO_4 and 0.1 M $NaNO_2$, the In_1Cu exhibited a 95.1 % of NH_3 FE at - 0.6 V vs. RHE and a NH_3 yield rate of 502 $\mu mol\ h^{-1}\ cm^{-2}$, outperforming pristine Cu and most of NO_2RR catalysts. Meanwhile, the NH_3 FE on In_1Cu electrocatalytic NO_2RR was higher than N_2, H_2 and N_2H_4 byproducts at all potential (Figure 14g). DFT calculations revealed that di-nuclear sites of In_1-Cu donated more electrons to $*NO_2$ (-0.28 |e|) and elongated the N=O bond to 1.981 Å, compared to $*NO_2$ on Cu (-0.23 |e|, 1.869 Å), thereby promoting NO_2^- adsorption and activation. Meanwhile, the electronic interaction between In_1 and Cu downshifted the ε_d from - 2.38 eV on pristine Cu to -2.46 eV on In_1Cu, resulting in weakened In_1Cu-*NO interaction. This decreased the energy barrier of RDS (*NO → *NHO) from 0.71 eV on Cu to 0.48 eV on In_1Cu, thereby promoting the NO_2RR (Figure 14h). Furthermore, the In_1Cu showed a more negative binding free energy for $*NO_2$ (-0.38 eV) than *H (0.62 eV), improving the NH_3 selectivity. While the calculations of NH_3 FE and yield in both studies are technically valid, from a rigorous analytical perspective,

neither study performed essential control experiments—namely, blank tests in the absence of NO_2^- to exclude potential NH_3 contributions from electrolyte impurities or the catalyst itself. Furthermore, when unbuffered neutral salt electrolytes (e.g., sodium sulfate) are used, prolonged electrolysis at low potentials consumes H^+ ions and increases the electrolyte pH. As UV-vis spectrophotometry is pH-sensitive, this tends to cause deviations in ammonia quantification. Meanwhile, pH fluctuations introduce errors in electrode potential calculation and reduce result reproducibility. To avoid these adverse effects, buffered electrolytes are recommended instead of unbuffered neutral salts to maintain a stable electrolyte environment [198].

Electrochemical production of high-value NH_3 from NO_3^- waste shows promise for industrial wastewater treatment. The total reaction pathway is $NO_3^- + 9H^+ + 8e^- \rightarrow NH_3 + 3H_2O$, but the complex reaction pathway form many undesired by-products [203, 204]. Through precise modulation of active sites, Cu-based SAA can significantly enhance the performance of the NO_3RR. For example, Du et al. prepared a PdCu SAA with Pd atoms doped in Cu NPs using a spontaneous galvanic replacement reaction [205]. In an H-cell containing 0.5 M Na_2SO_4 with 600 ppm NO_3^-, the PdCu SAA exhibited an ultrahigh NH_3 FE of 97.1% and an NH_3 yield rate of 15.4 μmol cm^{-2} h^{-1} under -0.6 V vs. RHE, which was much better than that of Cu (NH_3 FE of 81.2% with a yield rate of 11.0 μmol cm^{-2} h^{-1}) (Figure 14i). With the increase of the applied voltage from 0 to -1.3V, characteristic peaks corresponding to CuO (298 and 629 cm^{-1}), Cu_2O (436 cm^{-1}), and PdO (728 and 929 cm^{-1}) emerged gradually in the *operando* Raman spectra of PdCu SAA. This can be attributed to the generation of OH* radical from H_2O dissociation, which raises the oxidation states of Cu and Pd. DFT calculations further revealed that isolated Pd atoms in the PdCu SAA could generate *H from H_2O dissociation for the hydrogenation of $*NO_3$. Furthermore, electron transfer from Cu to Pd modulated the electronic properties, enhancing the adsorption and activation of key intermediates (NO_3^-, *NOO, *NOOH, etc). This decreased the energy barrier of RDS (*NOO → *NOOH) from 0.39 eV on Cu(100) to 0.1 eV for RDS (*NOH → *NHOH) on PdCu(100), thereby promoting the conversion of NO_3^- to NH_3. In another example, Cai et al. fabricated a single-atom Ni-alloyed Cu catalyst (denoted as Ni_1Cu-SAA) via *in situ* electrochemical reduction method [206]. In an H-type cell containing 0.5 M K_2SO_4 with 200 ppm NO_3^-, the maximum NH_3 FE of Ni_1Cu-SAA reached ~100% at -0.55 V vs. RHE, which was higher than that of Cu nanosheets (93.5%) at - 0.65 V vs. RHE. Additionally, Ni_1Cu-SAA exhibited a NH_3 yield rate of 326.7 μmol h^{-1} cm^{-2} under ambient conditions at -0.55 V vs. RHE, which was 10.7 times higher than that of Cu nanosheets (Figure 14j). DFT calculations revealed that doping Ni atoms increased the ε_d of the catalyst relative to the E_F and shifted upward the position of anti-bonding N 2*p* states (Figure 14k). As a result, more anti-bonding states above the E_F became unoccupied, which increased the bond strengths between NOOH* and active sites from -1.70 eV on Cu to -2.55 eV on Ni_1Cu-SAA (Figure 14l). The strong adsorption of NOOH* intermediates on Ni_1Cu-SAA decreased the NO_3RR limiting potential from -0.66 V on Cu to -0.33 V on Ni_1Cu-SAA, thus improving the NH_3 production. Compared with the SAAs formed by dispersing Ni within Cu, Ni single-atom catalysts supported on N-doped carbon substrates show inferior electrocatalytic performance toward the NO_3RR. For instance, Ajmal et al. reported that Ni single atoms anchored on N-doped graphene (denoted as NiSA@NG) delivered an NH_3 yield rate of 86 ug h^{-1} cm^{-2} (5.06 μmol h^{-1} cm^{-2}) with an NH_3 FE of 51% in an H-type cell [207]. Upon further doping with B atoms to tailor the electronic structure of Ni sites, the NH_3 FE was increased to 95% and the NH_3 yield rate promoted to 168 ug h^{-1} cm^{-2} (9.87 μmol h^{-1} cm^{-2}). Nevertheless, these values remain substantially lower than the catalytic efficiency of the Ni_1Cu-SAA system. This indicates that the electronic modulation between the host and guest metals in the alloy catalyst is significantly superior to that of N and other heteroatoms in N-doped C matrix.

In the electrocatalytic reduction of N-containing species (N_2, NO, NO_2^-, NO_3^-) to NH_3, electron transfer plays a dominant role, far exceeding the auxiliary regulation of energy band structure. All the SAA catalysts discussed herein demonstrate that electron transfer directly drives the adsorption and activation of N-containing species by injecting electrons to weaken N≡N and N=O bonds. It also regulates the energy barrier of the rate-determining step, accelerates reaction kinetics, and optimizes the adsorption selectivity of target intermediates and *H to inhibit HER. The optimization of energy band structure (e.g., ε_d shift, electron state near EF) is only a macroscopic manifestation of electron transfer, which cannot independently improve catalytic performance. Transition metals including Cu and Pd serve as the preferred host substrates, while Fe, Rh, Ni and other single atoms act as guest dopants, enabling the construction of the most favorable electronic structure. Such host-guest combinations realize directional electron transfer via the electronegativity difference, endowing active sites with electron-deficient or electron-rich states to efficiently activate N≡N, N=O, N–O and other chemical bonds.

5. Conclusion and perspectives

SAAs, integrating the ultrahigh atomic utilization efficiency of SACs and the synergistic electronic modulation of alloy catalysts, have emerged as a transformative platform for energy-related electrocatalysis. In this review, we summarized the recent progress of SAAs from the perspective of synthetic methods, unique electronic structures, and applications in the field of energy-related electrocatalysis. First, we summarized the regularly used synthetic methods for the fabrication of SAAs, including impregnation, GR, electrochemical reconstruction, sequential reduction, and ALD. Secondly, theoretical studies have elaborated on the unique free-atom-like *d*-states characteristics of the guest metal in SAAs and compared the effects of the resulting electron transfer and energy band structure changes on catalytic reactions. Finally, the applications of SAAs in energy-related electrocatalysis were described to understand the structure-performance relationship and catalytic mechanism, such as Pt/Ir -based SAAs for water splitting with ultra-low overpotential, Pd-based SAAs for ORR with high $E_{1/2}$, Cu-based SAAs for CO_2RR with high C_{2+} selectivity, and Pd/Cu-based SAAs for NH_3 synthesis with near-100% Faradaic efficiency.

Despite these advances, SAAs still face fundamental and practical challenges that hinder their widespread application. Specifically, these challenges include the difficulty in precisely controlling active site dispersion and distance, the ambiguous evolution mechanism of SAAs under realistic reaction environments, the limitation of binary SAA systems, the lack of low-cost scalable synthesis methods, the inefficiency of trial-and-error design strategies, and the barriers to integration into practical devices and establishment of industry standards. Below, we propose a clearly targeted roadmap to address these issues and guide future development:

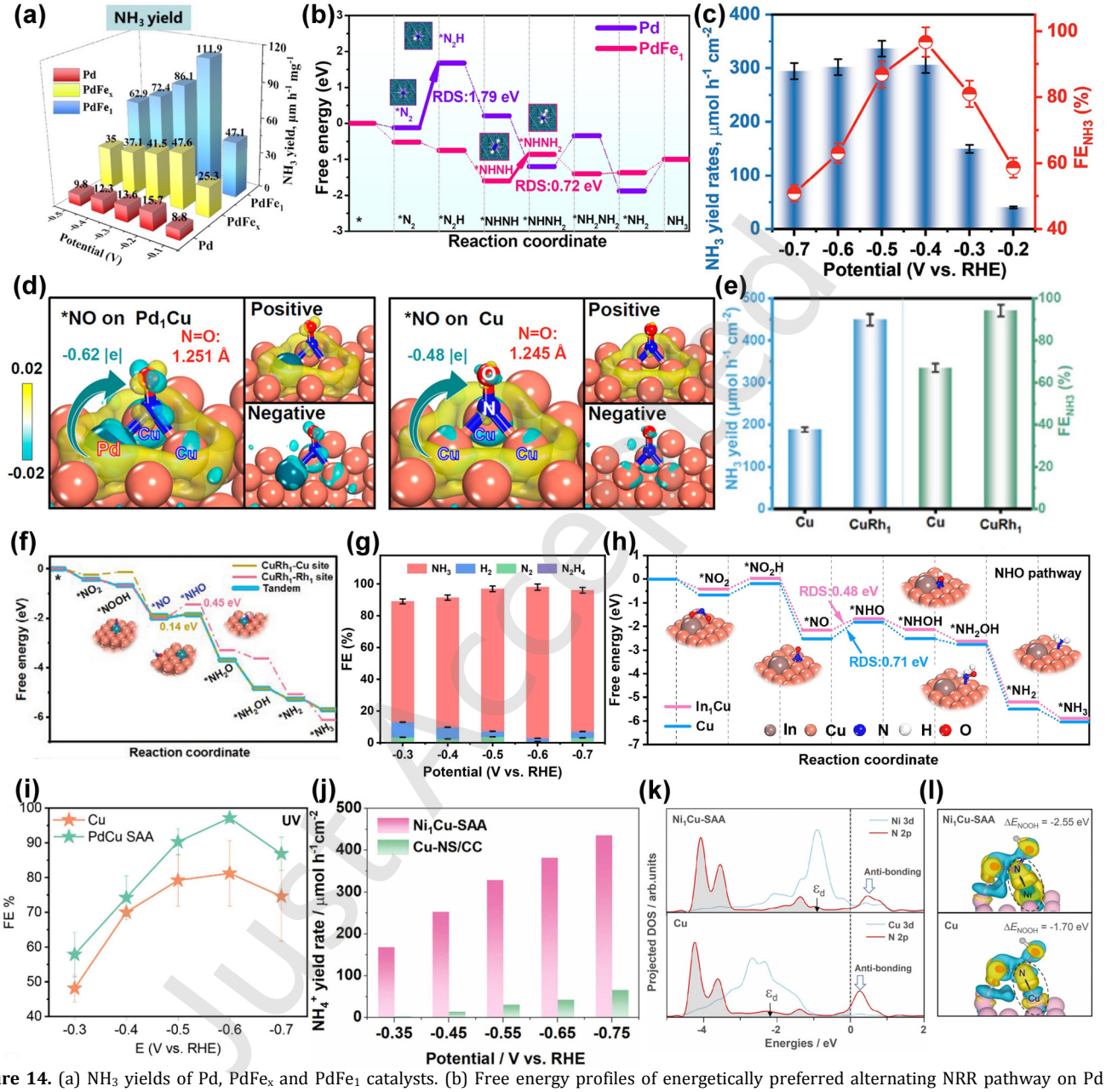

Figure 14. (a) NH_3 yields of Pd, $PdFe_x$ and $PdFe_1$ catalysts. (b) Free energy profiles of energetically preferred alternating NRR pathway on Pd and $PdFe_1$ at zero applied energy; Reproduced with permission from Ref. [194] Copyright 2022, Wiley-VCH GmbH. (c) NH_3 yield rates and NH_3 FE of Pd_1Cu at various potentials. (d) Charge density differences of *NO on Cu and Pd_1Cu, in which the isosurface is taken as 0.02 e/A^3; Reproduced with permission from Ref. [73] Copyright 2024, American Chemical Society. (e) Catalyst performance comparison between Cu and $CuRh_1$ at -0.6 V vs. RHE. (f) Free energy profiles of NO_2RR on Cu and $CuRh_1$; Reproduced with permission from Ref. [200] Copyright 2024, Wiley-VCH GmbH. (g) Different products FEs of In_1Cu for electrocatalytic NO_2RR at different potentials. (h) Free energy diagrams of NO_2RR pathways on Cu and In_1Cu; Reproduced with permission from Ref. [202] Copyright 2024, Elsevier. (i) FE results of PdCu SAA and Cu based on the UV-visible spectroscopy detection method for NH_3; Reproduced with permission from Ref. [205] Copyright 2023, American Chemical Society. (j) Comparison of the NH_4^+ yield rates for Ni_1Cu-SAA and Cu-NS/CC. (k) The projected-DOS for NOOH* chemisorbed on Ni_1Cu-SAA and Cu. (l) Charge density difference for NOOH* adsorption on Ni_1Cu-SAA and Cu. The blue and yellow electronic clouds indicate charge depletion and accumulation, respectively; Reproduced with permission from Ref. [206] Copyright 2022, Elsevier.

5.1 Resolve Core Scientific Challenges

(1) Precise control of active site dispersion and distance

The free-atom-like *d*-states of SAAs are highly dependent on the spatial isolation of guest atoms, yet high-temperature treatment and long-term catalysis often induce aggregation. Future efforts should focus on: (i) Developing novel synthesis strategies (e.g., ligand-protected ALD, defect-engineered hosts) to enhance the anchoring of guest atoms and suppress aggregation; (ii) Combining DFT calculations and advanced *in situ* characterization to investigate the "site

distance effect", revealing how inter-guest distances (e.g., 3-5 Å vs. >5 Å) regulate *d*-band width and orbital hybridization, and establishing a quantitative relationship between atomic distance and catalytic selectivity.

(2) Dynamic tracking of active sites under working conditions

Ex situ characterization techniques including ex situ HAADF-STEM, ex situ XAS, and ex situ XPS are incapable of tracking the dynamic evolution of guest-host interactions under realistic catalytic conditions, such as atomic migration, valence state fluctuation, surface segregation, and structural reconstruction. These dynamic structural changes are closely associated with catalytic activity and stability, yet remain poorly understood. Therefore, future research priorities should be placed on: (i) Establishing multifunctional integrated *in situ*/*operando* characterization platforms (e.g., *in situ* HAADF-STEM combined with *in situ* IR spectroscopy or *operando* XAS) to monitor in real time the dynamic charge transfer behavior and coordination environment evolution; (ii) Concentrating on critical reaction stages, especially the adsorption/activation of key intermediates and the rate-determining step in typical reactions such as CO_2RR, so as to reveal the intrinsic dynamic structure-activity relationship.

(3) Expansion of multi-metal SAA systems

Current SAAs are predominantly constructed as binary systems (e.g., Pt_1Cu, Ir_1Ni), which greatly restricts the tunability of electronic structures and catalytic functions. In contrast, theoretical calculations and simulations have suggested that ternary SAAs systems (e.g., Y_2CuAu, Au_2CuZn) can introduce strong synergistic effects between the two guest metals, enabling the generation and regulation of unique free-atom-like *d*-states that are hardly achievable in binary counterparts. Accordingly, future experimental efforts should focus on: (i) Developing controllable synthetic strategies such as sequential atomic deposition and co-reduction methods, to precisely fabricate ternary SAAs with well-defined atomic configurations and controllable guest-guest distances; (ii) Exploring their catalytic applications in complex multi-intermediate reactions, including CO_2RR toward C_{2+} products and multi-step NH_3 synthesis from nitrogen-containing precursors, where dual guest metal sites can cooperatively adsorb, activate, and tailor multiple key intermediates at the same time, thus boosting catalytic activity, selectivity, and stability.

5.2 Accelerate Technological Translation

(1) Low-cost and scalable synthesis

Laboratory-scale methods (e.g., electrochemical reconstruction, GR) are not suitable for industrial production. Therefore, developing new catalyst synthesis methods is of great significance in SAA preparation. Key directions include: (i) Scaling up green synthesis routes to achieve kilogram scale and even ton-level production of SAAs with uniform dispersion; For example, Ji et al. reported a straightforward and eco-friendly ball milling approach for the fabrication of Co-alloyed Pt (Pt/Co) SAAs at kilogram levels [208]. Pt_1/Co SAA catalysts display excellent stability without aggregation after five consecutive thermal catalytic cycles. More encouragingly, a series of Co-supported noble metal SAA catalysts (M_1/Co, M = Pd, Ru, Ir, and Rh) were successfully synthesized by tuning the acetylacetonate precursors. (ii) The replacement of noble metal catalysts can be achieved by alloying noble metal guest single atoms with non-noble metal hosts or non-noble metal guest single atoms with non-noble metal hosts, thereby effectively reducing the catalyst preparation cost while maintaining stable catalytic performance.

(2) Machine learning (ML)-guided rational design

The current trial-and-error approach, which relies heavily on empirical exploration without systematic guidance, significantly limits the efficient discovery and rational design of high-performance SAAs. This conventional method not only consumes substantial time and resources but also fails to fully exploit the potential synergies between guest atoms, host materials, and catalytic reactions. To address this bottleneck and accelerate the development of advanced SAAs, future work should focus on the following three interrelated aspects: (i) Construct a comprehensive and unified database that integrates multi-dimensional data, including DFT calculation results (e.g., electronic structures, adsorption energies of reaction intermediates, and *d*-band center values), experimental data (e.g., catalytic activity, long-term stability, and structural characterization results), as well as key synthetic parameters (e.g., precursor types, reaction temperature, and post-treatment conditions). This database will serve as a fundamental platform for data-driven catalyst design and mechanism research. (ii) Develop high-precision ML models, such as graph neural networks and deep learning algorithms, to efficiently predict optimal guest-host combinations, *d*-band center positions, and reaction selectivity of SAAs. By leveraging the unified database, these ML models can significantly reduce the catalyst screening cycle from months to weeks, thereby overcoming the inefficiency of the traditional trial-and-error method. (iii) Conduct targeted experimental validation for ML-predicted high-performance SAAs. For instance, if ML models predict that the ternary SAA Y_2CuAu exhibits excellent catalytic performance for CO_2RR to ethanol, systematic experiments should be carried out to verify its catalytic activity, selectivity, and stability, and further clarify the underlying catalytic mechanism, thus forming a closed loop of "prediction-validation-optimization".

5.3 Realize Industrial Commercialization

(1) Integration into practical devices

SAAs need to be further adapted to real-world industrial operating conditions, where they are often exposed to harsh environments such as high current density, long-term continuous operation, and complex electrolytes. This condition readily cause catalyst deactivation and performance decay. To tackle these practical challenges and advance the industrial application of SAAs, future research efforts should focus on two key directions: (i) Developing high-performance SAA-based MEAs specifically tailored for water electrolyzers and fuel cells, with a focus on optimizing catalyst loading to balance cost and performance, as well as improving interface compatibility between SAAs and other components (e.g., electrolyte membranes, gas diffusion layers) to reduce interfacial resistance and enhance overall device efficiency; (ii) Enhancing the long-term durability of SAAs via effective modification strategies, such as

encapsulating SAA particles with protective layers (e.g., N-doped carbon shells) to prevent atomic aggregation and corrosion, or alloying SAAs with corrosion-resistant metals to improve their stability under harsh reaction conditions.

(2) Establishment of industry standards

To promote the widespread industrial adoption of SAAs, the establishment of unified industry standards is critical. Specific efforts should focus on two aspects: (i) Standardizing characterization protocols for SAAs, including the quantification of atomic dispersion via XAS and stability testing under accelerated reaction conditions, to ensure the comparability and reliability of experimental data across different research groups and industrial sectors. (ii) Defining clear performance benchmarks for key catalytic reactions (e.g., CO_2RR, water electrolysis, ammonia synthesis), which will provide a unified evaluation criterion for SAA performance and facilitate their practical application and market promotion.

In summary, SAAs hold enormous potential to revolutionize energy-related electrocatalysis, but their development requires synergistic advances in synthetic chemistry, materials characterization, theoretical modeling, and engineering technology. By addressing the short-term scientific challenges, accelerating mid-term technological translation, and pursuing long-term industrialization, SAAs are expected to become key catalysts for sustainable energy conversion and storage. We anticipate that this review will inspire cross-disciplinary research and guide the rational design of next-generation SAAs toward practical applications.

Data availability

Not applicable."

Acknowledgements

This work was supported by the National Natural Science Foundation of China (22478419), Beijing Municipal Financial Project BJAST Young Scholar Programs B (26CE-YS-01), and Financial Program of BJAST (26CA007-02).

Declaration of competing interest

All the contributing authors report no conflict of interests in this work.

Author contribution statement

X. H. S., J. J. J. and C. M. X. proposed the overall concept. J. S. M., X. H. S. and J. J. J. wrote the paper. X. L. and S. W. G. collected the related information required for the paper. All authors contributed to the general discussion.

Use of AI statement

During the preparation of this work, the authors used Doubao only for language polishing and correction of grammatical errors. After using this tool, the authors reviewed and edited the content as needed and took full responsibility for the content of the publication.

References

[1] Oni, B. A. A review on electrochemical water splitting electrocatalysts for green H_2 production: Unveiling the fundamentals and recent advances. *Langmuir* **2025**, *41*, 10742-10767.

[2] Williams, F.; Yang, A. Substituting fossil fuels in cement production with solar energy to reduce carbon emissions. *Renew. Energy* **2026**, *260*, 125227.

[3] Gao, R.;Wang, J.;Huang, Z.-F.;Zhang, R.;Wang, W.;Pan, L.;Zhang, J.;Zhu, W.;Zhang, X.;Shi, C.;Lim, J.; Zou, J.-J. Pt/Fe_2O_3 with Pt-Fe pair sites as a catalyst for oxygen reduction with ultralow Pt loading. *Nat. Energy* **2021**, *6*, 614-623.

[4] Liu, F.;Shi, C.;Guo, X.;He, Z.;Pan, L.;Huang, Z.-F.;Zhang, X.; Zou, J.-J. Rational design of better hydrogen evolution electrocatalysts for water splitting: A review. *Adv. Sci.* **2022**, *9*, 2200307.

[5] Huanhuan, Z.;Yanping, F.;Shuyan, G.;Wen-Gang, C.;Mingchang, Z.;Zhenglong, L.;Yuhai, D.;Jiarui, Y.;Zechao, Z.;Zhenluo, Y.;Shiqian, Z.;Dingsheng, W.;Baozhong, L.; Hongge, P. Research progress on Ti-based materials for MgH_2 hydrogen storage systems. *Funct. Compos. Mater.* **2025**, *1*, 20250201.

[6] Muhammad, P.;Zada, A.;Rashid, J.;Hanif, S.;Gao, Y.;Li, C.;Li, Y.;Fan, K.; Wang, Y. Defect engineering in nanocatalysts: From design and synthesis to applications. *Adv. Funct. Mater.* **2024**, *34*, 2314686.

[7] Wang, M.;Langer, M.;Altieri, R.;Crisci, M.;Osella, S.; Gatti, T. Two-dimensional layered heterojunctions for photoelectrocatalysis. *ACS Nano* **2024**, *18*, 9245-9284.

[8] Wang, Y.;Ma, F.;Zhang, G.;Zhang, J.;Zhao, H.;Dong, Y.; Wang, D. Precise synthesis of dual atom sites for electrocatalysis. *Nano Res.* **2024**, *17*, 9397-9427.

[9] Quan, L.;Jiang, H.;Mei, G.;Sun, Y.; You, B. Bifunctional electrocatalysts for overall and hybrid water splitting. *Chem. Rev.* **2024**, *124*, 3694-3812.

[10] Jundi, Q.;Xiao, H.;Kanghua, M.; Xiongwu, K. Oxygen coordinated Cu single atom catalysts: a superior catalyst towards electrochemical CO_2 reduction for methane production. *Microstructures* **2025**, *5*, 2025022.

[11] Chen, Z.;Fei, L.;Jia-Jun, W.;Guang-Jin, W.;Zhao-Yong, S.;Qiang, C.;Xiao-Peng, H.;Yi-Da, D.; Wen-Bin, H. Recent research progress of bismuth-based electrocatalysts for electrochemical reduction of carbon dioxide. *Microstructures* **2025**, *5*, 2025016.

[12] Yang, Y.;Zhang, W.;Wu, G.;Huang, Q.;Wen, J.;Wang, D.; Liu, M. Electronic structure tuning in Cu-Co dual single atom catalysts for enhanced COOH* spillover and electrocalytic CO_2 reduction activity. *Angew. Chem. Int. Ed.* **2025**, *64*, e202504423.

[13] Zhang, P.;Wang, L.;Miao, J.;Gan, T.;Zhang, B.;Li, G.;Xu, C.; Sun, X. Iron dual-atom sites for high-efficiency CO_2 electroreduction at industrial-level current density. *J. Catal.* **2026**, *454*, 116617.

[14] Wang, L.;Zhang, B.;Song, Y.;Gan, T.;Miao, J.;Zhang, P.;Jiang, J.;Xu, C.; Sun, X. Fabrication of Fully Exposed Iron Single-Atom Catalyst for Efficient CO_2 Electroreduction Reaction. *Ind. Eng. Chem. Res.* **2025**, *64*, 18114-18123.

[15] Vela, I.;Lázaro, M.; Pérez-Rodríguez, S. Boosting the oxygen reduction electrocatalytic performance of grape stem-derived N-doped activated carbons via (hydro) thermal annealing. *J. Environ. Chem. Eng.* **2026**, *14*, 121363.

[16] Xu, H.;Peng, J.;Li, P.;Feng, X.;Hu, J.;Han, G.;Xu, J.;Wang, D.;Lu, Z.; Li, G. Gradient adsorption energy strategy unlocks ultra‐long stability and efficient electrocatalytic ammonia synthesis from nitrate over CoP/Cu_3P. *Angew. Chem. Int. Ed.* **2026**, *65*, e22410.

[17] Sang, J.-L.;Liu, Q.;Zhang, Y.; Liu, M. Liquid-gas interface confined AgPd nanosheets construct corn-shaped AgPd@Cu nanowires for electrochemical CO_2 reduction to C_2H_4. *Nano Res.* **2026**, *19*, 94908282.

[18] Yang, P.-P.; Gao, M.-R. Enrichment of reactants and intermediates for electrocatalytic CO_2 reduction. *Chem. Soc. Rev.* **2023**, *52*, 4343-4380.

[19] Ahmad, T.;Liu, S.;Sajid, M.;Li, K.;Ali, M.;Liu, L.; Chen, W. Electrochemical CO_2 reduction to C_{2+} products using Cu-based electrocatalysts: A review. *Nano Res. Energy* **2022**, *1*, e9120021.

[20] Verma, J.; Goel, S. Cost-effective electrocatalysts for hydrogen evolution reactions (HER): challenges and prospects. *Int. J. Hydrogen Energy* **2022**, *47*, 38964-38982.

[21] Sun, X.;Wang, L.;Tuo, Y.;Zhang, B.;Gan, T.;Miao, J.; Xu, C. Syngas evolution through CO_2 electroreduction over sulfur-bridged electron deficient cobalt and nickel dual atom catalysts. *Chem. Eng. J.* **2025**, *519*, 165199.

[22] Zhang, P.;Miao, J.;Zhang, B.;Gan, T.;Song, Y.;Li, G.;Jiang, J.;Xu, C.; Sun, X. Tailoring short- and long-range electron transfer of single iron sites for boosted CO_2 electroreduction reaction at low overpotentials. *Chem. Eng. Sci.* **2026**, *320*, 122448.

[23] Chen, T.;Zhang, J.;Zhu, Y.;Song, H.;An, Z.; He, J. Heterogeneous catalytic strategies on the selective oxidation of glycerol into dihydroxyacetone and glyceric acid: a short review of recent research advances. *Chem. Synth.* **2025**, *5*, 80.

[24] Tongyu, T.;Hai, Z.;Hao-Fan, W.;Hongjuan, W.;Yonghai,

C.;Lingyun, Z.; Hao, Y. Sub-2 nm PtBi alloy nanoparticles on Bi-N-C single-atom catalyst for selective oxidation of glycerol to 1,3-dihydroxyacetone. *Chem. Synth.* **2025**, *5*, 28.

[25] Wang, S.;Wang, L.;Zhou, X.;Fang, J.;Deng, C.; Wang, D. Design principles of single-atom catalysts anchored over porous materials for green catalysis and conversion. *Nano Res.* **2025**, *18*, 94907137.

[26] Sun, X.;Zhang, B.;Zhang, P.;Miao, J.; Xu, C. Fabrication of high-loading single atom catalysts for energy-related catalysis. *Small* **2025**, *21*, 2504632.

[27] Xin, H.;Kitchin, J. R.;López, N.;Schweitzer, N. M.;Artrith, N.;Che, F.;Grabow, L. C.;Gunasooriya, G. K. K.;Kulik, H. J.; Laino, T. Roadmap for transforming heterogeneous catalysis with artificial intelligence. *Nat. Catal.* **2026**, *9*, 102-111.

[28] Friend, C. M.; Xu, B. Heterogeneous Catalysis: A Central Science for a Sustainable Future. *Acc. Chem. Res.* **2017**, *50*, 517-521.

[29] Vogt, C.; Weckhuysen, B. M. The concept of active site in heterogeneous catalysis. *Nat. Rev. Chem.* **2022**, *6*, 89-111.

[30] Zaera, F. Designing Sites in Heterogeneous catalysis: Are we reaching selectivities competitive with those of homogeneous catalysts? *Chem. Rev.* **2022**, *122*, 8594-8757.

[31] Haobo, S.;Chuanli, D.;Zeyi, W.;Ying, J.;Iftikhar, H.; Zhengqing, Y. Cathode architecture and active site engineering in lithium-CO_2 batteries. *Microstructures* **2025**, *5*, 2025014.

[32] Shen, J.;Tang, M.;Shi, Z.;Guan, S.;Shi, Y.;Zhuang, Z.;Li, R.;Yang, J.;He, D.;Liu, B.;Dou, Y.; Wang, D. Efficient generation of negative hydrogen with bimetallic-ternary-structured catalysts for Nitrobenzene Hydrogenation. *Angew. Chem. Int. Ed.* **2025**, *64*, e202423626.

[33] Guan, S.;Liu, Y.;Liu, S.;Zhuang, Z.;Shen, R.;Zhang, H.;Liang, E.;Fan, Y.;Jiang, J.;Liu, B.;Wang, Y.;Wang, D.; Li, B. MXene-supported Ru-Ni: A common active site for hydrolysis, hydrogen oxidation, and hydrogenation. *Angew. Chem. Int. Ed.* **2025**, *64*, e202506869.

[34] Yang, H.;Duan, P.;Zhuang, Z.;Luo, Y.;Shen, J.;Xiong, Y.;Liu, X.; Wang, D. Understanding the dynamic evolution of active sites among single atoms, clusters, and nanoparticles. *Adv. Mater.* **2025**, *37*, 2415265.

[35] Ma, R.;Zhang, J.;Gong, J.;Lin, Y.;Zhang, J.;Huang, Z.-Q.;Chang, C.-R.;Liu, S.;Zhu, W.;Wang, Y.;Zeng, K.;Tao, Y.;Hu, J.;Zhang, Z.;Liang, X.;Han, Y.;Mao, J.;Zhuang, Z.;Yan, J.;Wang, D.; Xiong, Y. The cooperative effects of the Rh-M dual-metal atomic pairs in formic acid oxidation. *Angew. Chem. Int. Ed.* **2025**, *64*, e202503095.

[36] Collins, P. The pivotal role of platinum in the discovery of catalysis. *Johnson Matthey Technol. Rev.* **1986**, *30*, 141.

[37] Mittasch, A.; Frankenburger, W. The historical development and theory of ammonia synthesis. *J. Chem. Educ.* **1929**, *6*, 2097.

[38] Zhou, M.;Li, C.; Fang, J. Noble-metal based random alloy and intermetallic nanocrystals: syntheses and applications. *Chem. Rev.* **2021**, *121*, 736-795.

[39] Zhu, J.;Hu, L.;Zhao, P.;Lee, L. Y. S.; Wong, K.-Y. Recent advances in electrocatalytic hydrogen evolution using nanoparticles. *Chem. Rev.* **2020**, *120*, 851-918.

[40] Li, J.; Sun, S. Intermetallic nanoparticles: synthetic control and their enhanced electrocatalysis. *Acc. Chem. Res.* **2019**, *52*, 2015-2025.

[41] Liang, J.;Liu, Q.;Alshehri, A. A.; Sun, X. Recent advances in nanostructured heterogeneous catalysts for N-cycle electrocatalysis. *Nano Res. Energy* **2022**, *1*, 9120010.

[42] Nakaya, Y.; Furukawa, S. Catalysis of alloys: classification, principles, and design for a variety of materials and reactions. *Chem. Rev.* **2023**, *123*, 5859-5947.

[43] Zhi, X.;Jiao, Y.;Zheng, Y.;Vasileff, A.; Qiao, S.-Z. Selectivity roadmap for electrochemical CO_2 reduction on copper-based alloy catalysts. *Nano Energy* **2020**, *71*, 104601.

[44] Liu, W.;Feng, H.;Yang, Y.;Niu, Y.;Wang, L.;Yin, P.;Hong, S.;Zhang, B.;Zhang, X.; Wei, M. Highly-efficient RuNi single-atom alloy catalysts toward chemoselective hydrogenation of nitroarenes. *Nat. Commun.* **2022**, *13*, 3188.

[45] Zhang, L.;Dang, Y.;Zhou, X.;Gao, P.;van Bavel, A. P.;Wang, H.;Li, S.;Shi, L.;Yang, Y.; Vovk, E. I. Direct conversion of CO_2 to a jet fuel over CoFe alloy catalysts. *The Innovation* **2021**, *2*, 100170.

[46] Zhang, Z.;Liu, G.;Cui, X.;Chen, B.;Zhu, Y.;Gong, Y.;Saleem, F.;Xi, S.;Du, Y.;Borgna, A.;Lai, Z.;Zhang, Q.;Li, B.;Zong, Y.;Han, Y.;Gu, L.; Zhang, H. Crystal phase and architecture engineering of lotus-thalamus-shaped Pt-Ni anisotropic superstructures for highly efficient electrochemical hydrogen evolution. *Adv. Mater.* **2018**, *30*, 1801741.

[47] Niu, Z.;Becknell, N.;Yu, Y.;Kim, D.;Chen, C.;Kornienko, N.;Somorjai, G. A.; Yang, P. Anisotropic phase segregation and migration of Pt in nanocrystals en route to nanoframe catalysts. *Nat. Mater.* **2016**, *15*, 1188-1194.

[48] Sun, X.;Zhang, P.;Zhang, B.; Xu, C. Electronic structure regulated carbon‐based single‐atom catalysts for highly efficient and stable electrocatalysis. *Small* **2024**, *20*, 2405624.

[49] Fredersdorff, P. A.;Smyczek, J.;Schröder, C.;Fröhlich, P.;Kohlmorgen, P.;Appelfeller, S.;Neyman, K.; Schauermann, S. Pd/Cu single atom alloys for selective alcohol dehydrogenation: from single crystalline to nanostructured model catalysts. *Angew. Chem. Int. Ed.* **2026**, *65*, e21885.

[50] Cao, S.;Tao, F.;Tang, Y.;Li, Y.; Yu, J. Size- and shape-dependent catalytic performances of oxidation and reduction reactions on nanocatalysts. *Chem. Soc. Rev.* **2016**, *45*, 4747-4765.

[51] Wang, K.; Pera-Titus, M. Microstructured gas-liquid-(solid) interfaces: A platform for sustainable synthesis of commodity chemicals. *Sci. Adv.* **2024**, *10*, eado5448.

[52] Li, T.;Chen, Y.-T.;Zhang, X.-B.;Du, R.-R.;Ma, L.-N.; Lan, Y.-Q. Asymmetric heterogeneous catalysis using crystalline porous materials. *Chem. Soc. Rev.* **2025**, *54*, 5912-5960.

[53] Zhang, Z.;Zhou, M.;Chen, Y.;Liu, S.;Wang, H.;Zhang, J.;Ji, S.;Wang, D.; Li, Y. Pd single-atom monolithic catalyst: Functional 3D structure and unique chemical selectivity in hydrogenation reaction. *Sci. China Mater.* **2021**, *64*, 1919-1929.

[54] Yang, T.;Zhang, H.;Zhan, C.;Liang, L.;Xu, Y.;Ruan, P.;Zhang, Y.;Li, J.;Wang, L.;Lv, X.;Yang, S.;Pao, C.-W.; Huang, X. Strong synergy between single atoms and single-atom alloys enables active and selective H_2O_2 synthesis. *Chem Catal.* **2022**, *2*, 3607-3620.

[55] Sun, X.;Olivos-Suarez, A. I.;Osadchii, D.;Romero, M. J. V.;Kapteijn, F.; Gascon, J. Single cobalt sites in mesoporous N-doped carbon matrix for selective catalytic hydrogenation of nitroarenes. *J. Catal.* **2018**, *357*, 20-28.

[56] Sun, X.;Zhang, P.;Zhang, B.; Xu, C. Electronic structure regulated carbon-based single-atom catalysts for highly efficient and stable electrocatalysis. *Small* **2024**, *20*, 2405624.

[57] Qiao, B.;Wang, A.;Yang, X.;Allard, L. F.;Jiang, Z.;Cui, Y.;Liu, J.;Li, J.; Zhang, T. Single-atom catalysis of CO oxidation using Pt_1/FeO_x. *Nat. Chem.* **2011**, *3*, 634-641.

[58] Ye, H.;Shi, J.;Wu, Y.;Yuan, Y.;Gan, L.;Wu, Y.;Xie, H.;Pugazhendhi, A.; Xia, C. Research progress of nano-catalysts in the catalytic conversion of biomass to biofuels: Synthesis and application. *Fuel* **2024**, *356*, 129594.

[59] Wei, X.;An, M.;Tang, X.;Wei, J.;Yan, P.;Qiu, Y.;Jiang, D.;Asakura, Y.;Song, X.;Asahi, T.;Zhu, C.; Yamauchi, Y. Near-100% site utilization of single atoms for efficient electrocatalysis. *Nat. Commun.* **2026**, *17*, 1013.

[60] Yang, X.;Liu, D.;Zhang, Y.;Fu, C.;Qiu, Z.;Li, Y.;Zhuang, Z.; Yu, B. An alkali-modified biochar-supported single-atom catalyst with enhanced mass transfer for efficient nitrate electrolysis. *Nano Res.* **2026**, *19*, 94908413.

[61] Wang, M.;Zhang, H.;Liu, Y.; Pan, Y. Research progress of precise structural regulation of single atom catalyst for accelerating electrocatalytic oxygen reduction reaction. *J. Energy Chem.* **2022**, *72*, 56-72.

[62] Guo, J.;Zheng, Y.;Hu, Z.;Zheng, C.;Mao, J.;Du, K.;Jaroniec, M.;Qiao, S.-Z.; Ling, T. Direct seawater electrolysis by adjusting the local reaction environment of a catalyst. *Nat. Energy* **2023**, *8*, 264-272.

[63] Liu, J.;Kong, X.;Zheng, L.;Guo, X.;Liu, X.; Shui, J. Rare Earth single-atom catalysts for nitrogen and carbon dioxide reduction. *ACS Nano* **2020**, *14*, 1093-1101.

[64] Yang, Y.;Mao, K.;Gao, S.;Huang, H.;Xia, G.;Lin, Z.;Jiang, P.;Wang, C.;Wang, H.; Chen, Q. O-, N-atoms-coordinated Mn cofactors within a graphene framework as bioinspired oxygen reduction reaction electrocatalysts. *Adv. Mater.* **2018**, *30*, 1801732.

[65] Li, L.;Yuan, K.; Chen, Y. Breaking the scaling relationship limit: from single-atom to dual-atom catalysts. *Acc. Mater. Res.* **2022**, *3*, 584-596.

[66] Li, L.;Chang, X.;Lin, X.;Zhao, Z.-J.; Gong, J. Theoretical insights into single-atom catalysts. *Chem. Soc. Rev.* **2020**, *49*, 8156-8178.

[67] Zhang, W.;Fu, Q.;Luo, Q.;Sheng, L.; Yang, J. Understanding single-atom catalysis in view of theory. *JACS Au* **2021**, *1*, 2130-2145.

[68] Zhang, T.;Walsh, A. G.;Yu, J.; Zhang, P. Single-atom alloy catalysts: structural analysis, electronic properties and catalytic activities. *Chem. Soc. Rev.* **2021**, *50*, 569-588.

[69] Mao, J.;Yin, J.;Pei, J.;Wang, D.; Li, Y. Single atom alloy: An emerging atomic site material for catalytic applications. *Nano*

Today **2020**, *34*, 100917.
[70] Wang, Z.-T.;Darby, M. T.;Therrien, A. J.;El-Soda, M.;Michaelides, A.;Stamatakis, M.; Sykes, E. C. H. Preparation, structure, and surface chemistry of Ni-Au single atom alloys. *J. Phys. Chem C* **2016**, *120*, 13574-13580.
[71] Sun, X.;Song, Y.;Jiang, G.;Lan, X.; Xu, C. Fundamentals and catalytic applications of single-atom alloys. *Sci. China Mater.* **2024**, *67*, 1-17.
[72] Wang, S.;Guo, X.;Zhou, Z.;Cheng, H.; Wang, L. Atomic-precision engineering of single-atom alloy materials for green catalysis and energy conversion. *ACS Mater. Lett.* **2025**, *7*, 1654-1697.
[73] Chen, K.;Xiang, J.;Guo, Y.;Liu, X.;Li, X.; Chu, K. Pd_1Cu single-atom alloys for high-current-density and durable NO-to-NH_3 electroreduction. *Nano Lett.* **2024**, *24*, 541-548.
[74] Wang, F.;Zhao, H.;Zhang, G.;Zhang, H.;Han, X.; Chu, K. Electroreduction of nitrite to ammonia over Ni_1Ru single-atom alloys. *Adv. Funct. Mater.* **2024**, *34*, 2308072.
[75] Greiner, M. T.;Jones, T. E.;Beeg, S.;Zwiener, L.;Scherzer, M.;Girgsdies, F.;Piccinin, S.;Armbrüster, M.;Knop-Gericke, A.; Schlögl, R. Free-atom-like d states in single-atom alloy catalysts. *Nat. Chem.* **2018**, *10*, 1008-1015.
[76] Lucci, F. R.;Liu, J.;Marcinkowski, M. D.;Yang, M.;Allard, L. F.;Flytzani-Stephanopoulos, M.; Sykes, E. C. H. Selective hydrogenation of 1,3-butadiene on platinum-copper alloys at the single-atom limit. *Nat. Commun.* **2015**, *6*, 8550.
[77] Chu, M.;Tu, W.;Zhuang, Z.;Xu, P.;Weng, X.;Wang, J.;Yan, T.;Zhang, L.;Cao, M.;Zhang, L.;Lin, H.;Fan, X.;Zhang, Q.;Wang, D.; Chen, J. Efficient polyolefin upcycling over single-atom alloy catalyst. *CCS Chem.* **2025**, *7*, 2451-2464.
[78] Jiang, W.;Zhang, S. L.;Yang, J.;Hu, S.;Duan, D.;Heng, J. Z. X.;Wang, Z.;Yang, W.;Liu, X.;Yan, Q.;Zhang, M.;Wu, W.-Y.;Hu, J.;Li, J.;Ding, N.;Teo, S. L.;Chan, C. Y.;Lin, M.;Liu, H.;Loh, X. J.;Zhang, Y.-W.;Liu, Z.;Ye, E.;Xiong, Y.; Zhao, M. Phase-regulatable synthesis of single-atom alloy nanocages for efficient alkaline hydrogen evolution. *J. Am. Chem. Soc.* **2025**, *147*, 35293-35303.
[79] Lee, J.;Kumar, A.;Yang, T.;Liu, X.;Jadhav, A. R.;Park, G. H.;Hwang, Y.;Yu, J.;Nguyen, C. T. K.;Liu, Y.;Ajmal, S.;Kim, M. G.; Lee, H. Stabilizing the OOH* intermediate via pre-adsorbed surface oxygen of a single Ru atom-bimetallic alloy for ultralow overpotential oxygen generation. *Energy Environ. Sci.* **2020**, *13*, 5152-5164.
[80] Meng, G.;Sun, J.;Tao, L.;Ji, K.;Wang, P.;Wang, Y.;Sun, X.;Cui, T.;Du, S.;Chen, J.;Wang, D.; Li, Y. Ru_1Con Single-atom alloy for enhancing fischer-tropsch synthesis. *ACS Catal.* **2021**, *11*, 1886-1896.
[81] Jin, C.;Lin, Y.;Wang, Y.;Shi, J.;Li, R.;Liu, Y.;Yue, Z.;Leng, K.;Zhao, Y.;Wang, Y.;Han, X.;Qu, Y.; Bai, J. Engineering atom-scale cascade catalysis via multi-active site collaboration for ampere-level CO_2 electroreduction to C_{2+} products. *Adv. Mater.* **2025**, *37*, 2412658.
[82] Zhao, D.;Qiu, Z.; Lin, C. Challenges and performance optimization strategies of carbon-based transition metal single-atom catalysts derived from ZIF-8 for oxygen reduction reaction: Active site regulation, 3D structural engineering, and interfacial function design. *J. Environ. Chem. Eng.* **2025**, *13*, 119305.
[83] He, C.;Gong, Y.;Li, S.;Wu, J.;Lu, Z.;Li, Q.;Wang, L.;Wu, S.; Zhang, J. Single-atom alloys materials for CO_2 and CH_4 catalytic conversion. *Adv. Mater.* **2024**, *36*, 2311628.
[84] Jin, Z.;Xu, Y.;Chhetri, M.;Wood, J.;Torreon, B.;Che, F.; Yang, M. Recent developments of single atom alloy catalysts for electrocatalytic hydrogenation reactions. *Chem. Eng. J.* **2024**, *491*, 152072.
[85] Pan, Y.;Zhang, X.;Sun, G.;Li, Y.; Liu, B. Single-atom-alloy catalysts for enhanced hydrogenation reaction process: mechanism, regulation strategy, and design principle. *ACS Catal.* **2025**, *15*, 3674-3698.
[86] Zhang, S.;Wang, R.;Zhang, X.; Zhao, H. Recent advances in single-atom alloys: preparation methods and applications in heterogeneous catalysis. *RSC Adv.* **2024**, *14*, 3936-3951.
[87] Kim, S.;Lauterbach, J.; Sasmaz, E. Yolk-shell Pt-NiCe@SiO_2 single-atom-alloy catalysts for low-temperature dry reforming of methane. *ACS Catal.* **2021**, *11*, 8247-8260.
[88] Gao, W.;Liu, S.;Sun, G.;Zhang, C.; Pan, Y. Single‐atom catalysts for hydrogen activation. *Small* **2023**, *19*, 2300956.
[89] Lu, C.;Fang, R.; Chen, X. Single‐atom catalytic materials for advanced battery systems. *Adv. Mater.* **2020**, *32*, 1906548.
[90] Guo, W.;Wang, Z.;Wang, X.; Wu, Y. General design concept for single‐atom catalysts toward heterogeneous catalysis. *Adv. Mater.* **2021**, *33*, 2004287.
[91] Hannagan, R. T.;Giannakakis, G.;Flytzani-Stephanopoulos, M.; Sykes, E. C. H. Single-atom alloy catalysis. *Chem. Rev.* **2020**, *120*, 12044-12088.
[92] Sarma, B. B.;Maurer, F.;Doronkin, D. E.; Grunwaldt, J.-D. Design of single-atom catalysts and tracking their fate using operando and advanced X-ray spectroscopic tools. *Chem. Rev.* **2022**, *123*, 379-444.
[93] Li, P.;Yang, F.;Li, J.;Zhu, Q.;Xu, J. W.;Loh, X. J.;Huang, K. W.;Hu, W.; Lu, J. Nanoscale engineering of P‐block metal‐based catalysts toward industrial‐scale electrochemical reduction of CO_2. *Adv. Energy Mater.* **2023**, *13*, 2301597.
[94] Zou, S.;Liang, Y.;Zhang, X.;Gu, Q.;Wang, L.;Sun, H.;Liao, X.;Huang, J.; Masri, A. R. Manufacturing single-atom alloy catalysts for selective CO_2 hydrogenation via refinement of isolated-alloy-islands. *Angew. Chem. Int. Ed.* **2025**, *64*, e202412835.
[95] Huang, J.;Gao, C.;Liu, S.;Du, X.;Zhou, W.; Wang, C. CuPd/Al_2O_3 single atom alloy catalyst facilitates the catalytic transfer hydrodeoxygenation of furfural to 2-methylfuran. *Chem. Eng. J.* **2025**, *504*, 158731.
[96] Bai, P.;Chen, J.;Zhao, Y.; Li, Y. Pt_1In single atom alloy for visible-light-driven CO_2 formylation of benzylamine. *Nano Energy* **2025**, *135*, 110673.
[97] Hu, Y.;Shen, T.;Song, Z.;Wu, Z.;Bai, S.;Liu, G.;Sun, X.;Wang, Y.;Hu, S.;Zheng, L.; Song, Y.-F. Atomic modulation of single dispersed Ir species on self-supported NiFe layered double hydroxides for efficient electrocatalytic overall water splitting. *ACS Catal.* **2023**, *13*, 11195-11203.
[98] Shen, T.;Wang, S.;Zhao, T.;Hu, Y.; Wang, D. Recent advances of single‐atom‐alloy for energy electrocatalysis. *Adv. Energy Mater.* **2022**, *12*, 2201823.
[99] Wang, T.;Chutia, A.;Brett, D. J.;Shearing, P. R.;He, G.;Chai, G.; Parkin, I. P. Palladium alloys used as electrocatalysts for the oxygen reduction reaction. *Energy Environ. Sci.* **2021**, *14*, 2639-2669.
[100] Kong, X.;Wu, H.;Lu, K.;Zhang, X.;Zhu, Y.; Lei, H. Galvanic replacement reaction: Enabling the creation of active catalytic structures. *ACS Appl. Mater. Interfaces* **2023**, *15*, 41205-41223.
[101] Sun, G.;Zhao, Z.-J.;Mu, R.;Zha, S.;Li, L.;Chen, S.;Zang, K.;Luo, J.;Li, Z.;Purdy, S. C.;Kropf, A. J.;Miller, J. T.;Zeng, L.; Gong, J. Breaking the scaling relationship via thermally stable Pt/Cu single atom alloys for catalytic dehydrogenation. *Nat. Commun.* **2018**, *9*, 4454.
[102] Molina, D. L.;Inagaki, M.;Kazuma, E.;Kim, Y.; Trenary, M. Probing the properties of Pt-Cu(111) bimetallic surfaces with adsorbed CO. *J. Phys. Chem C* **2023**, *127*, 9796-9806.
[103] Oda, A.;Ichihashi, K.;Yamamoto, Y.;Ohtsu, T.;Shi, W.;Sawabe, K.; Satsuma, A. Pt single atom alloyed sub-1 nm thick Fe overlayer on supported Cu nanoparticles for methylcyclohexane dehydrogenation. *J. Mater. Chem. A* **2024**, *12*, 22655-22667.
[104] Mohammadpour, A.; Kaya, S. Step-edge decoration and clustering of Pt atoms on a Cu(211) stepped surface. *J. Phys. Chem C* **2024**, *128*, 5480-5489.
[105] Li, S.;Xu, B.;Yang, H.;Zhang, C.;Chen, J.;Liu, S.;Huang, Z.; Liu, H. A Pt_1Pd single-atom alloy nanozyme with boosted enzyme-like activity for efficient photo-mediated tumor therapy. *Small* **2024**, *20*, 2309704.
[106] Oda, A.;Ogawa, N.;Yamamoto, Y.;Sawabe, K.; Satsuma, A. Atom-to-nm scale engineering of PtCo alloy catalysts over supported Co nanoparticles for advanced toluene hydrogenation efficiency in hydrogen storage applications. *ACS Catal.* **2025**, *15*, 3191-3202.
[107] Lan, J.;Wei, Z.;Lu, Y.-R.;Chen, D.;Zhao, S.;Chan, T.-S.; Tan, Y. Efficient electrosynthesis of formamide from carbon monoxide and nitrite on a Ru-dispersed Cu nanocluster catalyst. *Nat. Commun.* **2023**, *14*, 2870.
[108] Zhang, Y.;Chen, X.;Wang, W.;Yin, L.; Crittenden, J. C. Electrocatalytic nitrate reduction to ammonia on defective Au_1Cu (111) single-atom alloys. *Appl. Catal. B: Environ.* **2022**, *310*, 121346.
[109] Wang, B.;Li, J.;Li, D.;Xu, J.;Liu, S.;Jiang, Q.;Zhang, Y.;Duan, Z.; Zhang, F. Single atom Iridium decorated Nickel alloys supported on segregated MoO_2 for alkaline water electrolysis. *Adv. Mater.* **2024**, *36*, 2305437.
[110] De Gregorio, G. L.;Burdyny, T.;Loiudice, A.;Iyengar, P.;Smith, W. A.; Buonsanti, R. Facet-dependent selectivity of Cu catalysts in electrochemical CO_2 reduction at commercially viable current densities. *ACS Catal.* **2020**, *10*, 4854-4862.
[111] Chen, T.;Tan, Z.;Xu, H.;Zhang, J.;Chen, L.;Huang, Z.; Pang, H.

Electrochemical reconstruction of defect engineered MOFs: A dynamic frontier in electrochemistry. *Adv. Funct. Mater.* **2026**, *36*, e17710.

[112] Liu, X.;Ao, C.;Shen, X.;Wang, L.;Wang, S.;Cao, L.;Zhang, W.;Dong, J.;Bao, J.; Ding, T. Dynamic surface reconstruction of single-atom bimetallic alloy under operando electrochemical conditions. *Nano Lett.* **2020**, *20*, 8319-8325.

[113] Gao, Q.;Han, X.;Liu, Y.; Zhu, H. Electrifying energy and chemical transformations with single-atom alloy nanoparticle catalysts. *ACS Catal.* **2024**, *14*, 6045-6061.

[114] Chen, Y.;Tan, Z.;Wang, E.;Yin, J.;Luo, L.;Shen, S.; Zhang, J. Progress and prospects of dealloying methods for energy-conversion electrocatalysis. *Dalton Transactions* **2023**, *52*, 7370-7382.

[115] Cao, Y.;Chen, S.;Bo, S.;Fan, W.;Li, J.;Jia, C.;Zhou, Z.;Liu, Q.;Zheng, L.; Zhang, F. Single atom Bi decorated copper alloy enables C−C coupling for electrocatalytic reduction of CO_2 into C_{2+} products. *Angew. Chem. Int. Ed.* **2023**, *62*, e202303048.

[116] Zheng, T.;Liu, C.;Guo, C.;Zhang, M.;Li, X.;Jiang, Q.;Xue, W.;Li, H.;Li, A.;Pao, C.-W.;Xiao, J.;Xia, C.; Zeng, J. Copper-catalysed exclusive CO_2 to pure formic acid conversion via single-atom alloying. *Nat. Nanotechnol.* **2021**, *16*, 1386-1393.

[117] Fang, C.;Huang, L.;Gao, W.;Jiang, X.;Liu, H.;Hu, R.;Li, X.;Yu, J.; Zhou, W. Oxygen-pinned Ag_1In single-atom alloy for efficient electroreduction CO_2 to formate. *Adv. Energy Mater.* **2024**, *14*, 2400813.

[118] Zhao, Y.;Liu, X.;Chen, D.;Liu, Z.;Yang, Q.;Lin, X.;Peng, M.;Liu, P.; Tan, Y. Atomic-level-designed copper atoms on hierarchically porous gold architectures for high-efficiency electrochemical CO_2 reduction. *Sci. China Mater.* **2021**, *64*, 1900-1909.

[119] Wang, M.;Fang, M.;Liu, Y.;Chen, C.;Zhang, Y.;Jia, S.;Wu, H.;He, M.; Han, B. Enhanced intermediates Inter-migration on Ag single-atom alloys for boosting multicarbon product selectivity in CO_2 electroreduction. *J. Am. Chem. Soc.* **2025**, *147*, 16450-16458.

[120] Kim, J. H.;Sa, Y. J.;Lim, T.;Woo, J.; Joo, S. H. Steering catalytic selectivity with atomically dispersed metal electrocatalysts for renewable energy conversion and commodity chemical production. *Acc. Chem. Res.* **2022**, *55*, 2672-2684.

[121] Zhang, Q.; Guan, J. Single-atom catalysts for electrocatalytic applications. *Adv. Funct. Mater.* **2020**, *30*, 2000768.

[122] Darby, M. T.;Réocreux, R.;Sykes, E. C. H.;Michaelides, A.; Stamatakis, M. Elucidating the stability and reactivity of surface intermediates on single-atom alloy catalysts. *ACS Catal.* **2018**, *8*, 5038-5050.

[123] Xu, T.;Li, P.;Deng, W.;Liu, X.;Sun, Q.; Bai, S. Atomic ordering engineering of precious metal alloys in liquid phase synthesis. *Nano Lett.* **2024**, *24*, 2328-2336.

[124] Yu, J.;Gao, R.-T.;Guo, X.;Truong Nguyen, N.;Wu, L.; Wang, L. Electrochemical nitrate reduction to ammonia on AuCu single-atom alloy aerogels under wide potential window. *Angew. Chem. Int. Ed.* **2025**, *64*, e202415975.

[125] Pan, Y.;Qian, Y.;Zheng, X.;Chu, S.-Q.;Yang, Y.;Ding, C.;Wang, X.;Yu, S.-H.; Jiang, H.-L. Precise fabrication of single-atom alloy co-catalyst with optimal charge state for enhanced photocatalysis. *Natl. Sci. Rev.* **2020**, *8*, nwaa224.

[126] Ren, W.;Tan, X.;Qu, J.;Li, S.;Li, J.;Liu, X.;Ringer, S. P.;Cairney, J. M.;Wang, K.;Smith, S. C.; Zhao, C. Isolated copper-tin atomic interfaces tuning electrocatalytic CO_2 conversion. *Nat. Commun.* **2021**, *12*, 1449.

[127] Zhao, Y.;Zhang, L.;Liu, J.;Adair, K.;Zhao, F.;Sun, Y.;Wu, T.;Bi, X.;Amine, K.;Lu, J.; Sun, X. Atomic/molecular layer deposition for energy storage and conversion. *Chem. Soc. Rev.* **2021**, *50*, 3889-3956.

[128] Zhou, L.;Lu, S.-Y.; Guo, S. Recent progress on precious metal single atom materials for water splitting catalysis. *SusMat* **2021**, *1*, 194-210.

[129] Yao, Y.;Wang, S.;Li, Z.; Wu, Y. Atomic level engineering of noble metal nanocrystals for energy conversion catalysis. *J. Energy Chem.* **2021**, *63*, 604-624.

[130] Zhong, M.;Zhao, J.;Fang, Y.;Wu, D.;Zhang, L.;Du, C.;Liu, S.;Yang, S.;Wan, S.;Jiang, Y.;Huang, J.; Xiong, H. Depositing Pd on the outmost surface of Pd_1Ni/SiO_2 single-atom alloy via atomic layer deposition for selective hydrogenation of acetylene. *Applied Catalysis A: General* **2023**, *662*, 119288.

[131] Fonseca, J.; Lu, J. Single-atom catalysts designed and prepared by the atomic layer deposition technique. *ACS Catal.* **2021**, *11*, 7018-7059.

[132] Zhang, L.;Liu, H.;Liu, S.;Norouzi Banis, M.;Song, Z.;Li, J.;Yang, L.;Markiewicz, M.;Zhao, Y.;Li, R.;Zheng, M.;Ye, S.;Zhao, Z.-J.;Botton, G. A.; Sun, X. Pt/Pd single-atom alloys as highly active electrochemical catalysts and the origin of enhanced activity. *ACS Catal.* **2019**, *9*, 9350-9358.

[133] Wang, H.;Luo, Q.;Liu, W.;Lin, Y.;Guan, Q.;Zheng, X.;Pan, H.;Zhu, J.;Sun, Z.;Wei, S.;Yang, J.; Lu, J. Quasi Pd_1Ni single-atom surface alloy catalyst enables hydrogenation of nitriles to secondary amines. *Nat. Commun.* **2019**, *10*, 4998.

[134] Wu, W.;Qu, W.;Wang, Z.;Tan, Y.;Chen, R.;Chen, S.;Lv, H.;Zhong, J.; Cheng, N. Single-atom Al precisely modulate the strain of Pt_3Co intermetallic for superior oxygen catalytic performance. *Chem. Eng. J.* **2024**, *491*, 151987.

[135] Luo, F.;Zhu, J.;Ma, S.;Li, M.;Xu, R.;Zhang, Q.;Yang, Z.;Qu, K.;Cai, W.; Chen, Z. Regulated coordination environment of Ni single atom catalyst toward high-efficiency oxygen electrocatalysis for rechargeable Zinc-air batteries. *Energy Storage Mater.* **2021**, *35*, 723-730.

[136] Rosen, A. S.;Vijay, S.; Persson, K. A. Free-atom-like d states beyond the dilute limit of single-atom alloys. *Chem. Sci.* **2023**, *14*, 1503-1511.

[137] Spivey, T. D.; Holewinski, A. Selective interactions between free-atom-like d-states in single-atom alloy catalysts and near-frontier molecular orbitals. *J. Am. Chem. Soc.* **2021**, *143*, 11897-11902.

[138] Zhang, J.;Yang, H. B.;Zhou, D.; Liu, B. Adsorption energy in oxygen electrocatalysis. *Chem. Rev.* **2022**, *122*, 17028-17072.

[139] Nørskov, J. K.;Bligaard, T.;Hvolbæk, B.;Abild-Pedersen, F.;Chorkendorff, I.; Christensen, C. H. The nature of the active site in heterogeneous metal catalysis. *Chem. Soc. Rev.* **2008**, *37*, 2163-2171.

[140] Gerber, I. C.; Serp, P. A Theory/experience description of support effects in carbon-supported catalysts. *Chem. Rev.* **2020**, *120*, 1250-1349.

[141] Li, B.;Wang, H.;Shen, Y.;Zhang, Z.;Xiong, Y.;Wang, M.;Li, W.;Zhou, W.; He, J. Selective adsorption-catalysis sites of lithium polysulfides induced by the competition between spin polarization and electronegativity in high-entropy alloy electrocatalysts. *ACS nano* **2025**, *19*, 12021-12032.

[142] Panjwani, M. K.;Liu, Y.;Han, S.;Khan, D.;Yang, S.;Xiao, F.; Gao, P. Breaking scaling relationship limitations in peroxymonosulfate activation through electronegativity-driven Fe-Mn dual-metal synergy. *Nanoscale* **2025**, *17*, 17676-17688.

[143] Chen, W.;Qian, G.;Wang, H.;Chen, D.;Zhou, X.;Yuan, W.; Duan, X. Rationalizing the d-band model from theory to practice in catalyst design. *J. Am. Chem. Soc.* **2025**, *147*, 46729-46744.

[144] Chen, K.;Ma, Z.;Li, X.;Kang, J.;Ma, D.; Chu, K. Single-atom Bi alloyed Pd metallene for nitrate electroreduction to ammonia. *Adv. Funct. Mater.* **2023**, *33*, 2209890.

[145] Liu, S.;Wu, D.;Yang, F.;Chen, K.;Luo, Z.;Li, J.;Zhang, Z.;Zhao, J.;Zhang, L.;Zhang, Y.;Zhang, H.;Wan, S.;Peng, Y.-k.;Zhang, K. H. L.; Xiong, H. Atomic intimacy in Pd_1Ni/SiO_2 single-atom alloy prepared by galvanic replacement for enhanced semi-hydrogenation of acetylene. *Chem. Eng. J.* **2024**, *481*, 148658.

[146] Ren, H.;Yu, W.;Lv, M.;Gao, J.;Hu, H.;Wang, M.;Cui, X.;Liu, J.; Jiang, L. Carbon-encapsulated single-atom platinum nickel alloy for efficient and durable alkaline hydrogen oxidation through enhanced charge polarization. *Adv. Funct. Mater.* **2025**, *35*, 2413754.

[147] Chen, H.;Wu, Q.;Wang, Y.;Zhao, Q.;Ai, X.;Shen, Y.; Zou, X. d-sp orbital hybridization: a strategy for activity improvement of transition metal catalysts. *Chem. Commun.* **2022**, *58*, 7730-7740.

[148] Wang, F.;Shang, S.;Sun, Z.;Yang, X.; Chu, K. P-Block antimony-copper single-atom alloys for selective nitrite electroreduction to ammonia. *ACS Nano* **2024**, *18*, 13141-13149.

[149] Zhang, M.;Li, H.;Ma, F.-X.;Zhen, L.;Du, Y.; Xu, C.-Y. IrCo single-atom alloy catalysts with optimized d-band center for advanced alkali-Al/acid hybrid fuel cell. *Chem. Eng. J.* **2023**, *471*, 144187.

[150] Chen, Z.;Wu, R.;Liu, Y.;Ha, Y.;Guo, Y.;Sun, D.;Liu, M.; Fang, F. Ultrafine Co nanoparticles encapsulated in carbon-nanotubes-grafted graphene sheets as advanced electrocatalysts for the hydrogen evolution reaction. *Adv. Mater.* **2018**, *30*, 1802011.

[151] Li, Z.;Feng, Y.;Liang, Y.-L.;Cheng, C.-Q.;Dong, C.-K.;Liu, H.; Du, X.-W. Stable rhodium (IV) oxide for alkaline hydrogen evolution reaction. *Adv. Mater.* **2020**, *32*, 1908521.

[152] Pan, J.;Yu, S.;Jing, Z.;Zhou, Q.;Dong, Y.;Lou, X.; Xia, F. Electrocatalytic hydrogen evolution reaction related to nanochannel materials. *Small Struct.* **2021**, *2*, 2100076.

[153] Gao, H.;Jiang, Y.;Chen, R.;Dong, C.-L.;Huang, Y.-C.;Ma, M.;Shi, Z.;Liu, J.;Zhang, Z.;Qiu, M.;Wu, T.;Wang, J.;Jiang, Y.;Chen, J.;An, X.;He, Y.; Wang, S. Alloyed Pt single-atom catalysts for durable PEM water electrolyzer. *Adv. Funct. Mater.* **2023**, *33*, 2214795.

[154] Luo, M.;Cai, J.;Zou, J.;Jiang, Z.;Wang, G.; Kang, X. Promoted alkaline hydrogen evolution by an N-doped Pt-Ru single atom alloy. *J. Mater. Chem. A* **2021**, *9*, 14941-14947.

[155] Yuan, H.;Jiang, D.;Li, Z.;Liu, X.;Tang, Z.;Zhang, X.;Zhao, L.;Huang, M.;Liu, H.;Song, K.; Zhou, W. Laser synthesis of PtMo single-atom alloy electrode for ultralow voltage hydrogen generation. *Adv. Mater.* **2024**, *36*, 2305375.

[156] Tong, Y.;Liu, J.;Wang, L.;Su, B.-J.;Wu, K.-H.;Juang, J.-Y.;Hou, F.;Yin, L.;Dou, S. X.;Liu, J.; Liang, J. Carbon-shielded single-Atom alloy material family for multi-functional electrocatalysis. *Adv. Funct. Mater.* **2022**, *32*, 2205654.

[157] Yang, S.;Si, Z.;Li, G.;Zhan, P.;Liu, C.;Lu, L.;Han, B.;Xie, H.; Qin, P. Single cobalt atoms immobilized on palladium-based nanosheets as 2D single-atom alloy for efficient hydrogen evolution reaction. *Small* **2023**, *19*, 2207651.

[158] Chong, L.;Wen, J.;Song, E.;Yang, Z.;Bloom, I. D.; Ding, W. Synergistic Co-Ir/Ru composite electrocatalysts impart efficient and durable oxygen evolution catalysis in acid. *Adv. Energy Mater.* **2023**, *13*, 2302306.

[159] Wang, K.;Wang, Y.;Yang, B.;Li, Z.;Qin, X.;Zhang, Q.;Lei, L.;Qiu, M.;Wu, G.; Hou, Y. Highly active ruthenium sites stabilized by modulating electron-feeding for sustainable acidic oxygen-evolution electrocatalysis. *Energy Environ. Sci.* **2022**, *15*, 2356-2365.

[160] Luo, F.;Hu, H.;Zhao, X.;Yang, Z.;Zhang, Q.;Xu, J.;Kaneko, T.;Yoshida, Y.;Zhu, C.; Cai, W. Robust and stable acidic overall water splitting on Ir single atoms. *Nano Lett.* **2020**, *20*, 2120-2128.

[161] Reier, T.;Nong, H. N.;Teschner, D.;Schlögl, R.; Strasser, P. Electrocatalytic oxygen evolution reaction in acidic environments - reaction mechanisms and catalysts. *Adv. Energy Mater.* **2017**, *7*, 1601275.

[162] Yang, Z.;Ding, Y.;Chen, W.;Luo, S.;Cao, D.;Long, X.;Xie, L.;Zhou, X.;Cai, X.;Liu, K.;Fu, X.-Z.; Luo, J.-L. Phase-engineered Bi-RuO_2 single-atom alloy oxide boosting oxygen evolution electrocatalysis in proton exchange membrane water electrolyzer. *Adv. Mater.* **2025**, *37*, 2417777.

[163] Long, X.;Zhao, B.;Zhao, Q.;Wu, X.;Zhu, M.-N.;Feng, R.;Shakouri, M.;Zhang, Y.;Xiao, X.;Zhang, J.;Fu, X.-Z.; Luo, J.-L. Ru-RuO_2 nano-heterostructures stabilized by the sacrificing oxidation strategy of Mn_3O_4 substrate for boosting acidic oxygen evolution reaction. *Appl. Catal. B: Environ.* **2024**, *343*, 123559.

[164] Li, P.;Xie, Q.;Zheng, L.;Feng, G.;Li, Y.;Cai, Z.;Bi, Y.;Li, Y.;Kuang, Y.;Sun, X.; Duan, X. Topotactic reduction of layered double hydroxides for atomically thick two-dimensional non-noble-metal alloy. *Nano Res.* **2017**, *10*, 2988-2997.

[165] Xu, B.-B.;Fu, X.-B.;You, X.-M.;Zhao, E.;Li, F.-F.;Chen, Z.;Li, Y.-X.;Wang, X. L.; Yao, Y.-F. Synergistic promotion of single-atom Co surrounding a PtCo alloy based On a g-C_3N_4 nanosheet for overall water splitting. *ACS Catal.* **2022**, *12*, 6958-6967.

[166] Chae, K.;Lee, H.;Huang, W.-T.;Son, J.;Pavageau, B.;Kim, T.-H.;Lee, S.-e.;Kim, J.;Moon, J.;Liu, R.-S.;Bang, J.; Kim, D. H. Spin-polarized acidic water electrolysis with antenna-reactor plasmonic electrocatalysts. *Adv. Mater.* **2025,** *37*, 2507658.

[167] Lu, X.;Xia, B. Y.;Zang, S.; Lou, X. W. D. Metal-organic frameworks based electrocatalysts for the oxygen reduction reaction. *Angew. Chem. Int. Ed.* **2019**, *59*, 4634-4650.

[168] Li, J.;Yin, H.-M.;Li, X.-B.;Okunishi, E.;Shen, Y.-L.;He, J.;Tang, Z.-K.;Wang, W.-X.;Yücelen, E.;Li, C.;Gong, Y.;Gu, L.;Miao, S.;Liu, L.-M.;Luo, J.; Ding, Y. Surface evolution of a Pt-Pd-Au electrocatalyst for stable oxygen reduction. *Nat. Energy* **2017**, *2*, 17111.

[169] Kelly, S. R.;Kirk, C.;Chan, K.; Nørskov, J. K. Electric field effects in oxygen reduction kinetics: Rationalizing pH dependence at the Pt(111), Au(111), and Au(100) electrodes. *J. Phys. Chem C* **2020**, *124*, 14581-14591.

[170] Luo, S.;Xie, L.;Cai, X.;Chen, W.;Wu, J.;Ding, Y.;Zhou, Y.;Quan, Z.;Feng, R.;Fu, X.-Z.; Luo, J.-L. Golden single-atom alloys selectively boosting oxygen reduction and methanol oxidation. *Adv. Mater.* **2025**, *37*, 2500848.

[171] Qiu, Y.;Sun, M.;Wu, J.;Chai, C.;Wang, S.;Huang, H.;Zhao, X.;Jiao, D.;Xu, S.;Wang, D.;Ge, X.;Zhang, W.;Zheng, W.;Song, Y.;Fan, J.;Huang, B.; Cui, X. Boosting oxygen reduction performances in Pd-based metallenes by co-confining interstitial H and p-block single atoms. *Nat. Commun.* **2025**, *16*, 5262.

[172] Balamurugan, C.;Kim, Y. Y.;Jo, Y.-R.;Cho, K.;Park, B.;Kim, W.;Lim, N.;Pak, Y.;Kim, H.;Lee, H.;Chae, K. H.;Shim, J. H.;Lee, C.; Kwon, S. In-situ probing polarization-induced stability of single-atom alloy electrocatalysts in metal-air battery via synchrotron-based X-ray diffraction. *Appl. Catal. B: Environ. Energy* **2024**, *353*, 124072.

[173] Cheng, X.;Wang, Y.;Lu, Y.;Zheng, L.;Sun, S.;Li, H.;Chen, G.; Zhang, J. Single-atom alloy with Pt-Co dual sites as an efficient electrocatalyst for oxygen reduction reaction. *Appl. Catal. B: Environ.* **2022**, *306*, 121112.

[174] Niu, X.;Wei, J.;Xu, D.;Pei, J.; Sui, R. Charge-asymmetry Fe_1Cu single-atom alloy catalyst for efficient oxygen reduction reaction. *Nano Res.* **2024**, *17*, 4702-4710.

[175] Jiang, J.-C.;Chen, J.-C.;Zhao, M.-d.;Yu, Q.;Wang, Y.-G.; Li, J. Rational design of copper-based single-atom alloy catalysts for electrochemical CO_2 reduction. *Nano Res.* **2022**, *15*, 7116-7123.

[176] Tuo, Y.;Liu, W.;Lu, Q.;Wang, X.;Luo, J.;Wang, S.;Zhou, Y.;Wang, M.;Sun, X.;Feng, X.;Wu, M.;Chen, D.; Zhang, J. SO_4^{2-} mediated CO_2 activation on metal electrode for efficient CO_2 electroreduction. *Chem. Eng. J.* **2023**, *464*, 142510.

[177] Dai, M.;Ni, W.;Zeng, Z.;Zhang, W.;Zhang, Y.;Wang, S.; Zhang, S. Inert is not inactive: origin of carbon dioxide electroreduction activity over a carbon current collector-based electrode. *Energy Environ. Sci.* **2024**, *17*, 1531-1539.

[178] Sun, Q.;Jia, C.;Lu, H.;Yang, M.;Liu, R.;Villamanca, D. M.;Zhao, Y.; Zhao, C. Ampere-level electroreduction of CO_2 and CO. *Chem. Soc. Rev.* **2025**, *54*, 6973-7016.

[179] Zhang, B.;Zhang, B.;Jiang, Y.;Ma, T.;Pan, H.; Sun, W. Single‐atom electrocatalysts for multi‐electron reduction of CO_2. *Small* **2021**, *17*, 2101443.

[180] Li, J.;Zeng, H.;Dong, X.;Ding, Y.;Hu, S.;Zhang, R.;Dai, Y.;Cui, P.;Xiao, Z.;Zhao, D.;Zhou, L.;Zheng, T.;Xiao, J.;Zeng, J.; Xia, C. Selective CO_2 electrolysis to CO using isolated antimony alloyed copper. *Nat. Commun.* **2023**, *14*, 340.

[181] Nitopi, S.;Bertheussen, E.;Scott, S. B.;Liu, X.;Engstfeld, A. K.;Horch, S.;Seger, B.;Stephens, I. E. L.;Chan, K.;Hahn, C.;Nørskov, J. K.;Jaramillo, T. F.; Chorkendorff, I. Progress and perspectives of electrochemical CO_2 reduction on copper in aqueous electrolyte. *Chem. Rev.* **2019**, *119*, 7610-7672.

[182] Lee, C. W.;Yang, K. D.;Nam, D.-H.;Jang, J. H.;Cho, N. H.;Im, S. W.; Nam, K. T. Defining a materials database for the design of copper binary alloy catalysts for electrochemical CO_2 conversion. *Adv. Mater.* **2018**, *30*, 1704717.

[183] Peterson, A. A.;Abild-Pedersen, F.;Studt, F.;Rossmeisl, J.; Nørskov, J. K. How copper catalyzes the electroreduction of carbon dioxide into hydrocarbon fuels. *Energy Environ. Sci.* **2010**, *3*, 1311-1315.

[184] Garza, A. J.;Bell, A. T.; Head-Gordon, M. Mechanism of CO_2 reduction at copper surfaces: pathways to C_2 products. *ACS Catal.* **2018**, *8*, 1490-1499.

[185] Xiao, Y.;Yu, F.;Xia, C.;Zhu, D.;Chen, J.;Liu, N.;Zhao, Y.;Qi, R.;Guo, W.;You, B.;Yao, T.;Pang, Y.;Wang, Z.;Wang, H.;Song, F.; Xia, B. Y. Asymmetric CO-CHO coupling over Pr single-atom alloy enables industrial-level electrosynthesis of ethylene. *J. Am. Chem. Soc.* **2025**, *147*, 15654-15665.

[186] Wang, S.;Li, F.;Zhao, J.;Zeng, Y.;Li, Y.;Lin, Z.-Y.;Lee, T.-J.;Liu, S.;Ren, X.;Wang, W.;Chen, Y.;Hung, S.-F.;Lu, Y.-R.;Cui, Y.;Yang, X.;Li, X.;Huang, Y.; Liu, B. Manipulating C-C coupling pathway in electrochemical CO_2 reduction for selective ethylene and ethanol production over single-atom alloy catalyst. *Nat. Commun.* **2024**, *15*, 10247.

[187] Qing, G.;Ghazfar, R.;Jackowski, S. T.;Habibzadeh, F.;Ashtiani, M. M.;Chen, C.-P.;Smith, M. R., III; Hamann, T. W. Recent advances and challenges of electrocatalytic N_2 reduction to ammonia. *Chem. Rev.* **2020**, *120*, 5437-5516.

[188] Li, Y.;Wang, H.;Priest, C.;Li, S.;Xu, P.; Wu, G. Advanced electrocatalysis for energy and environmental sustainability via water and nitrogen reactions. *Adv. Mater.* **2021**, *33*, 2000381.

[189] Sun, X.;Zhang, B.;Lu, Q.;Jiang, J.;Ye, C.;Cui, G.;Zhuang, Z.;Zhang, J.;Bitter, J. H.;Li, G.; Xu, C. Tailoring the proximity of iron and manganese atomic sites for efficient CO_2 electroreduction reaction. *Nano Res.* **2025**, *18*, 94907249.

[190] Xiang, J.;Zhao, H.;Chen, K.;Yang, X.; Chu, K. Electrocatalytic nitrite reduction to ammonia on an Rh single-atom catalyst. *J. Colloid Interface Sci.* **2024**, *659*, 432-438.

[191] Song, W.;Yue, L.;Fan, X.;Luo, Y.;Ying, B.;Sun, S.;Zheng, D.;Liu, Q.;Hamdy, M. S.; Sun, X. Recent progress and strategies on the design of catalysts for electrochemical ammonia synthesis from nitrate reduction. *Inorg. Chem. Front.* **2023**, *10*, 3489-3514.

[192] Shao, J.;Jing, H.;Wei, P.;Fu, X.;Pang, L.;Song, Y.;Ye, K.;Li, M.;Jiang, L.;Ma, J.;Li, R.;Si, R.;Peng, Z.;Wang, G.; Xiao, J. Electrochemical synthesis of ammonia from nitric oxide using a copper-tin alloy catalyst. *Nat. Energy* **2023**, *8*, 1273-1283.

[193] Yu, Y.;Wei, X.;Chen, W.;Qian, G.;Chen, C.;Wang, S.; Min, D. Design of single‐atom catalysts for electrocatalytic nitrogen

fixation. *ChemSusChem* **2024**, *17*, e202301105.
[194] Li, X.;Shen, P.;Luo, Y.;Li, Y.;Guo, Y.;Zhang, H.; Chu, K. PdFe single-atom alloy metallene for N_2 electroreduction. *Angew. Chem. Int. Ed.* **2022**, *61*, e202205923.
[195] Long, J.;Chen, S.;Zhang, Y.;Guo, C.;Fu, X.;Deng, D.; Xiao, J. Direct electrochemical ammonia synthesis from nitric oxide. *Angew. Chem. Int. Ed.* **2020**, *59*, 9711-9718.
[196] Han, G.-F.;Shi, X.-M.;Kim, S.-J.;Kim, J.;Jeon, J.-P.;Noh, H.-J.;Im, Y.-K.;Li, F.;Uhm, Y. R.;Kim, C. S.;Jiang, Q.; Baek, J.-B. Dissociating stable nitrogen molecules under mild conditions by cyclic strain engineering. *Sci. Adv.* **2019**, *5*, eaax8275.
[197] Zhao, Y.;Shi, R.;Bian, X.;Zhou, C.;Zhao, Y.;Zhang, S.;Wu, F.;Waterhouse, G. I. N.;Wu, L.-Z.;Tung, C.-H.; Zhang, T. Ammonia detection methods in photocatalytic and electrocatalytic experiments: how to improve the reliability of NH_3 production rates? *Adv. Sci.* **2019**, *6*, 1802109.
[198] Liu, H.;Guijarro, N.; Luo, J. The pitfalls in electrocatalytic nitrogen reduction for ammonia synthesis. *J. Energy Chem.* **2021**, *61*, 149-154.
[199] Zhao, H.;Xiang, J.;Sun, Z.;Shang, S.; Chu, K. Electroreduction of Nitrite to ammonia over a cobalt single-atom catalyst. *ACS Sustainable Chem. Eng.* **2024**, *12*, 2783-2789.
[200] Xiang, J.;Qiang, C.;Shang, S.;Chen, K.;Kang, C.; Chu, K. Tandem electrocatalytic reduction of nitrite to ammonia on rhodium-copper single atom alloys. *Adv. Funct. Mater.* **2024**, *34*, 2401941.
[201] Wang, H.;Zhang, F.;Jin, M.;Zhao, D.;Fan, X.;Li, Z.;Luo, Y.;Zheng, D.;Li, T.; Wang, Y. V-doped TiO_2 nanobelt array for high-efficiency electrocatalytic nitrite reduction to ammonia. *Mater. Today Phys.* **2023**, *30*, 100944.
[202] Wang, F.;Shang, S.;Sun, Z.;Yang, X.; Chu, K. Electrocatalytic nitrite reduction to ammonia on In_1Cu single atom alloy. *Chem. Eng. J.* **2024**, *489*, 151410.
[203] Gupta, S.;Rivera, D. J.;Shaffer, M.;Chismar, A.; Muhich, C. Behavior of cupric single atom alloy catalysts for electrochemical nitrate reduction: An ab initio study. *ACS EST Engg.* **2023**, *4*, 166-175.
[204] Yuwei, Z.; Hanfeng, L. Crystal facet engineering of electrocatalysts for nitrate reduction to ammonia: recent advances and future perspectives. *Chem. Synth.* **2024**, *4*, 39.
[205] Du, C.;Lu, S.;Wang, J.-a.;Wang, X.;Wang, M.;Fruehwald, H. M.;Wang, L.;Zhang, B.;Guo, T.;Mills, J. P.;Wei, W.;Chen, Z.;Teng, Y.;Zhang, J.;Sun, C.-J.;Zhou, H.;Smith, R. D. L.;Kendall, B.;Henkelman, G.; Wu, Y. A. Selectively reducing nitrate into NH_3 in neutral media by PdCu single-atom alloy electrocatalysis. *ACS Catal.* **2023**, *13*, 10560-10569.
[206] Cai, J.;Wei, Y.;Cao, A.;Huang, J.;Jiang, Z.;Lu, S.; Zang, S.-Q. Electrocatalytic nitrate-to-ammonia conversion with ~100% Faradaic efficiency via single-atom alloying. *Appl. Catal. B: Environ.* **2022**, *316*, 121683.
[207] Ajmal, S.;Kumar, A.;Mushtaq, M. A.;Tabish, M.;Zhao, Y.;Zhang, W.;Khan, A. S.;Saad, A.;Yasin, G.; Zhao, W. Uniting synergistic effect of single-Ni site and electric field of B- bridged-N for boosted electrocatalytic nitrate reduction to ammonia. *Small* **2024**, *20*, 2310082.
[208] Gan, T.;Liu, Y.;He, Q.;Zhang, H.;He, X.; Ji, H. Facile synthesis of kilogram-scale Co-alloyed Pt single-atom catalysts via ball milling for hydrodeoxygenation of 5-Hydroxymethylfurfural. *ACS Sustainable Chem. Eng.* **2020**, *8*, 8692-8699.

Address correspondence to Xiaohui Sun, sunxiaohui@cup.edu.cn; Jingjing Jiang, jiangjingjing@bcpca.ac.cn